Imperial College London

Department of Mechanical Engineering

Analysis of building vulnerability and firebrand exposure to mitigate wildfire damage

by

Simona Dossi

A thesis submitted for the degree of Doctor of Philosophy

Supervised by

Prof. Guillermo Rein

September 2023

Statement of Originality

The content of this thesis is the result of the author's own work unless otherwise specified. Parts of this thesis have been adapted from a journal publication written by the author, respecting the respective copyright agreements, and are cited appropriately accordingly.

Copyright Declaration

Ai miei genitori, Alberta e Roberto,
i quali mi hanno regalato una profonda ammirazione per le scienze,
che mi riempe ripetutamente di meraviglia e gratitudine.

Acknowledgements

I would like to thank my supervisor Guillermo Rein for his valuable guidance in developing and conducting this research; and for his inspiring passion for and wisdom in fire science. I am grateful for the engagement of my secondary supervisors; Birgitte Messerschmidt, and Wojciech Węgrzyński, thank you for being inspiring and funny people. This research project wouldn't exist without Prof. Cathelijne Stoof; thank you for your vision. Thank you all for giving me this opportunity.

Both this research and I have greatly benefitted from the numerous fellow early career researchers who I was lucky to meet and share the last few years with. It has been a blessing to interact with people from diverse paths of lives, united by the common objective of learning and contributing to fire safety. A huge thanks to the more experienced members who I interacted with closely and who served as inspiring mentors to me, both scientifically and personally: thank you Dwi, Wuquan, Nadjia, and Matt. Thank you to all my fellow PyroLife ESRs, past and present, who taught me so much through their diverse passions, viewpoints, and motivations.

A special thank you to my parents who I owe so much to, and an extra special thank you to my mother who paved the way for me in so many ways; as the first member of our lineage to graduate from university, and as one of the few women engineering professors. Abaraka Yankuba, for all your love and kindness.

Abstract

Wildfire intensity and resulting damage to communities and infrastructure is increasing worldwide; this thesis investigates the vulnerability of wildland-urban interface (WUI) buildings to wildfires, focusing on firebrand exposure. The research objective is to improve understanding of wildfire damage mechanisms to aid effective risk reduction practices. A comprehensive literature review establishes the need for quantitative building vulnerability assessments and advanced understanding of firebrand deposition and accumulation around solid obstacles. To address these needs, a statistical analysis on two large wildfire damage databases from Portugal and California is conducted to investigate the relationship between building design and damage extent. The results contribute to the development of a preliminary building resistance index (WRI) to assess building vulnerability to wildfire damage.

The thesis progresses to characterise the feasibility of using the Fire Dynamics Simulator (FDS) to simulate firebrand creep movement and accumulation around solid obstacles. A sensitivity analysis quantifies the impact of input parameters on final particle position, revealing a relationship between sensitivity and the Tachikawa number, which describes the aerodynamic properties of simulated particles. A comparison between two FDS Lagrangian Particle model modalities assesses their efficacy in simulating firebrand accumulation based on previously published experimental results. The analysis explain the connection between particulate transport physical mechanisms and the effective operational FDS use for simulating wildfire firebrand exposure. FDS simulations are subsequently conducted to identify regions of firebrand contact exposure, connected to firebrand ignition hazard, around three different obstacles mimicking common building components. Results characterize the combined influence of wind speed and obstacle geometry on firebrand contact exposure. Finally, the applicability of established sand protection measures to protect infrastructure from firebrands is explored by reviewing literature and conducting exploratory FDS simulations. The effectiveness of a trench protection measure to inhibit firebrand accumulation on an infrastructure component is investigated, indicating its potential when combined with contextual information on infrastructure design and ambient conditions.

Table of Contents

Chapter 1 : Introduction to Wildland-Urban Interface Fires

1.1 Wildland-urban interface fires

Wildfires are a complex natural phenomenon, threatening ecosystems and communities worldwide (Manzello *et al.*, 2018). The burning of vegetation in natural environments can vary drastically in fire intensity and in impact; because fire results from specific environmental conditions, the vast environmental diversity results in numerous possible fire regimes (Pyne, 1949). Depending on the ecosystem and the occurring fire regime, wildfires can and have played a crucial role in maintaining biodiversity (Moritz *et al.*, 2014). Nonetheless, uncontrollable wildfires devastating communities' safety socially, economically, and environmentally have been growing worldwide and are now a regular seasonal occurrence in many countries (United Nations Environment Programme, 2022). The majority of wildfire-caused mortalities, infrastructure damage, and emergency fire suppression economic cost occur in the wildland-urban interface (Moritz *et al.*, 2014).

The wildland-urban interface (WUI) is the general term referring to the built environment located adjacent to, or intermixed with, wildlands (Butler, 1974). WUI areas differ in size, layout, and conditions; landscape-scale WUI analysis in literature most often characterises them based on building density, or distance to nearest wildlands (Chappaz and Ganteaume, 2022). When wildfires enter and ignite the built environment, WUI fires are created (Mell *et al.*, 2010). WUI fuels are any combustible materials in these areas, including buildings, vehicles, vegetation, fuel tanks, etc.; alongside ambient conditions, fuel condition determines the WUI fire behaviour and impact. Fuel properties (including bulk, particle, physical and chemical properties), topography, and weather all affect wildfire spread and behaviour; the variety of fuel materials and densities in residential areas contribute to the complexity of understanding WUI fire behaviour and hazard (Simeoni, 2016).

As WUI areas expand, more fuel and people reside in wildfire-prone regions. WUI areas in the USA grew 33% between 1990 and 2010, and WUI areas in the Mediterranean, especially along the wildfire prone coastal regions, are experiencing increasing touristic infrastructure constructions (Galiana-Martin *et al.*, 2011; San-Miguel-Ayanz *et al.*, 2013; Radeloff *et al.*, 2018). In central Patagonia, Argentina the WUI increased 76% in area and 74% in number of houses between 1981 and 2016 (Defossé, 2023). In 2020 the WUI consisted of 15% of European land area, and is inhabited by approximately 44% of the global population worldwide (Schug *et al.*, 2023). This thesis focuses on the wildfire exposure on and vulnerability of single WUI buildings.

The impact of WUI fires has been significant and increasing significantly in recent years. In Australia, the 2009 Black Saturday bushfires complex caused a national record number of casualties, killing 173 people and destroying over 2000 buildings (Teague *et al.*, 2010). The USA annual economic

wildfire cost is approximated between $71.1 billion and $347.8 billion (United Nations Environment Programme, 2022). Analysis of Eurostat economic data including Portugal, Spain, Italy and Greece between 2011 and 2018 indicated a -0.11% to -0.18% wildfire impact on annual GDP rate; with severe wildfires impact reaching approximately -3.3– -4.8% (Meier *et al.*, 2023).

Given the extensive human and economic threat, risk reduction of WUI fire damage is urgent. Post-fire inspection studies (Graham *et al.*, 2012), wildfire exposure models and experiments (Cohen and Butler, 1996; Cohen, 2004; Biswas *et al.*, 2013), and statistical data analysis (Syphard *et al.*, 2012; Knapp *et al.*, 2021), have concluded the building construction and its immediate surrounding conditions primarily determine WUI ignitions and resulting damage. By creating and maintaining appropriate defensible space, or limiting combustibles in the buildings' immediate surroundings, ignitions and subsequent fire spread are prevented. The relevant surrounding area, including the building, has been named the Home Ignition Zone (HIZ) (Smith and Adams, 1991; Cohen, 2008). The wider residential area planning, road access, and emergency service availability, will also influence, to a lesser extent, building fire exposure (NFPA 1140, 2022). Table 1-1 lists all contributing detailed factors identified in literature as significant in affecting wildfire building damage; this comprehensive table includes building construction components as well as surrounding environmental and social factors. The information presented and organised in table 1-1 serves as the scientific basis and justification for building components selection in Chapter 2 and Chapter 5 analysis.

1.2 Building ignition mechanisms

Ignition, generally defined as the initiation of a sustained combustion reaction, of WUI construction materials occurs through three primary exposure mechanisms: flame impingement, flame radiation, and firebrand ignition (Caton *et al.*, 2017); these are illustrated in Figure 1-1. Flame impingement refers to direct contact between flames and fuel; this involves radiation, conduction and convection. Breakthrough experiments across various spatial scales discovered that flame contact with fine fuels correlate with the instabilities generated by buoyancy in the flame zone (Finney *et al.*, 2015). Thermal radiation allows heat transfer from a distance; flame radiation has been calculated as accounting for up to 80% of heat transfer for upward spread of flames under specific conditions (Orloff *et al.*, 1975). Experiments indicate that as flame height increases, the heat flux remains approximately constant, while the exposure area increases (Babrauskas, 2003). Firebrands are aerodynamically buoyant burning fragments of fuel which can ignite fuels at far distances away from flames (Manzello *et al.*, 2020).

Firebrands are often found as the primary cause of building ignitions, both in post-fire inspections and experimental studies (Blanchi *et al.*, 2006; Hakes *et al.*, 2017; Ribeiro *et al.*, 2020). Embers more generally describe small and hot carbon-based fuel particles, and firebrands specifically describe airborne burning particles, which travel through wind-driven transport (Babrauskas, 2018). Firebrands can directly ignite building features by landing and accumulating on their outer surface,

or by entering through openings and igniting the building's interior. Firebrand ignition can also occur indirectly, by firstly igniting adjacent fuel which in turn ignites the building through flame radiation or impingement. Firebrands are generated as fuel burn, lofted by the fire-induced plume, transported aerodynamically in the wind, to finally land, and possibly accumulate and ignite fuel. Literature exploring the physical governing principles of these processes is reviewed in detail in Chapter 3.

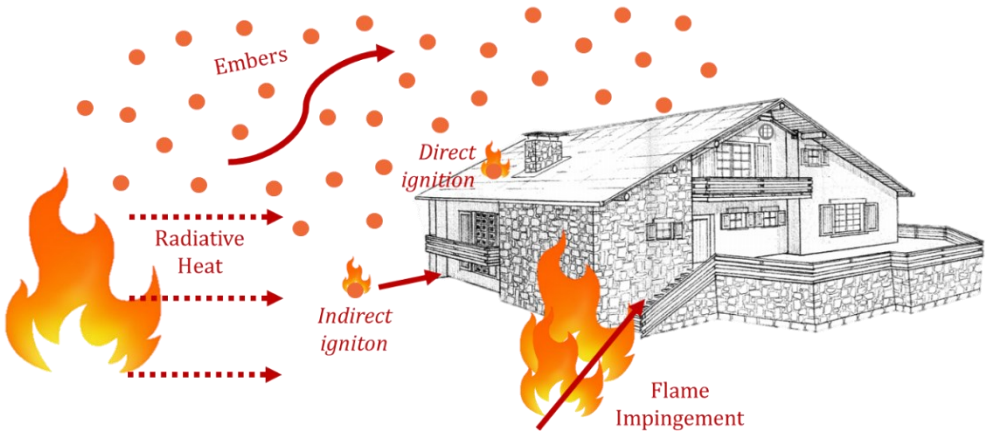

Figure 1-1: Heat transfer mechanisms from wildfire flames to a generic residential building: airborne firebrands causing direct and indirect ignition, flame radiation, and flame impingement.

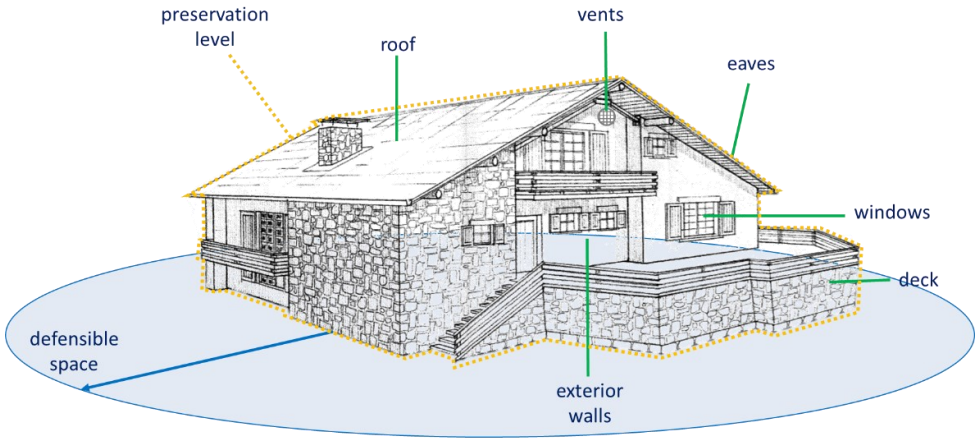

Figure 1-2:. Vulnerable components of generic residential building to wildfires: preservation level, defensible space, roof, vents, eave, window, deck, and exterior wall.

The ignition process of building features is usually studied as flaming ignition of a solid caused by external radiant heat (Torero, 2016). Combustible solids, when exposed to enough heat, will undergo pyrolysis and release pyrolyzed vapours which react with oxygen to form a flame. The physical and chemical properties of the solid material determine its response to heat exposure, and therefore its ignition thresholds per a given exposure. The most common and vulnerable features involved in wildfire building ignition are labelled in Figure 1-2 as identified in literature (Quarles *et al.*, 2010; Hakes *et al.*, 2017). Table 1-1 includes experiments testing each fire exposure mechanism, and each factor's inclusion in existing WUI vulnerability assessments.

Table 1-1: List of wildfire vulnerability contributing factors for WUI buildings. Table includes vulnerable factors, literature identifying factor as vulnerable, experimental investigation of factor response to wildfire exposure, and wildfire vulnerability assessments considering factor.

Relevant Factors influencing building wildfire vulnerability	**Reference** Identification of vulnerability factor (specific	**Experimental studies of wildfire exposure vulnerability/ response** involving factor influence/response	**WUI vulnerability assessments including general factor** (specific factors included)
Building Construction			
Roofing system: includes roof covering, fascia, gutters - material, design, condition.	(Vacca *et al.*, 2020), (Hakes *et al.*, 2017), (NFPA 1140, 2022)	**Radiation and Convection:** Preliminary test plan: (Maranghides *et al.*, 2022) **Firebrands**:(Manzello *et al.*, 2009), (Manzello, 2013), (Manzello, Hayashi, *et al.*, 2010), (Nguyen and Kaye, 2021)	Construction type, general wall and roof: (Papakosta *et al.*, 2017) Roof material, roof type, and roof-leaf accumulation: (Papathoma-Köhle *et al.*, 2022)
Eave: includes overhang, and roof and wall connection – design (overhang size, enclosed or open overhang), material (soffit, roof beam, roof fascia).	(Hakes *et al.*, 2017), (NFPA 1140, 2022)	**Radiation and Convection:** Preliminary test plan: (Maranghides *et al.*, 2022) **Radiation:** (Quarles and Sindelar, 2011), **Firebrands**: (Manzello *et al.*, 2012)	N/A
Ventilation Openings: opening size and location, screen material and area openings.	(Vacca *et al.*, 2020), (NFPA 1140, 2022)	**Radiation and Convection:** Preliminary test plan: (Maranghides *et al.*, 2022) **Radiation:** (Quarles and Sindelar, 2011), **Firebrands** (Quarles and Sindelar, 2011), (Manzello, Park, *et al.*, 2010)	N/A
Windows: frame, glazing, number of panes, glass type, framing system material	(NFPA 1140, 2022), (Vacca *et al.*, 2020)	**Radiation and Convection:** (Shields *et al.*, 2001)**,** Preliminary test plan: (Maranghides *et al.*, 2022) **Firebrands**: (Manzello *et al.*, 2012) **Radiation:**(Klassen *et al.*, 2010)**,** (Quarles and Sindelar, 2011),	Shutters material: (Papathoma-Köhle *et al.*, 2022)
Deck: material, design	(Hakes *et al.*, 2017)	**Firebrands**: (Wheeler, 2004), (Meerpoel-Pietri *et al.*, 2021)	N/A

		Radiation and Flame Contact: (Wheeler, 2004)	
External Walls: material, thickness,	(Hakes *et al.*, 2017), (NFPA 1140, 2022)	**Firebrands:** (Manzello *et al.*, 2012), (Quarles and Sindelar, 2011), (Meerpoel-Pietri *et al.*, 2021). **Radiation**: (Manzello *et al.*, 2018),(Quarles and Sindelar, 2011) **Radiation and Flame contact:** (Cohen, 2000)	Construction type, general wall and roof: (Papakosta *et al.*, 2017) Structural type: (Papathoma-Köhle *et al.*, 2022)
Preservation level: maintenance, accumulated debris/combustibles, feature failures	(Caton *et al.*, 2017)	**N/A**	House damage: (Papakosta *et al.*, 2017)
Surrounding condition			
Neighbouring vegetation, buildings other combustibles **~1 m immediate surrounding** of building	Neighbouring vegetation/combustibles: (NFPA 1140, 2022) Defensible space: (Caton *et al.*, 2017)	**Neighbouring vegetation:** ***Mulch Beds:*** - *Ignition tests:* (cigarette, matches, propane torch): (Steward *et al.*, 2003) - *Firebrands exposure response:* (Suzuki *et al.*, 2015) **Neighbouring urban fuel:** - *Quantifying Exposure:*180-275 m distance from fire (Vacca *et al.*, 2022), Production of firebrands from wooden roof: (Suzuki and Manzello, 2021c), (Manzello *et al.*, 2019), - *Radiation and Convection:* max 10.7 m separation, preliminary test plan: (Maranghides *et al.*, 2022)	Fuel type, tree cover density, NDVI: (Hysa, 2021) Forest cover, elevation, biomass: (Andersen and Sugg, 2019) Land cover, vegetation type, house density: (Papakosta *et al.*, 2017) Main ground covering and vegetation: (Papathoma-Köhle *et al.*, 2022) Type of landscape, land cover: (Galiana-Martin *et al.*, 2011)
Neighbouring vegetation, buildings, fences, other combustibles ~**5 m surrounding area** of building	Neighbouring vegetation/combustibles: (NFPA 1140, 2022) Defensible space: (Caton *et al.*, 2017)		
Neighbouring vegetation, buildings other combustibles >**10 m surrounding area** of building	(Syphard *et al.*, 2012) (Vacca *et al.*, 2020) (NFPA 1140, 2022)		

		- *Radiation and Flame Contact:* 1.8m separation between two buildings (Maranghides and Johnsson, 2008)	
WUI Community and General Location			
Slope of sorrounding terrain	(NFPA 1140, 2022) (Syphard *et al.*, 2012)	Wind and slope effects on fire rate of spread on forest litter (Boboulos and Purvis, 2009).	(Andersen and Sugg, 2019) (Hysa, 2021) (Papathoma-Köhle *et al.*, 2022) (Galiana-Martin *et al.*, 2011)
Access to **emergency services:** e.g.: distance to fire station, road access	(NFPA 1140, 2022)	**N/A**	Road density: (Andersen and Sugg, 2019) Distance to fire station: (Papakosta *et al.*, 2017)
Population characteristics		**N/A**	Building density: (Galiana-Martin *et al.*, 2011) Socio-economic vulnerability: (Andersen and Sugg, 2019)
Climate		N/A	Temperature and precipitation: (Andersen and Sugg, 2019) Solar radiation, precipitation, temperature, wind speed: (Hysa, 2021) FWI: (Papakosta *et al.*, 2017)

1.3 Vulnerability Assessments

Assessing WUI fire ignition, spread, and damage is a complex task requiring the interpretation and integration of many diverse parameters. Given the variable complexity of possible wildfire exposures and WUI vulnerabilities, detailed fire risk assessments of buildings' fire response are limited, and not viable on large-scale application due to data availability, financial and time constraints. Risk indexing is a quantitative, cost-effective methodology which can be used as a prioritisation tool when detailed engineering risk analysis is not possible. Indexing uses simplified models of fire safety that produce a numerical risk ranking (Watts, 2008).

Especially in the USA, assessment programs and tools are available for residents to evaluate and mitigate their community's vulnerability to wildfire damage. The NFPA community programme, Firewise (National Fire Protection Association, 2022) educates and empowers residents to take wildfire risk reduction actions. The Institute of Building and Home Safety (IBHS) developed a mobile app 'Wildfire Ready Virtual' that allows users to photograph their home and assesses its vulnerability through virtual reality software; IBHS recently launched its own residents-focused preparation program 'Wildfire Prepared Home' (IBHS, 2022). A specialised website, defensiblespace.org, provides guidance for communities located in the Southern California region (SMMNRA, no date). Although these tools offer practical and empowering resident-focused mitigation approaches, comprehensive scientific risk assessments are necessary to methodologically apply community-scale and industry-scale mitigation measures.

Table 1-2 provides a list of recent WUI vulnerability assessments, each considering different geographical areas, contributing vulnerability factors, and quantification methodologies. The lack of studies focusing on the building construction area, despite its widely recognised crucial importance (IBHS, 2021), illustrates an important gap in literature.

Table 1-2: List of recently published quantitative WUI vulnerability assessment methods and the location considered for development and/or validation.

Reference	Vulnerability assessment/ranking method description	Location considered
(Papakosta *et al.*, 2017)	Bayesian Network probabilistic model for wildfire building damage prediction	Cyprus
(Papathoma-Köhle *et al.*, 2022)	Physical Vulnerability Index (PVI) for wildfire building damage developed using random forest model.	Mati, Greece
(Andersen and Sugg, 2019)	Mapped and validated wildfire vulnerability index based socio-economic and physical data in GIS.	Western North Carolina, USA

(Hysa, 2021)	Wildfire vulnerability assessment of vegetation in WUI areas based on anthropogenic, hydro-meteorological, geophysical, and fuel properties.	Sarajevo, Bosnia Tirana, Albania
(Galiana-Martin *et al.*, 2011)	Landscape analysis and GIS and remote sensing techniques to assess WUI hazard and vulnerability	Valencia, Spain
(Samora-Arvela *et al.*, 2023)	Multiple regressions analysis analyses the relationship between factors obtained through GIS calculation and public data to wildfire damage	Santa Comba Dão municipality, Portugal

The vulnerability assessments listed also reflect the different scales which built environment wildfire vulnerability exists on and needs to be considered from. On a larger landscape scale, the topography and landscape characteristics combined with the human characteristics relating to social vulnerabilities and emergency resources available are significant in determining wildfire impact. On a smaller, single-building scale, the building components designs, construction materials, and immediate surroundings, are significant in determining wildfire damage.

The only quantitative WUI building wildfire vulnerability index known to authors are (Wilson, 1984) and (Papathoma-Köhle *et al.*, 2022). Wilson considered 450 houses exposed to bushfire in Australia; the study considered fire intensity, attendance by residents, roof material, wall material, presence of flammable objects' and vegetation around the house (Wilson, 1984). In chapter 3 we expand on this approach by considering two different geographical regions, and a larger sample of buildings. We present an analysis of two different post-fire building inspection databases, from the USA and Portugal, and develop the Wildfire Resistance Index (WRI), a preliminary risk index specifically applied to rural buildings. The objective is to quantify the relationship between characteristics of the building feature and damage, and validate the methodology with data from two diverse WUI regions.

1.4 European rural building constructions

Significant amount of the literature and analysis cited in this chapter has been developed in the USA and Australia, where destructive wildfires have been causing extensive damage to communities and infrastructures for decades. This section provides general statistics, qualitative, and photographic data collected regarding rural construction design across the European continent to contextualise the literature reviewed earlier in this section. Table 1-3 presents general background information comparing the construction materials used for the external building envelope and the roofing system in the USA and Portugal; these regions are specifically chosen because post-fire damage data from these countries is analysed in Chapter 3 to provide a quantitative methodology for building wildfire vulnerability assessment. The significant differences in building design can impact which wildfire

exposure is most important to defend structures from. The statistics presented in Table 1-3 reflect the high fire resistance of roof and wall construction materials in Portugal, compared to California.

Table 1-3: Background information on common construction materials for external building envelope, and roof coverings in residential homes in the USA and Portugal.

-	External building envelope	Roofing System
USA	*USA national census data 2021 for Single-Family Homes:* Bricks (19%), Wood (4%), Stucco (27%), Vinyl Sidings (26%) Fibre Cement (22%) (US Department of Housing and Urban Development, 2021).	*National:* Asphalt composition shingles (78.6 %), steel panels and tiles (15.6%), wood roofs (5.8%) *California:* Wood shake/shingle roofs (42 %) (Kimiko, 2022).
Portugal	*2011 survey data:* Reinforced concrete (48.6 %), Masonry walls with reinforced concrete deck (31.7 %), masonry walls without concrete deck (13.6 %) Loose stone masonry walls (5.3 %).(Mendes, 2013).	*2011 survey data:* Ceramic or concrete tiles 93,1% (Mendes, 2013).

Figure 1-3: Photos of WUI buildings in Europe taken by Simona Dossi in 2021 and 2022 from (a) Vila Real, Portugal, (b) la Grigna, Lombardia, Italy, (c) Warsaw, Poland and (d) Aberystwyth, Wales

There is a wide variety of rural building construction materials and designs across Europe, comparable to the European landscapes, climates, cultures, and governance diversity. This variation renders wildfire infrastructure vulnerability a local and relative phenomenon; Chapter 3 addresses this by presenting a statistical analysis of post-fire building damage data from diverse locations.

Figure 1-3 provides photos of various rural building constructions in different locations around Europe; this is provided as context for how the different building vulnerabilities listed in Table 1-1 act in unison, coupling numerous vulnerabilities, and to illustrate the diversity of building constructions that can be found across the continent. Figure 1-3a and Figure 1-3b provide examples of common southern European rural buildings from Italy and Portugal, while Figure 1-3c and Figure 1-3d provide examples of temperature European countries constructions from Poland and Wales. The four selected photos are included to illustrate high wildfire vulnerability, in Figure 1-3a and Figure 1-3c, and low wildfire vulnerability, in Figure 1-3b and Figure 1-3d, constructions in each general European area.

Firstly considering the high vulnerability examples, although in southern Europe the external walls and roofing materials are made of fire-resistant materials - most often using masonry, concrete, and stone, as expanded on in Table 1-3 – other common vulnerabilities can nonetheless lead to extensive wildfire damage. Figure 1-3a illustrates numerous of these vulnerabilities: dense vegetation coming to contact with the external walls, low maintenance level of the building structures (referred to as preservation level in this thesis) illustrated by broken and missing glazing, and by openings under the tiles in the buildings eaves. Figure 1-3c, shows the external envelop of the construction built solely with seemingly untreated wood, and high vegetation amount and density in direct contract with this low fire resistance construction material.

Figure 1-3b and Figure 1-3d are photos of rural constructions in the Alpine Mountain region, and the Welsh coast region respectively. Showing two different ecosystems and landscapes, both at risk of damaging wildfire activity, and different building construction materials and styles. The following photos were selected as examples of low wildfire ignition and damage construction, in terms of construction materials adopted and maintenance level of both the construction and the surrounding vegetation. Both building constructions are well-maintained: the roof and external wall connections, the windows and doors have functional fittings. Furthermore, no accumulated debris or vegetation is present around the building, and on the building in the gutters or on the room. Lastly a well-defined distance between the building and any vegetation is created: in Figure 1-3b stones are used to create a fire-resistant path all around the building construction that keep even grass from coming to contact with any building features. Although less clear from the photograph, Figure 1-3d shows a construction raised above a garage structure; the way this is designed safely keeps vulnerable features away from the surrounding vegetations and creates a safe distance from possible wildfire exposure. The design of these structures includes the fire protection measures for wildfire exposure that will be expanded on in this thesis.

Chapter 2 : Characterising Building Vulnerability - Wildfire Resistance Index

2.1 Introduction

The increasing occurrence and severity of wildfires in WUI areas have highlighted the urgent need to understand the relationship between building design and wildfire damage, in order to build and maintain safer residential areas. In this chapter, we explore the correlations between various building features and the level of damage caused by wildfires in two different databases: the California Department of Forestry and Fire Protection (CAL FIRE) database and the Pedrógão Grande database in Portugal. The research presented in this chapter is adapted from a journal publication led by the author (Dossi *et al.*, 2022).

In Australia, Wilson first conducted a post-fire building damage data to predict wildfire damage probability (Wilson, 1984); this chapter extends this analysis methodology applying more advanced statistical test to larger, more comprehensive, and multiple damage databases. California and Portugal are both high wildfire risk regions, regularly experiencing intense wildfires and wildfire damage; these regions were specifically selected due to the significant difference between their respective building constructions styles. The comparison between building constructions and wildfire damage in the regions can provide valuable insight in the necessary difference for building risk-reduction in southern Europe building constructions compared to common constructions in the USA. The objective of this analysis is to gain insight regarding the most vulnerable building characteristics, both in terms of design geometry and construction materials, of WUI buildings to wildfire ignition and damage.

To assess the overall fire protection level of buildings in WUI areas, we introduce the Wildfire Risk Index (WRI). This index is a simple and yet valuable tool created to assess the cumulative impact of multiple building features on wildfire vulnerability. By assigning fire protection coefficients to each characteristic of a building, the WRI allows for a methodical comparison of the overall fire resistance of different structures. The final WRI values range from -1 to 1; 1 representing higher fire protection, and -1 indicating lower fire protection. To validate the applicability of this index a correlation analysis is conducted with the damage databases analysed in this chapter. The correlation between the WRI and damage levels is encouraging especially for the Portuguese data; the variation between the CAL FIRE and Pedrógão Grande databases, suggesting that factors not considered in the WRI, such as building-to-building separation distance and defensible space condition, play a stronger role in determining building damage in California.

2.1.1 Case studies: California and Pedrógão Grande

We consider 17500 buildings exposed to 59 wildfires in California, USA between 2013 and 2017, from the CAL FIRE (DINS) database of wildfire-exposed building damage inspections (Henning *et al.*, 2016); and data of 1190 buildings exposed to the 2017 Pedrógão Grande Fire Complex in Portugal derived from comprehensive damage inspection of exposed structured conducted by ADAI (Ribeiro *et al.*, 2020). The databases were selected because of their large sample size, and the amount of building construction design information included, which allows meaningful statistical analysis. Furthermore, the geographical regions considered, California, USA and rural Portugal, both have experienced significant WUI damage and are wildfire-prone regions relevant to this study. In 2021 California was estimated to have over 2 million properties in with high or extreme wildfire risk, the highest number out of all USA states (Verisk, 2022). The estimated damage caused by the 2017 fires in Portugal, between June and October, is €1.5 billion, 97% of which attributed to physical damage (San-Miguel-Ayanz *et al.*, 2021).

Lastly, the analysis serves to compare wildfire risk and impact on different WUI constructions. As the regions have differing building construction styles and materials. Table 1-3 provides background information on common building materials used in the USA and Portugal for the external building envelop and roofing system; this table provides general background information on difference in construction practices and materials in the region.

In both databases the dependent variable is damage level; it is characterized between six possible levels in the CAL FIRE database: (0) No Damage, (1) 1-9%, (2) 10-25%, (3) 26-50%, (4) 51-75%, and (5) Destroyed, and between five levels in the Pedrógão Grande Fire Complex database: (0) No Damage, (1) 1-19%, (2) 20 - 39%, (3) 40 – 75%, and (4) Destroyed. We note the damage level ranges differ between the two databases. Other important differences include the number of inspectors, the training received by inspectors; these are all relevant factors which can influence the definition and type of data collected. The California database was collected by numerous inspectors over 5 years, the Portuguese data was collected by one team of two inspectors which increased consistency. All information relating to the building construction and condition was selected as independent variables. The independent variables in the CAL FIRE database are: roof material, number of windowpanes, exterior walls material, eaves presence, deck material, and vents presence. In the Pedrógão Grande Fire Complex database the independent variables are: exterior walls material, preservation level, roof material and, deck material. The data was filtered for relevance; the CAL FIRE database was limited to buildings exposed to wildfire between 2013-2017.

2.1.2 Descriptive Statistics

Bar graphs of the number of inspected buildings per damage level, which illustrate the damage level distribution for the CAL FIRE database, and Pedrógão Grande database are presented in Figure 2-1. Note that the damage levels are defined differently in each database. Figure 2-1 illustrats the large

skewedness of the CAL FIRE data toward 'Destroyed' buildings. The vast majority (87.4 %) of buildings inspected post wildfire were completely destroyed; this indicates the severity of WUI fire in California. The Pedrógão Grande Fire Complex damage is characterised by more evenly distributed damage levels 38.5% of inspected building characterised as destroyed, and 36.3% as highly damaged (damage level of 40-75%). These distributions illustrate an inherent difference in wildfire building resilience between the regions, despite differing damage level definitions.

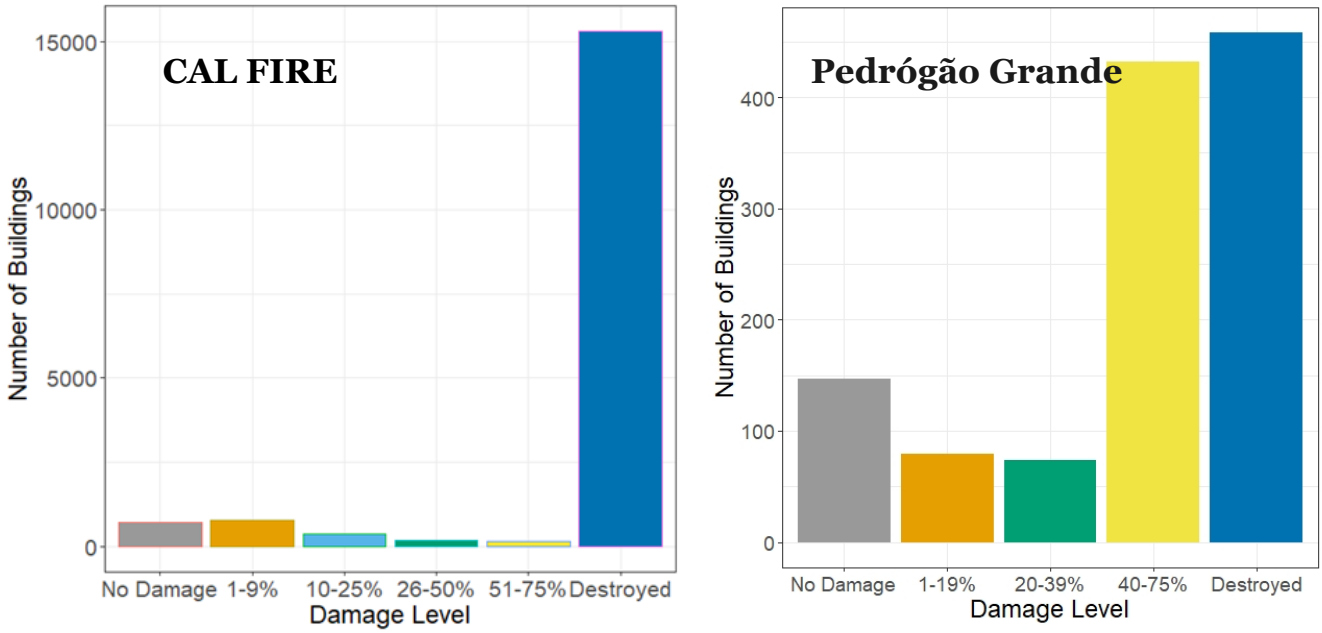

Figure 2-1: Distribution of damage in CAL FIRE database (left) and Pedrógão Grande database (right) by number of buildings

The independent variables considered describing the building: either relating to the building features (e.g: roof, walls, deck) or building condition (e.g.: preservation level). All possible characterizations for each variable, are summarized in Table 2-1 and Table 2-2 for the CAL FIRE and Pedrógão Grande Fire Complex databases respectively. "N/A" refers to buildings that did not have the feature in question; some buildings do not have any decks, or eaves when buildings lack overhang at connection between the roof and external wall e.g.: mobile homes, trailers, metal roofs.

Table 2-1: Building features characteristics included in the CAL FIRE database.

Roof	Windowpanes	Exterior Walls	Deck	Eaves	Vent Screens
Fire Resistant	Double	Fire Resistant	Masonry	Enclosed	Yes
Combustible	Single	Combustible	Wood	Un-Enclosed	No
			Composite	N/A	
			N/A		

Table 2-2: Building features characteristics included in the Pedrógão Grande database.

Exterior Walls	Preservation Level	Roof	Deck
Masonry	Well Preserved	Combustible (Metal Plate)	Masonry
Stone	Moderately Preserved	Fire Resistant (Ceramic Tile)	Wood
Wood	Poorly Preserve		N/A
Metal			

All characteristics listed in Table 2-1 and Table 2-2 are classified as providing lower or higher levels of fire protection to the building. The fire protection classification is based on published knowledge on fire protection of various materials and designs, presented in Table 1-1; and is relative to the other characterisations available in the relevant database for the same feature variable. Figure 2-2 shows the proportion of variables classifies as offering low fire protection, high fire protection, or unknown, for the CAL FIRE database and Pedrógão Grande Fire Complex database respectively. The Pedrógão Grande database ranges from 80% high fire protection characteristics (exterior walls material and preservation level) to 99% high fire protection (deck material). Contrastingly, the CAL FIRE database, the average percentage of high fire protection characteristics is 31%; ranging from a minimum of 1% high fire protection (eave geometries), to a maximum of 75% of high fire protection (roof material).

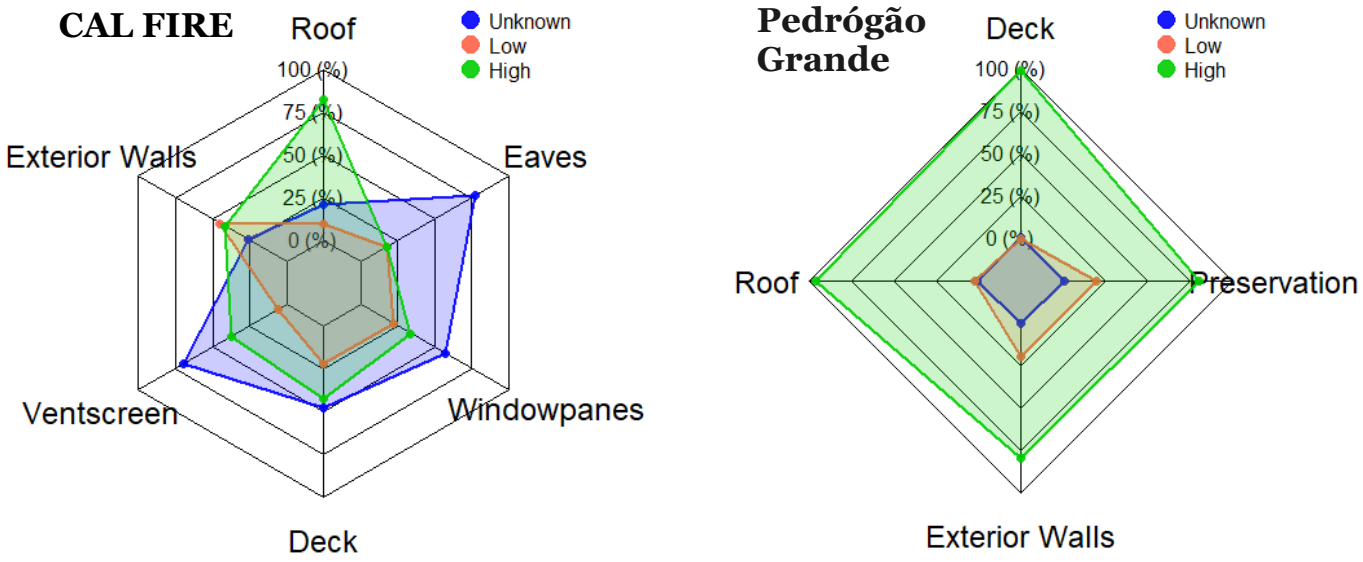

Figure 2-2: (left) Distribution of low fire protection (Red), high fire protection (Green), and unknown (Blue) building features considered in the CAL FIRE database and (right) in the Pedrógão Grande database

Pie graphs showing detailed subdivision of all possible variable characteristics are presented for variables with three or more possible characteristics: Figure 2-3 show the distribution for the deck material, and eaves geometry in the CAL FIRE data. Figure 2-4 show the distribution for preservation level, and external walls as distributed in the Pedrógão Grande data.

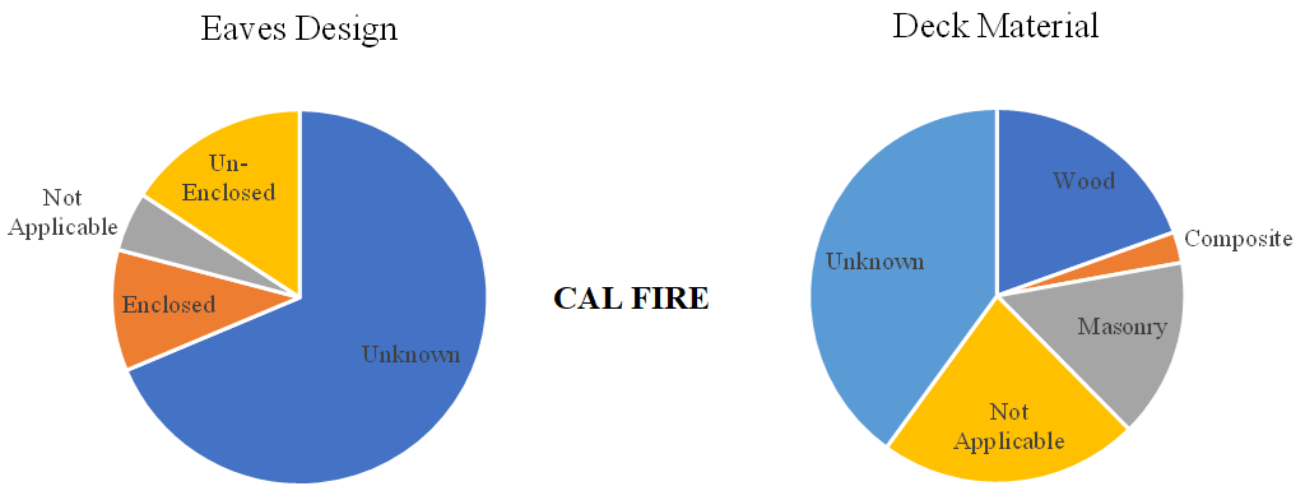

Figure 2-3: CAL FIRE database distribution of characteristics by number of buildings for (a) eave geometry and (b) deck material

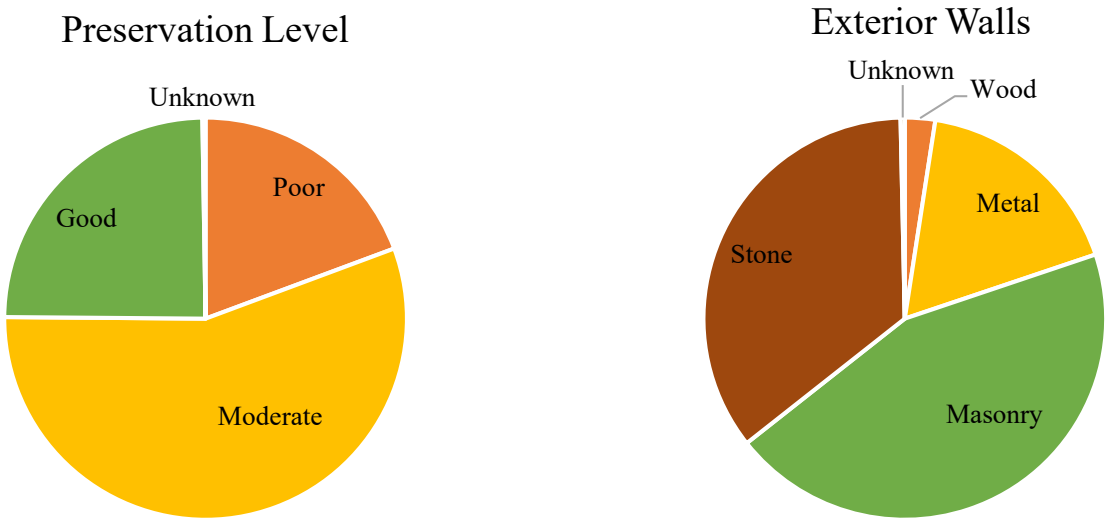

Figure 2-4: Pedrógão Grande database distribution of characteristics by number of buildings for (a) preservation level and (b) with external walls material.

2.1.3 Handling missing data

Table 2-3 and Table 2-4 summarise the percentage missing data for each independent variable considered for the CAL FIRE and Pedrógão Grande databases respectively. CAL FIRE data includes as high as 69% (eave geometry) of missing data per building feature variable; if disregarded, the high

proportion of unknown data can introduce bias in the analysis (Pampaka *et al.*, 2016). Two different types of analysis are presented in this paper: the ranking of relative importance of independent building feature variables for wildfire damage (sections 2.3.1 and 2.4.1), and the WRI development and validation (sections 2.3.2 and 2.4.2). Missing value imputation is used to handle missing data for the ranking analysis. The WRI calculations use the original databases, without imputation; missing data is assigned a coefficient of 0 to not influence the final WRI value instead. An iterative imputation method based on a random forest, computed with RStudio 1.3.1093 package 'missForest', is chosen as imputation method due to the low computational power and time required, and its built-in imputation error estimation: the random forest out-of-bag error (Stekhoven and Bühlmann, 2012). The out-of-bag error, proportion of falsely classified, for the imputed CAL FIRE data is 19.9%, and 27.6% for the Pedrógão Grande data.

Table 2-3: Percentage of missing data in the CAL FIRE database per independent variable.

Damage	Roof	Window	Exterior	Eaves	Deck	Vent
0.0%	18.8%	50.5%	23.1%	68.7%	40.0%	61.7%

Table 2-4: Percentage of missing data in the Pedrógão Grande database per independent variable

Damage	Exterior	Preservation	Roof	Deck
0.0%	0.08%	0.25%	1.01%	0.42%

2.2 Methodology

2.2.1 Statistical dependence tests

Statistical dependence tests are conducted to analyse and quantify the correlation between each building feature (independent variable) and damage level (dependent variable). Given the complexity of the physical processes which cause the correlation between variables (many independent variables, all correlated with each other as well as with dependent variable, furthermore dependent variable also dependent on many unconsidered variables as presented in Table 1-1), and the level of uncertainty in the databases (due to missing data which is discussed in section 2.1.3), three applicable statistical dependence tests based on different statistical methods are conducted and compared: the Bayes Factor (BF), the Chi Square test of independence with Cramer's V, and the Boruta feature selection using random forests. For the BF and Chi Square test, the null hypothesis is defined as no relationship between building feature and damage, or that wildfire building damage is independent of the building feature characteristic considered. All calculations are computed with RStudio 1.3.1093, with packages 'BayesFactor', 'lsr', and 'Boruta'.

The BF is the ratio between the probability of the alternative hypothesis, and the probability of the null hypothesis being true based on the observed data. The higher the value of the BF, the stronger the evidence against the null hypothesis is in the data (Gunel and Dickey, 1974; Rouder *et al.*, 2009). Equation 1 describes the BF where *P(x)* is the probability of *x*, D is the observed data, M_{alt} is the model for the alternate hypothesis, and M_{null} is the model for the null hypothesis.

$$BF = \frac{P(D|M_{alt})}{P(D|M_{null})} = \frac{probability\ the\ variables\ are\ dependent}{probability\ the\ variables\ are\ independent} \qquad \textit{Equation 1}$$

The BF in this study is calculated assuming a poisson sampling plan, referring to the fact that neither the number of buildings exposed to wildfire, nor the variables considered were pre-determined before the inspections (Gunel and Dickey, 1974; Rouder *et al.*, 2009).

The Pearson's Chi Square Test of Independence evaluates the likelihood that a particular distribution occurred randomly, or without any significant relationship between independent and dependent variables. Equation 2 defines the Chi Square χ^2 value, I and J are the independent and dependent variables, and i and j are each variable's possible characteristics, E_{ij} is the expected number of combinations of variables (assuming the null hypothesis), and O_{ij} the observed number of combinations. The p-value threshold is taken as 0.001, corresponding to 99.9% confidence of statistically significant dependence.

$$\chi^2 = \sum_{i=1,j=1}^{I,J} \frac{(E_{ij} - O_{ij})}{E_{ij}} \qquad \textit{Equation 2}$$

Cramèr's V is calculated to estimate the effect size, or strength, of the relationship between variables. Cramèr's V is based on the Chi Square and ranges from 0 to 1, the greater the value, the stronger the estimated relationship is. Equation 3 defines Cramèr's V, and n is the sample size.

$$V = \sqrt{\frac{\chi^2/n}{min(I,J)-1}} \qquad \textit{Equation 3}$$

Lastly, Boruta feature selection uses calculated importance scores provided by Random Forest algorithms and compares them to those of randomly generated "shadow variables" to calculate relative importance of each independent variable. The shadow variables are generated by randomly shuffling original variables in order to maintain the existing distribution but eliminate their correlation to the dependent variable. All variables that rank of higher importance than the shadow variables are selected as relevant features (Kursa and Rudnicki, 2010). The interpretation for the values calculated by these statistical tests can vary depending on the degrees of freedom of a certain variable; guides to interpret these values are provided below. Table 2-5 provides the interpretation of the BF value, adapted from Lee and Wagenmakers (Lee and Wagenmakers, 2014).

Table 2-5: Interpretation of BF Value

BF value	*Interpretation*
>100	Extreme evidence for alternative hypothesis
1-100	Some evidence for alternative hypothesis (evidence strength depending on magnitude)
1	No evidence
1/3 -1/100	Some evidence for null hypothesis (evidence strength depending on magnitude)
<1/100	Extreme evidence for null hypothesis

Table 2-6 provides the interpretation of the Cramer's V value, adapted from Rea and Parker (Rea and Parker, 1962). Table 2-7 provides, more generally, how the number of degrees of freedom in the original data impact the interpretation of Cramer's V value; this is significant for presented analysis as degrees of freedom vary between building features considered.

Table 2-6: Interpretation of Cramer's Value

V value	*Interpretations*
0 - 0.1	Negligible association
0.1 - 0.2	Weak association
0.2 - 0.4	Moderate association
0.4 - 0.6	Relatively strong association
0.6 - 0.8	Strong association
0.8 - 1.0	Very strong association

Table 2-7: Cramer's V Interpretation impacted by degrees of freedom values

Degrees of Freedom	*Small association*	*Medium association*	*Large association*
1	0.1	0.3	0.5
2	0.07	0.21	0.35
3	0.06	0.17	0.29
4	0.05	0.15	0.25
5	0.04	0.13	0.22

2.2.2 WRI

A simple Wildfire Resistance Index (WRI) was created for each building, in order to compare the cumulative effect of multiple building features on wildfire damage. A fire protection coefficient of -1, 0, or 1, is assigned to each building feature characteristic (1 corresponds to higher fire protection, -1 to lower fire protection, and 0 to unknown or intermediate characteristics). These coefficients are

summed for all features of every building, and normalised to the range [-1, 1] by dividing by the maximum index value of the sample data. Equation 4 describes this calculation; where WRI is the wildfire resistance index, and C_i is the coefficient assigned to building feature i.

$$WRI = \frac{\sum C_i}{max(\sum C_i)} \qquad \textit{Equation 4}$$

The WRI relates to the relative number of characteristics offering high fire protection, compared to characteristics offering lower fire protection. A value of 1, therefore, refers to buildings classified as having all possible high fire protection characteristics, and a value of -1 to buildings having only lower fire protection characteristic possible. An assumption of this WRI definition is that all building features contribute equally – Authors note this is a preliminary development stage, and limitations of current WRI methodology are fully discussed in the discussion. Table 2-8 and Table 2-9 provide the C_i values for both databases. Note, the exterior wall material 'metal' is classified providing 'low fire protection'; this most commonly refers to thin (< 1mm thick) aluminium, galvanised or zinc plated, sheets used in low value structures. This material is more susceptible to fire exposure compared to other possible options for the same variable.

Table 2-8: The WRI coefficients (C_i) assigned to the CAL FIRE building features: -1, 1 or 0 in order of their fire protection ranging from providing poor fire protection, to high fire protection.

C_i	Roof	Windows	Exterior	Deck	Vent Screens	Eave Design
-1	Combustible Material	Single pane	Combustible Material	Wood	Not present	No Eaves Un-enclosed
1	Non-combustible Material	Multiple panes	Non-combustible Material	Masonry No Deck	Present	Enclosed
0	Unknown	Unknown	Unknown	Composite Unknown	Unknown	Unknown

Table 2-9: The WRI coefficients (C_i) assigned to the Pedrógão Grande building features: -1, 1 or 0 in order of their fire protection ranging from providing poor fire protection, to high fire protection.

C_i	Roof	Preservation Level	Exterior	Deck
-1	Combustible Material	Poor	Wood Metal	Wood
1	Non-combustible Material	Good	Masonry Stone	Masonry No Deck
0	Unknown	Unknown Moderate	Unknown	Unknown

2.3 Results

2.3.1 Statistical dependence tests

Table 2-10 and 2-11 present the statistical dependence tests results for each database considered. The results include the Chi Square value, its associated p-value which indicates statistical significance of correlation to damage level, Cramer's V value and the degrees of freedom which are necessary for interpretation of Cramer's V value (Cohen, 1988), the BF value, and the median importance value calculated with Boruta feature selection. Each table includes a 'ranking' column which presents the relative ranking of variable importance for each methodology results, the ranking is also colour-coded with darker colours corresponding to higher correlation to damage level; authors note that values of similar magnitude are interpreted as having the same correlation ranking as these statistical tests are designed to give a range of correlation strength rather than specific absolute values. Figure 2-5 and Figure 2-6 present the graphical visualisation of distribution of importance value calculated with the Boruta feature selection method, and how they compare to shadow feature importance. All independent variables considered are found to be statistically significantly correlated to damage level by all the statistical methods applied.

Table 2-10: CAL FIRE database Chi Square of Independence, BF, and Boruta Feature Selection analysis results. The 'ranking' columns classify the correlation strength of each method's numerical result.

Method:	**Chi Square of Independence and Cramer's V**					**Bayes Factor**		**Boruta Selection**	
	Chi Square	*p-value*	*Cramer's V*	*DoF*	*Ranking*	*Bayes Factor*	*Ranking*	*Median importance value*	*Ranking*
Roof	122.41	<0.001	0.084	3	3	2.31×10^{21}	3	65.44	4
Exterior	280.79	<0.001	0.13	3	1	1.49×10^{55}	1	60.60	5
Windows	25.02	<0.001	0.038	3	4	3.29	4	104.52	1
Vents	318.50	<0.001	0.14	3	1	4.36×10^{51}	1	81.22	2
Deck	311.35	<0.001	0.077	9	1	2.86×10^{53}	1	82.77	2
Eaves	160.56	<0.001	0.068	6	2	1.43×10^{23}	2	81.70	2

Table 2-11: Pedrógão Grande database Chi Square of Independence, BF, and Boruta Feature Selection analysis results. The 'ranking' columns classify the correlation strength of each method's numerical result.

Method:	**Chi Square of Independence and Cramer's V**					**Bayes Factor**		**Boruta Selection**	
	Chi Square	*p-value*	*DoF*	*Cramer's V*	*Ranking*	*Bayes Factor*	*Ranking*	*Median importance value*	*Ranking*
Roof	33.63	<0.001	3	0.168	3	23.39	4	26.48	3
Preservation	140.91	<0.001	6	0.243	2	4.09×10^{26}	3	26.26	3
Exterior	269.84	<0.001	12	0.276	1	4.19×10^{55}	1	39.01	2
Deck	362.45	<0.001	6	0.39	1	6.72×10^{44}	2	62.84	1

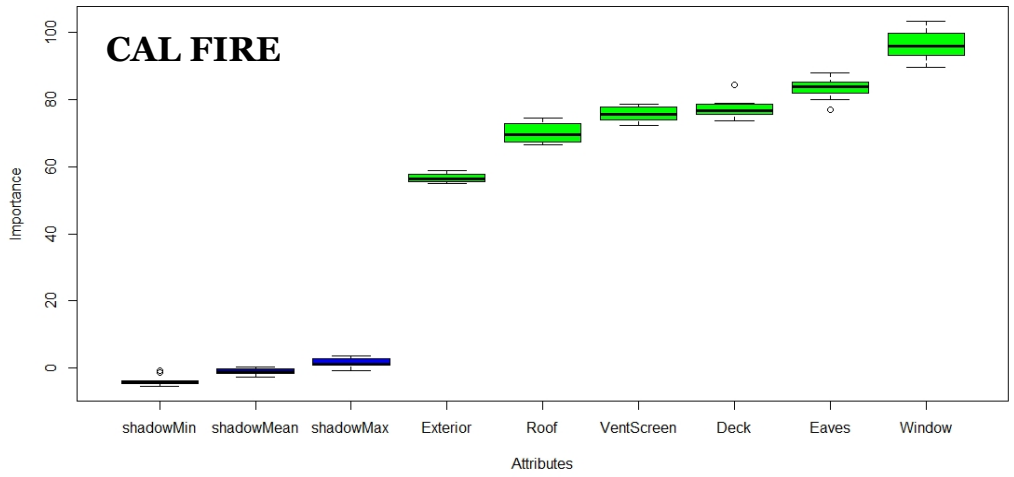

Figure 2-5: CAL FIRE database independent variables importance calculated by boruta feature selection.

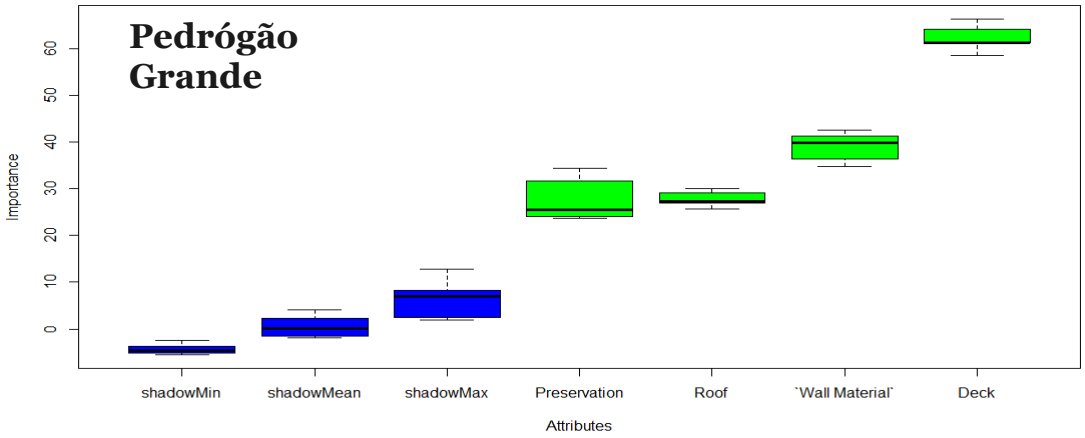

Figure 2-6: Pedrógão Grande database independent variables importance calculated by boruta feature selection.

The Cramer's V and BF analysis agree on the ranking of relative correlation strength for the CAL FIRE independent variables: vent screens, deck material, and exterior wall material rank as highest correlation, followed by eaves design, roof material, and number of windowpanes ranking as having the lowest correlation to damage level. The Boruta feature selection results disagree, and result in a switched ranking for number of windowpanes, with the highest correlation to damage level, and exterior wall material, raking with the lowest correlation to damage level. For the Pedrógão Grande database, the BF and Cramer's V analysis agree completely in the ranking of the building features' correlation. The BF and Cramer's V analysis ranking is: exterior wall material ranks as most highly correlated, followed by deck material, preservation level, and least strongly correlated is roof material. The Boruta analysis ranks Deck material as most highly correlated, followed by exterior material, and lastly roof material and preservation level with comparable ranking.

Due to the variation in number of buildings with each WRI value, the WRI is plotted against the proportion of buildings in each WRI value (calculated by dividing number of buildings with indicated WRI and damage level, with the total number of buildings considered) in Figure 2-9 - Figure 2-12. The size of the plotted circles in Figure 2-9 - Figure 2-12 is proportional to the number of buildings with each WRI value. Two distinct linear correlations are fitted to in each figure to reflect the two observed trends; our analysis focused on correlations including the larger number of buildings, and therefore indicating more meaningful results.

2.3.2 WRI

Figure 2-7 and Figure 2-8 show damage level distributions plotted against WRI values. The figures illustrate distribution with boxplots, and jitter plots showing the relative concentration of houses with each damage level and WRI value combination.

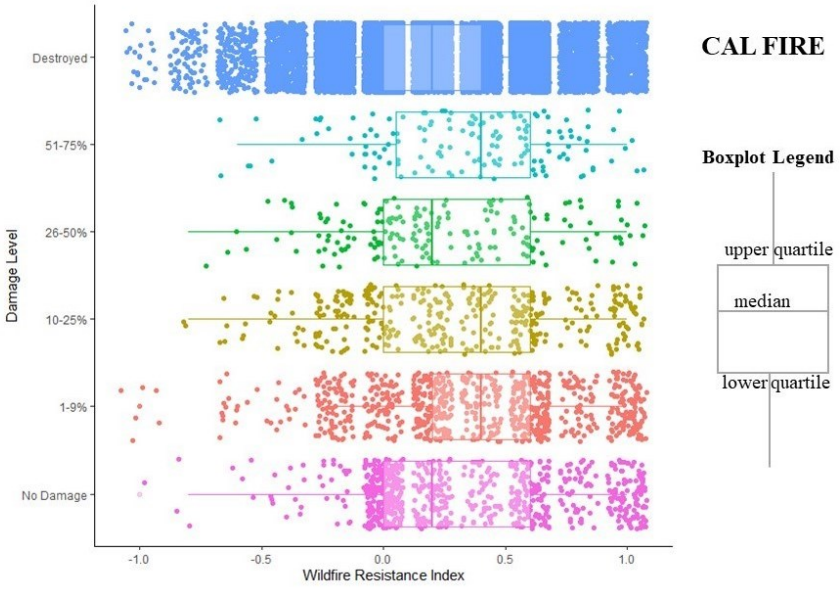

Figure 2-7: CAL FIRE database WRI against damage level as boxplot and jitter plot

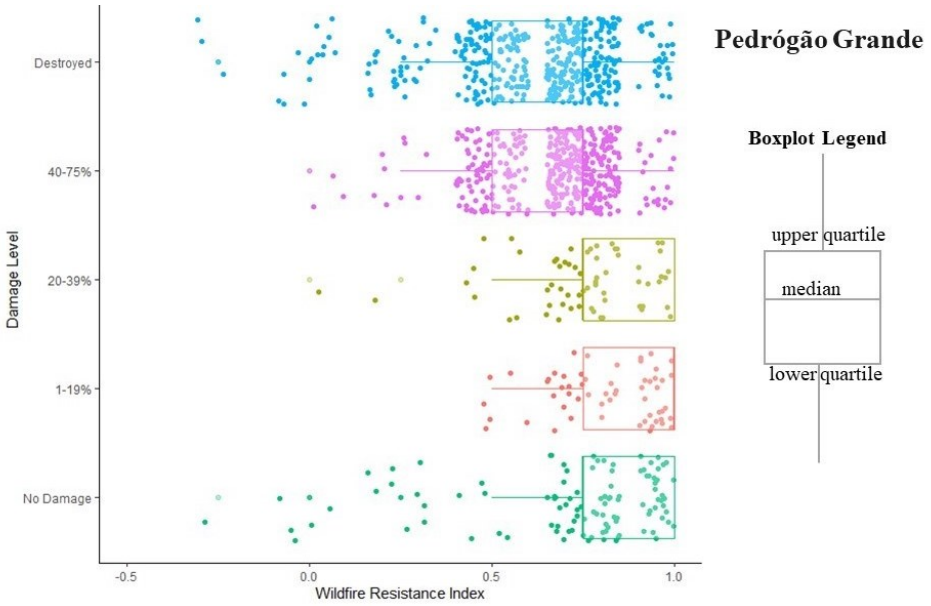

Figure 2-8: Pedrógão Grande database WRI against damage level as boxplot and jitter plot

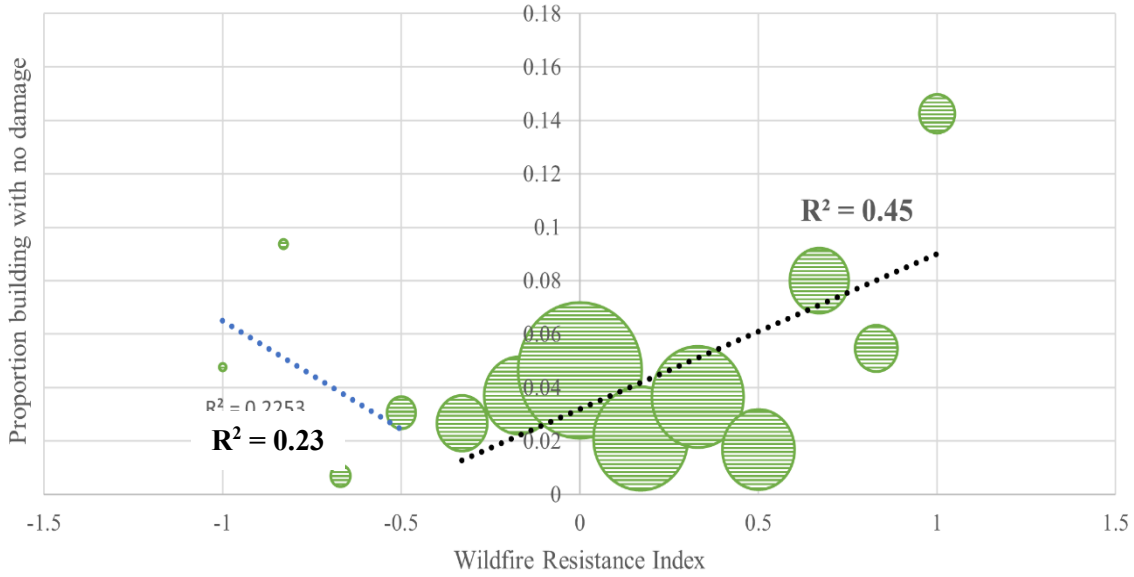

Figure 2-9: CAL FIRE data: WRI against proportion of buildings that experienced no damage after wildfire. The size of the circles plotted is proportional to the number of buildings in each WRI value.

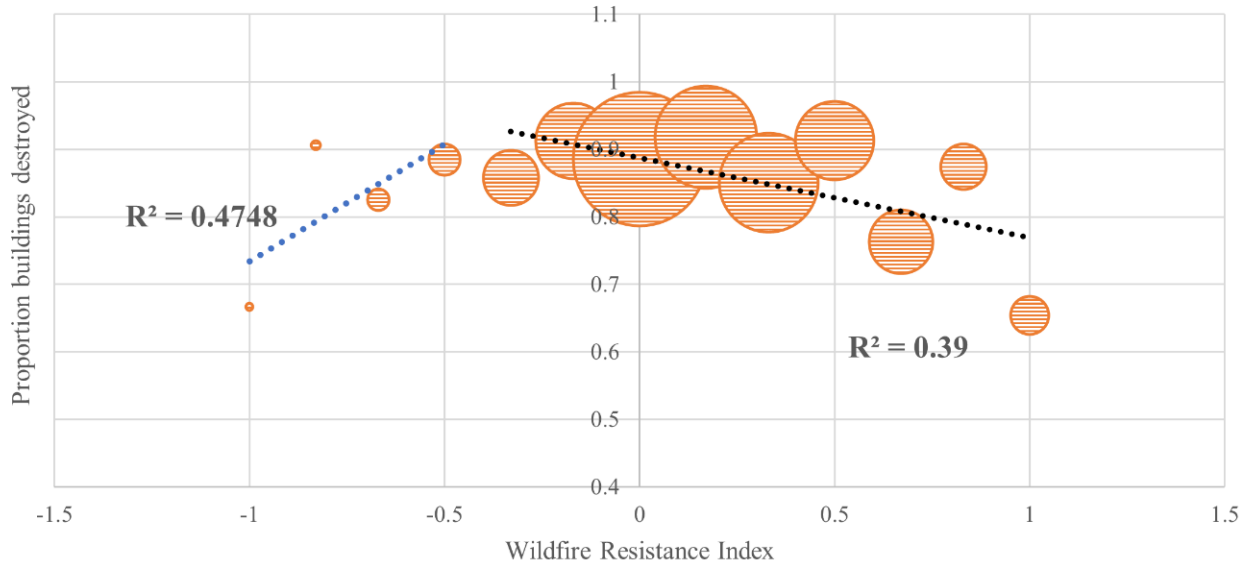

Figure 2-10: CAL FIRE data: WRI against proportion of buildings that were destroyed after wildfire. The size of the circles plotted is proportional to the number of buildings in each WRI value.

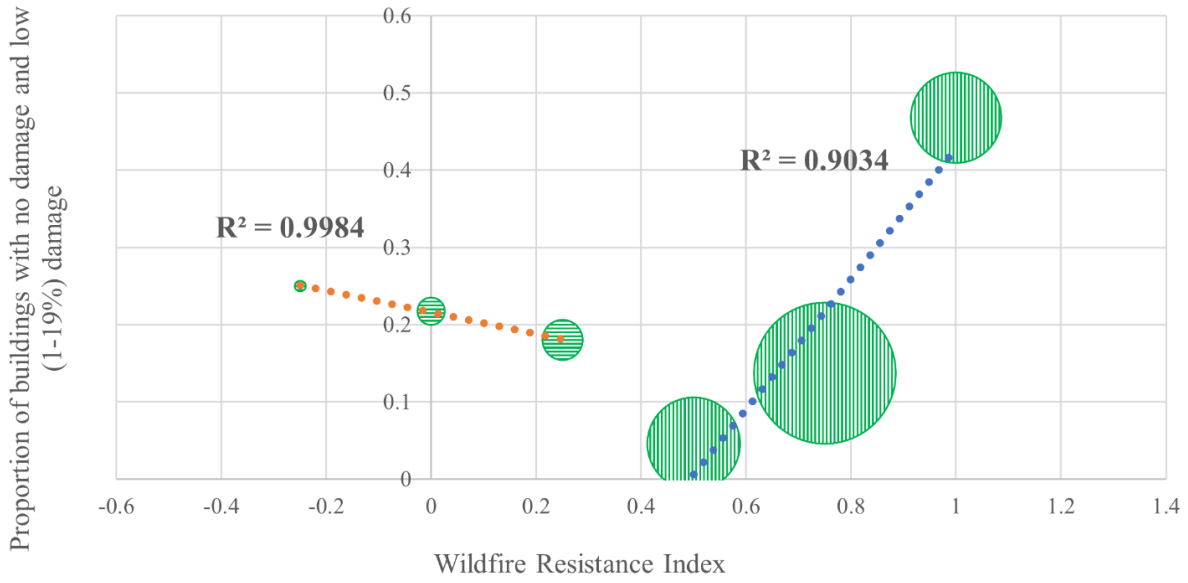

Figure 2-11: Pedrógão Grande data: WRI against proportion of buildings with no damage or low (1-19%) damage after wildfire. The size of the circles plotted is proportional to the number of buildings in each WRI value.

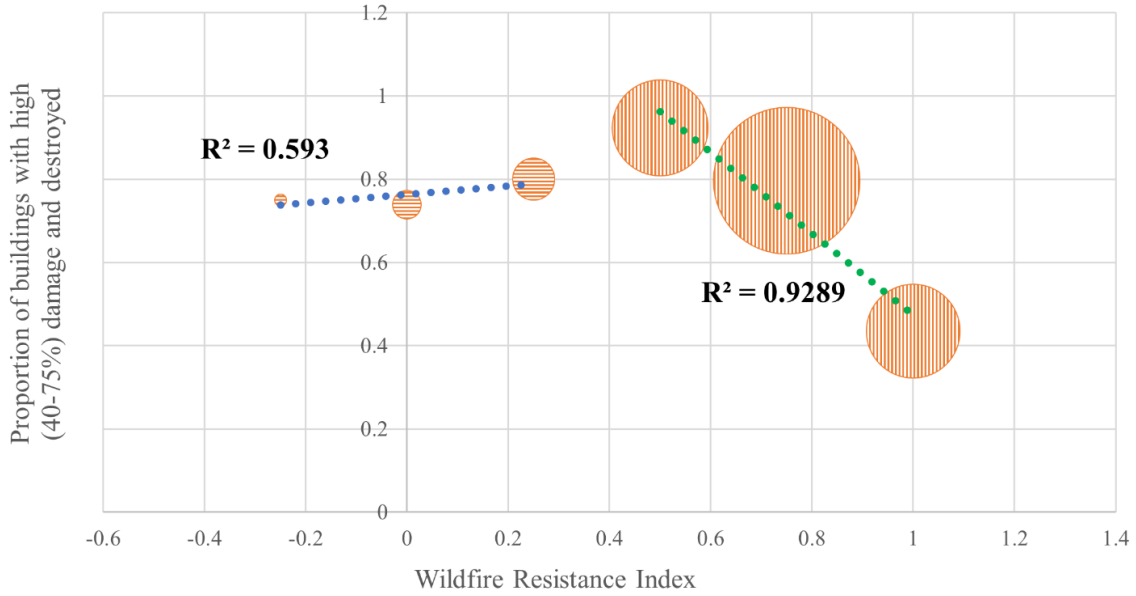

Figure 2-12: Pedrógão Grande data: WRI against proportion of buildings that had high (40-75%) damage and were destroyed after wildfire. The size of the circles plotted is proportional to the number of buildings in each WRI value.

In the Pedrógão Grande data analysis, shown in Figure 2-11 and Figure 2-12, the three highest WRI values (0.5, 0.75, and 1) include the largest sample size (>248 buildings), and give a positive linear correlation to proportion of 'no damage' and 'low damage' buildings with $R^2 = 0.90$. This correlation estimates, for a WRI increase of 0.5, an increase in proportion of no and low damage of approximately 42%. A negative linear correlation with $R^2 = 0.93$, is found between the same WRI values (0.5, 0.75, and 1), and the proportion of 'high damage' and 'destroyed' buildings. This correlation estimates that, for a WRI increase of 0.5, the proportion of highly damaged and destroyed buildings decreases by approximately 48%.

In the CAL FIRE data, and Figure 2-10, WRI values -0.33 to 1 include sample sizes ranging from 428 to 2909 buildings, while the WRI values < -0.33 have sample sizes < 294 buildings. For WRI values ≥ -0.33, less accurate linear correlations compared to the Pedrógão Grande data are found, which follow similar trends. A negative linear correlation ($R^2 = 0.39$) is found between increasing WRI values and proportion of 'destroyed' buildings. A positive linear correlation ($R^2 = 0.45$) is found between WRI and proportion of survived buildings. Although these R^2 values are significantly lower compared to the Pedrógão Grande, authors note that WRI =1 (corresponding to buildings with only fire-resistant features) is an outlier from both linear trends; thus reducing the R^2 value, and indicating a significantly higher proportion of survived and significantly lower proportion of destroyed buildings for these buildings. Authors also tested a WRI version which considers all CAL FIRE building features except 'Eave Geometry'; this was tested due to uncertainty in literature regarding the wildfire vulnerability of eaves. This WRI version resulted in more accurate correlations: a negative linear

correlation (R^2 = 0.76) between WRI values ≥ -0.33 and 'destroyed' buildings proportion, and a positive linear correlation (R^2 = 0.63) with proportion of survived buildings.

2.4 Discussion

2.4.1 Statistical dependence tests

All statistical methods employed, for both databases, rank deck material as one of the most highly correlated building features to damage, and rank roof material as a poorly correlated building feature to damage. Exterior material also ranks as highly correlated to damage in both databases, except for the Boruta feature method with the CAL FIRE database which ranks number of windowpanes as most correlated and exterior material as least.

The low ranking of the roof material relevance to wildfire damage disagrees with similar published index (PVI) applied to Mati, Greece post-fire data (Papathoma-Köhle *et al.*, 2022). Authors infer this difference is due to the amount of detail information included in the roof material data; the PVI roof material considers five possible materials, describing both the roof frame and tiles. The current WRI only considers two roof covering material options: i) Fire resistant and ii) Non Fire resistant material. Given the size and complexity of roofing systems, unconsidered details (e.g: design, accumulation of debris) may all contribute to wildfire damage. Furthermore a recent experimental investigation of firebrand accumulation on roofs concluded that the area where firebrands contact the roof is a complex function of the building shape, roof angle, and wind angle (Nguyen and Kaye, 2021).

The high-ranking correlation of the deck and exterior material variables supports the importance of defensible space in wildfire damage. The deck variable, in both databases, includes the differentiation between buildings with and without a deck, as well as what material the deck is primarily constructed of. These conditions directly relating to the building's defensible space condition. Furthermore, exterior wall material is primarily vulnerable to flame radiation and impingement, which are strongly impacted by the condition of the defensible space around the building. Including more detailed information on the condition of deck (e.g: amount and condition of combustibles) in future damage inspections can help further explore its relationship to wildfire damage (Quarles and Standohar-Alfano, 2018).

For the CAL FIRE database, vent screens and eaves geometry both rank with relatively high correlations to damage level. These features are both associated with firebrand exposure. Vent screens only protect from firebrand entry, and eave geometry increases building vulnerability to firebrands and flame impingement. Furthermore, deck vulnerability to firebrands has been extensively documented and investigated (Wheeler, 2004; Manzello and Suzuki, 2014; Meerpoel-Pietri *et al.*, 2021). These results can indicate the importance of firebrand exposure in building ignition and damage, agreeing with existing literature (Maranghides and Mell, 2012; Ribeiro *et al.*, 2020).

The disagreement in ranking the relevance of number of windowpanes between the Boruta feature selection method, and the Cramer's V and BF method, highlights the importance of testing various statistical dependence tests, and of standardising data collection to minimise variations. The amount of missing data in the original databases, as well as the lack of detail of certain building feature characteristics introduce limitations of the accuracy of statistical relevance ranking. This is quantified by the imputation out-of-bag error: approximately 20% for the CAL FIRE data, and 28% for the Pedrógão Grande data. Authors note missing data, and lack of detail are standard limitation of post-fire damage data given the complications of collecting vast and detail damage data of the field. Recommendations for future data collections include focusing on more detail for the roofing system, and standardising data collection with existing databases to allow comparison and extension of lessons learnt.

2.4.2 WRI

The WRI creates a WUI building fire protection index based on currently available post-fire building damage data. The correlations found between WRI and damage level confirm that including the greatest number of high fire protection features has a significant impact on increasing the building's wildfire survivability; emphasising the importance of holistic fire safety constructions rather than focusing on isolated building features. The Pedrógão Grande data linear correlations estimate, for a WRI increase of 0.5, a decrease in proportion of highly damaged and destroyed buildings of 48%, and increase in proportion of low or no damage buildings of 42% (correlation with R^2 of 0.93 and 0.90 respectively). These significant increases confirm that for Portuguese rural WUI buildings an increase in fire protection level of exterior wall material, deck material, preservation level, and roof material can significantly impact the survivability of buildings. Contrastingly, the CAL FIRE data WRI did not correlate as accurately with damage level (R^2 of 0.39 and 0.45), this can suggest that building vulnerability in California is more strongly controlled by factors not considered in the WRI (e.g.: building-to-building separation distance, defensible space condition). Buildings with a WRI of 1, corresponding to only having high-fire protection features, do exhibit exceptionally high proportion of survival (14.2% compared to an average of 5.13% for buildings with WRI ≥ -0.33), and exceptionally low proportion of destroyed buildings (65.4% compared to an average of 84.8 % for buildings with WRI ≥ -0.33). These outlier values suggest that buildings which incorporate higher fire protection characteristics for all building features are significantly more resistant to wildfire damage. Although a second WRI variation excluding 'eave geometry' building feature resulted in correlations with higher R^2 values to the proportion of destroyed and survived buildings, this trend was not included due to the statistical dependence tests results confirming 'eave geometry' significant correlation to damage level. Authors recommend careful assessment of what features to include in the WRI based on specific local building and surrounding characteristics.

The following WRI limitations can explain the variance in the data observed, and need to be considered and addressed prior to further application in fire spread models or as WUI building risk assessment tool; the WRI is not weighted, it only accounts for building construction features and maintenance level, and needs to be validated with more data to confirm correlations. In contrast to recently published PVI index (Papathoma-Köhle *et al.*, 2022), also due to this study's use of a significantly larger database, the WRI assumes all features considered contribute equally to the building vulnerability; this assumption is a limitation as in reality certain building features will contribute more significantly to wildfire ignition and spread. The decision to not weigh the various building features was made to calculate a baseline correlation when only considering the relative number features providing high fire protection, and due to disagreement in building feature ranking resulting from the statistical dependence tests conducted. The WRI only considers factors contributing to building construction vulnerability, as this is a clear gap in WUI vulnerability assessment methods in literature; if applied in WUI fire spread or damage models, authors recommend to also include calculation and correlation relating to the condition of building defensible space, e.g.(Hysa, 2021). Results indicate this might be especially valuable of California, or similar, WUI regions, compared to Portugal WUI regions. Lastly, the small sample size of buildings with low WRI values (maximum of 50 buildings of WRI < 0.5 in the Pedrógão Grande data, and maximum of 294 buildings of WRI ≤ 0.5 in the CAL FIRE database) poses limits to the validation; validating the methodology with more evenly distributed data can increase its value and accuracy. Authors note that small sample sizes and missing data are normal occurrences in post-fire damage databases given the difficulty of collecting relevant data in post-fire WUI.

Chapter 3 : Firebrand Exposure and Particulate Wind Transport

3.1 Wildfire Firebrands

Firebrands are airborne particles of burning fuel which aid wildfires in spreading quickly and often in unexpected directions. Firebrand ignition is often observed to be the leading cause of WUI building ignitions, both in post-fire inspections and experimental studies (Blanchi *et al.*, 2006; Hakes *et al.*, 2017; Ribeiro *et al.*, 2020). Figure 3-1 is a photograph of a wildfire in California, capturing the high number of firebrands produced and coming close to buildings and firefighters protecting the house from potential firebrand ignition.

Figure 3-1: Photograph of firebrands reaching a home, and firefighters protecting the building with water, during a wildfire in California. Photo by Ethan Swope, 2021.

The process of wildfire spread through firebrand ignition is called spotting and occurs when firebrands successfully ignite new fuel upon landing; thus spreading the fire (Koo *et al.*, 2010). Spotting includes different sub-processes occurring on different spatial scales. On the macroscale, large wildfires impact several hectares of land area, changing atmospheric conditions and sometimes creating formidable weather events. Firebrands can travel as far as several kilometres away; for example, Eucalyptus tree forest fires often generate firebrands which ignite secondary fires 8-10 kilometres away from the generating flames (Babrauskas, 2018), contributing to fast wildfire spread. Fast urban fire spread speeds of 0.28-0.39 m/s have been attributed to firebrand exposure and

ignition (Babrauskas, 2018). The mesoscale in wildfire spread and impact refers to one single residential building dimensions, which can span approximately 85 - 100 m², and experience firebrand generation, exposure and ignition. The forces and fire dynamics influencing single firebrands and their trajectory, on the other hand, occur on the microscale. Firebrand particles range in shape and sizes and have an average equivalent diameter of a handful of millimetres; literature on firebrand collection and characterisation is reviewed in section 3.1. This Chapter aims to clarify the significant physical parameters governing firebrand exposure and building ignition and damage, by learning from the research conducted on landscape-scale wildfire spotting and wind-driven sand transport. The most recent literature on firebrand exposure processes is summarised, and computational research methods applied to investigate particulate accumulation processes are discussed. The research presented is selected to best understand building scale firebrand accumulation and contact exposure. Firebrand exposure and ignition subprocess on buildings are schematically illustrated in a simple diagram in Figure 3-2.

Figure 3-2: Diagram of five stages of wildfire firebrand exposure and ignition of buildings: firebrand generation, wind-driven transport, landing and accumulation, ignition and fire spread.

Section 3.1 reviews the literature on firebrand generation, wind driven transport, ignition, and deposition and accumulation. Section 3.2 introduces the physical processes governing particulate transport, focusing on sand transport literature, as it is most applicable to wildfire firebrand deposition and accumulation. Section 3.3 provides the background on computational approaches to simulate particulate transport in wind, and justifies the approach adopted in this research to computationally investigate wildfire deposition and accumulation processes.

Generally, firebrand exposure literature has focused on characterising firebrand particle properties, applying aerodynamic models for short-range and long-range spotting, and defining firebrands ignition potential. Deposition subprocesses, which precede and determine firebrand accumulation around solid obstacles, have not been comprehensively explored in literature. After defining the WUI most vulnerable solid obstacles, or vulnerable WUI building features, in Chapter 1 and 2; Chapters 4, 5 and 6 aim to expand and computationally characterise knowledge on firebrand landing and accumulation processes on and around solid obstacles.

3.1.1 Generation

Firebrand generation is a complex phenomenon during which burning fuel, both vegetative and urban fuel, degrades due to combustion creating particles of various sizes and shapes which are lofted by the fire plume. The fuel material properties, condition, and distribution, as well as both the local ambient wind flow and fire-induced air and smoke flow influence the generating mechanisms and resulting particle properties (Manzello *et al.*, 2020). The methodologies adopted to research this phenomenon mostly include generating firebrands in field and laboratory fires under ambient or induced wind flow, and collecting firebrands during or post wildland and WUI fires events. Laboratory fires offer the benefit of controlling and recording conditions influencing the generation process; post-fire and field-scale firebrand analysis allow overall understanding of firebrand generation under diverse transient wildfire conditions, and allow validation of developed models and parameters relationships.

Here we summarise the most novel research approaches applied to investigate firebrand generation. Barr and Ezekoye created a numerical model describing firebrand generation from an idealised fractal geometry tree by coupling a mechanical breakage and thermal degradation model (Barr and Ezekoye, 2013). Tohidi et al. investigated the mechanical and thermal breakage mechanisms generating firebrands experimentally by exposing cylindrical wooden rods of three vegetative species and of different moisture contents to a Bunsen burner flame for set time lengths, extinguishing them, and measuring their mechanical properties using the three-point bending test (Tohidi *et al.*, 2017). Statistical models have also been studied to predict firebrand generation characteristics; Wickramasinghe et al. used inverse analysis, conducting randomly generated physics-based FDS simulations until experimental data matched results, to calibrate the impact of wind velocity, relative humidity, and vegetation species through interpolation technique (Wickramasinghe *et al.*, 2022). Himoto and Hayashi applied hierarchical Bayesian models to experimental data to retrieve probabilistic distributions for firebrand size and distance travelled (Himoto and Hayashi, 2022).

For the purpose of this research the review of firebrand generation focuses on the particle properties recorded necessary to accurately simulate landing and accumulation processes around solid obstacles, instead of reviewing breakage mechanisms models in details. To this end, Table 3-1 summarises relevant firebrand properties recorded, focusing on realistic wildfires and WUI fires firebrand collections, as well as field and full-scale experimental firebrand collection. Firebrand particles are characterised by mass and size distribution, number of firebrands, firebrand velocities and projected area. These characteristics impact the forces acting on firebrands during wind-driven transport and landing; therefore impacting trajectory, landing location, accumulation patterns, and potential exposure. Notably, only recently Hedayati et al. published an analysis and methodology for accurately analysing and reporting the wide range of particle properties distributions produced during firebrand generation; concluding the minimum sample size for defined statistical parameters is 1,400

firebrands and presenting an automatic image processing algorithm to facilitate large data analysis (Hedayati *et al.*, 2019).

Table 3-1: Firebrand generation studies collecting and recording firebrand particle properties from relevant vegetation and urban structures relevant for wildland and WUI fires.

Generating fuel	Study type	Data recorded	Reference
White Fire-Jeffery Pine	Post-fire analysis of firebrand burns on trampoline (WUI fire: Angora fire, USA in 2007)	• Firebrand size distribution (firebrand particle area) • >85 % of area of burned holes by firebrands < 0.5 cm^2	(Manzello and Foote, 2014)
Vegetation in Pinelands National Reserve	Experimental landscape-scale vegetation fires (Pinelands National Reserve in southern New Jersey, USA 2013-2015) Post-fire collection and thermal imaging during burns	• Type, velocity, size and number of firebrands recorded. Photos of firebrand shapes included. • ≥70% of firebrands bark fragments, the rest pine and shrub branches. • Firebrand mass range: 5 - 50 mg, most in 10–20 mg range. • ~80% of firebrands cross sectional area of (5–20) × 10^{-5} m^2 • Firebrand velocity distributed between 0.1–10.5 m/s (average = 2.5 m/s)	(Filkov *et al.*, 2017)
Forest (Pitch pine and oak trees), 3 most prominent understory species: huckleberry, blueberry and inkberry	Experimental landscape-scale vegetation fires	• Firebrand fluxes: 0.82–1.36 firebrands/$m^{-2}s^{-1}$ recorded for fire front of intensities: 7.35 ± 3.48 MWm^{-1} to 12.59 ± 5.87 MWm^{-1}. • Firebrand size distributions: most common size is 0.75–5×10^{-5} m^2 with corresponding 0.6-1 firebrands m^{-2} s^{-1} flux. • For firebrands of area > 5×10^{-5} m^2, fluxes are 0.2–0.3 firebrands m^{-2} s^{-1}.	(Thomas *et al.*, 2017)
Urban buildings; mostly of wooden construction materials and Japanese tile roofing.	Post-fire firebrand collection (urban fire: Itoigawa-city, Japan in 2016)	• Size and mass distribution recorded. • 60% of firebrands mass < 100 mg and projected area < 2.0 cm^2. • Comparison with literature data of other urban fire firebrands.	(Suzuki and Manzello, 2018)
Full scale roofing assemblies - Sheathing: oriented strand board (OSB) - Framing: Wood joists	Wind tunnel experiments under different wind speeds (6 and 8 m/s)	• Firebrand mass (average: 100 mg) • Projected area (average: 1.5 cm^2) distribution.	(Manzello *et al.*, 2019)
Douglas-fir, Grand fir Western juniper	Experimental tree burns (burning 1, 3, and 5 trees), varying moisture	• Number of generated firebrands and number of char marks generated dependent on the species of trees.	(Hudson *et al.*, 2020)

and Ponderosa pine trees	content (11 – 193%), induced wind with industrial fan.	• Grand fir generated highest number of char marks (15 marks $m^{-2}kg^{-1}$). Ponderosa pine generated lowest (2 marks $m^{-2}kg^{-1}$). • 30% of Western juniper firebrands left char marks, and 5% of the ponderosa pine firebrands did. • Moisture content, average tree DBH and tree height were most significant factors influencing generation.

3.1.2 Wind-driven transport

Firebrand wind-driven transport trajectory has been widely investigated through empirical and computational models, supported by experimental and post-fire investigation data. In wildfire events, the ignition of secondary fires by wind-driven firebrands is called spotting, the new ignited fires are called spot fires, and spotting distance references to the distance between the fire front generating firebrands and the spot fire location (Koo *et al.*, 2010). The focus in the literature has been on large scale wildfire transport dynamics, as these are most applicable to macroscale wildfire and urban spread dynamics (Koo *et al.*, 2010). Literature makes a distinction between short range spotting, which occurs when firebrands land and ignite fuel ≤750m away from the flaming fire front, medium range spotting (1-5 km away spotting from the fire front), and long range spotting (>5km spotting distance from the fire) (Wadhwani *et al.*, 2022). Especially when reviewing and operating empirical models, it is important to distinguish which spatial scale of spotting the model has been designed to predict. Literature identifies and models fire intensity, wind profile, topography, fuel material and condition, and firebrand shape and size as the most influential factors influencing firebrand transport (Wadhwani *et al.*, 2022); these factors are illustrated in Figure 3-3 diagram.

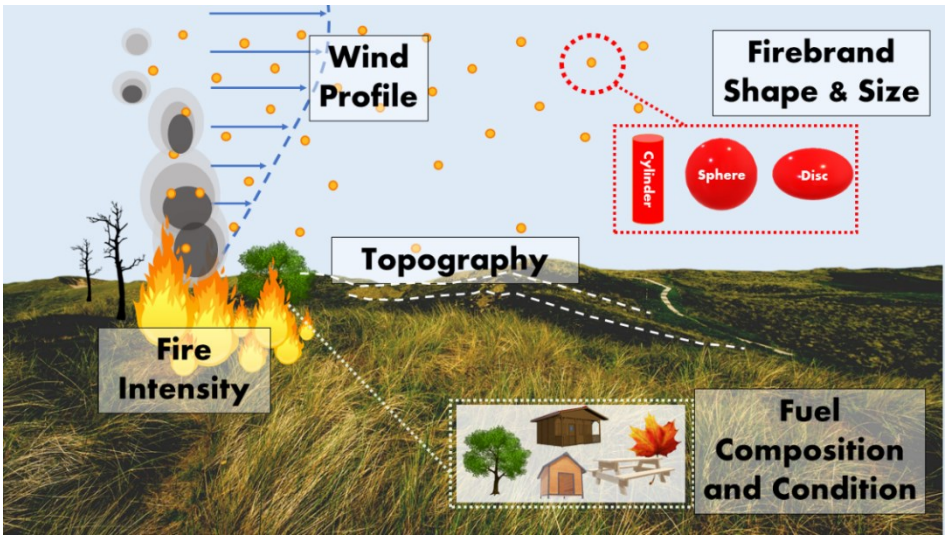

Figure 3-3: Landscape-scale illustration of wildfire spotting, most influential factors impacting firebrand transport are labelled.

The flowchart provided in Figure 3-4 illustrates how these parameters are interrelated; each arrow in the figure indicates the relationship between two variables, an influencing point to an influenced. Fuel properties (which, as mentioned in Chapter 1, include numerous diverse possible properties and conditions), landscape topography, and wind profile all influence the transient fire intensity of a given flaming wildfire front, which in turn influences the firebrand generation and lofting height of firebrands by determining the plume conditions and fire energy release. Once the firebrands are generated and after possible lofting by the plume, their shape and size distribution, as well as the local wind they interact with, will influence their wind-driven transport. The fuel material and condition are two of the most important factors influencing firebrand generation flux and shape and size (Hudson *et al.*, 2020).

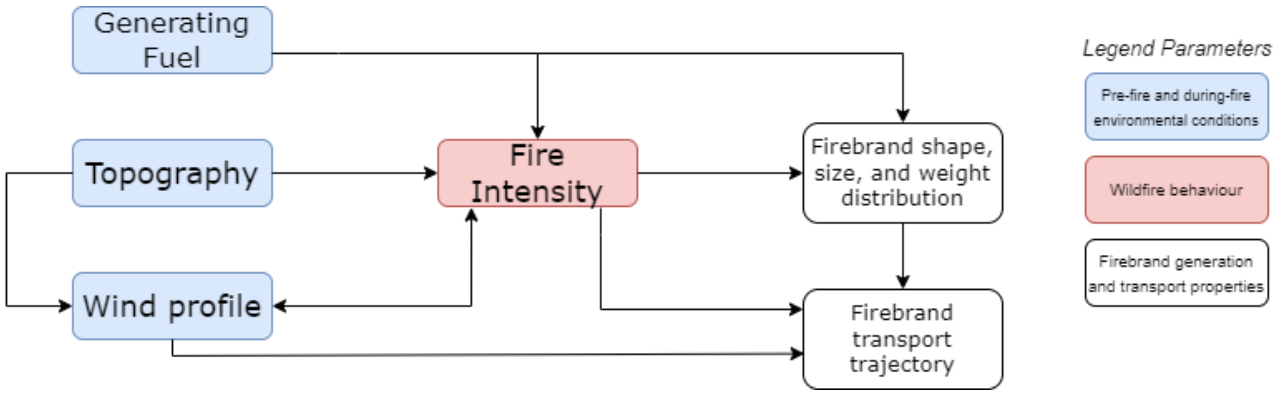

Figure 3-4: Flowchart of influencing relationships of different environmental factors involved in wildfire occurrence and wildfire firebrand generation and transport phenomena.

In this section we give a brief introduction to empirical and experimental research on firebrand transport, and end by focusing on computational firebrand transport research. In an effort to quantify and predict the relationships introduced in Figure 3-3 and Figure 3-4, empirical models of spotting parameters have been developed based on experimental and wildfire observations. McArthur measured the wildfire rate of spread (ROS), flame height, and spotting distance under different weather conditions and fuel loads; and developed Equation 5 to estimate the spotting distance (S) based on rate of spread (ROS), fuel load in [tons/ha] (W) for fuel eucalyptus forests (McArthur, 1967).

$$S = ROS(4.17 - 0.033W) - 0.36 \qquad \textit{Equation 5}$$

Tarifa et al. executed innovative wind tunnel experiments on firebrands combustion and transport properties in convective columns and during wind-driven transport (Tarifa *et al.*, 1967). This research concluded that firebrands can be studied as always falling at their terminal velocity and that the drag coefficient does not change significantly over the transport trajectory. Tarifa et al. also experimentally deduced the drag and combustion rates of spherical, cylindrical, and disc-shaped particles of various wood species. This work was progressed by Lee and Hellman (Lee and Hellman,

1970), Muraszew et al. (Muraszew *et al.*, 1977) and Albini (Albini, 1979, 1981, 1983) who developed operational models for maximum firebrand spotting distance for various fire conditions.

The general methodologies used to predict the forces acting on firebrand particles combine plume correlations or CFD simulations with drag coefficients to approximate the vertical lofting force, and with wind profile approximations and drag coefficients, to approximate the horizontal forces. Details of the mathematical equations describing these processes are discussed in section 3.2 and 3.3. These approaches require information about firebrand particle characteristics, wind profile, and plume behavior. Table 3-2 lists the most significant published CFD models for firebrand transport, and qualitatively describes their different approaches and assumptions. Authors note that CFD simulations for firebrand transport in the past have often focused on medium and long-range spotting, and given particular attention to the interaction and influence of the wildfire plume with firebrand transport. This approach is especially relevant for landscape wildfire macroscale spread investigations.

Table 3-2: List of relevant Computational Fluid Dynamic (CFD) models of firebrand transport

Reference	Model description and discussion
(Tse and Fernandez-Pello, 1998)	• Numerical models of transport trajectories of copper and aluminium particles simulating sparks from power cables, and of wood firebrand particles. • Approach resolved the equations of motion for Newtonian particles considering drag force and gravity. • Metals particles are assumed to have initial temperature equal to their melting temperature, and the lumped capacitance assumption is applied to solve the transient energy equation. • For given initial height different particle trajectories are computed for different conditions and wood firebrands are found to show the longest spotting distance.
(Woycheese and Pagni, 1999)	• Transport model for combusting wood disc-shaped firebrands. • A stagnation-point combustion model is applied after reviewing eight published firebrand combustion models. • Lofting height and firebrand size relationship is calculated and presented. • Firebrands are assumed to loft in the centre of an axisymmetric pool fire, in constant wind conditions. • Maximum spotting distances based on firebrand thickness, burning parameter, constant wind speed, and angle of attack are calculated.

(Himoto and Tanaka, 2005)	• CFD model using Large Eddy Simulations (LES) of disc-shaped firebrand transport. • Momentum (including drag, gravitational, and lift force effects) and angular momentum conservation equations are solved simultaneously. • Three firebrand densities (50, 100, 150 kg/m^{-3}) are tested and the landing distribution in terms of the injection height is presented. • Assumes heat release of 4.0 kW uniformly distributed in the cells above ground boundary, and firebrands released in a turbulent boundary layer.
(Sardoy *et al.*, 2007)	• Disc-shaped firebrands are injected in calculated crown-fire induced thermal, plume, and wind flow fields. • The firebrand burning characteristics are preliminarily studied. • The transport trajectories and burning rates of firebrands are calculated for different wind speeds and fire intensities. • Firebrands that reach the ground are characterised as either experiencing flaming or smouldering combustion.
(Koo *et al.*, 2012)	• Firebrand transport of cylindrical and disc-shaped particles is modelled and analysed using different assumptions for firebrand transport and combustion by simulating their trajectories in coupled-physical fire simulator HIGRAD/FIRETEC. • The force dynamics during transport phase for both shapes of firebrand particles are developed balancing the influence of drag, gravitational, and lift forces acting on the firebrand particles. • Tests assumption that firebrands are always traveling at their terminal velocity, and concludes this assumption significantly impacts firebrand trajectory in the case of non-steady inhomogeneous plumes which occur in real wildfire scenarios. • The combustion impact on firebrand particle shape, and therefore aerodynamics, is simulated through mass loss in different directions; discs experiencing axial regression and cylinders experiencing radial regression show the highest impact of firebrand transport trajectories, discs with radial regression and cylinders with axial regression illustrate combustion has no effect on firebrand transport.
(Tohidi, 2016)	• Tohidi's PhD dissertation investigated aspects of non-combusting cylindrical firebrand generation and transport experimentally and computationally.

	• Downwind transport of non-combusting firebrands is found to be highly sensitive to the initial conditions of firebrand release (angle and location) as well as temporal and spatial variations of the ambient wind flow field. • An LES model to simulate the wildfire wind flow field coupled with a published deterministic 6 degrees of freedom firebrand transport model. Model is validated with wind tunnel experimental measurements.
(Thurston *et al.*, 2017)	• Created wildfire plume simulations using the UK Met Office LES and coupled an offline Lagrangian particle model to plume simulation results to solve for firebrand particle trajectories. • The plume was simulated by introducing a heat source in a turbulent atmospheric boundary layer; the plume flow field was then used to model firebrand transport under ambient wind speeds varying between 5 – 15 m/s. • With low ambient wind speeds firebrands are observed to be lofted higher and have a residence time between 5 and 30 minutes. This is interpreted as having lower spotting risk as most firebrands are expected to burn out before landing. • With high ambient wind speeds, firebrands are observed to land outside of the plume more easily. Once leaving the plume, firebrand trajectory is observed to be independent of plume dynamics. Firebrand lateral spread is significantly lower compared to low-ambient wind cases.
(Moinuddin and Wadhwani, 2019; Wadhwani *et al.*, 2022)	• Wadhwani investigated short range firebrand transport experimentally and numerically in a series of publications expanding understanding of firebrand transport. • Through a new firebrand generator desgin producing repeatable sets of firebrand particle exposure, a numerical model describing the transport of burning and non-burning cubiform firebrands at two flow speeds is validated. • Four drag sub-models estimating drag coefficients are used in the numerical model and compared to experimental results to quantify their applicability for different conditions. • This validation research has been extended to a larger (1 km long) computational domain simulating firebrand in an idealized wildfire exposure scenario including forest canopy.

3.1.3 Ignition

When burning firebrands land on target fuel and transfer enough heat, they ignite the target fuel, completing the spotting process. Ignition of fuels is a complex process involving heat transfer, chemical kinetics of the pyrolysis and combustion reactions involved, and fluid mechanics influencing

the heat transfer in question. As firebrands are burning they most often experience smouldering, flameless or glowing, combustion which is a result of the heterogeneous oxidation of solid fuel (Santoso *et al.*, 2019). The number, size, mass, and energy of firebrands, the condition of the target material and surrounding environment, all contribute to whether and which type of ignition will occur. Figure 3-5 shows a schematic of the simplified energy balance presented in firebrand ignition studies; burning firebrands are generating heat through a combustion reaction occurring with firebrand material and possible pyrolyzate gases as reactants, and losing heat through convection and radiation to the surroundings; if in contact with solid target fuel, the firebrand will lose heat through conduction to the solid (Wessies *et al.*, 2019). This simplified energy balance is mathematically shown by Equation 6, where m_f is the firebrand mass, c_f is the firebrand specific heat, $\dot{Q}_{rxn}$ refers to the heat generated by the firebrand through combustion and pyrolysis reactions, $\dot{Q}_{rad}$ is the radiative heat loss, $\dot{Q}_{conv}$ is the convective heat loss to the surrounding air, and $\dot{Q}_{cond}$ is the combined conductive and radiative heat losses to the target fuel. The firebrand mass (m_f) will also be changing with time, due to firebrand fuel reacting in the reactions; this change is slower compared to the change in temperature and therefore often assumed to stay constant.

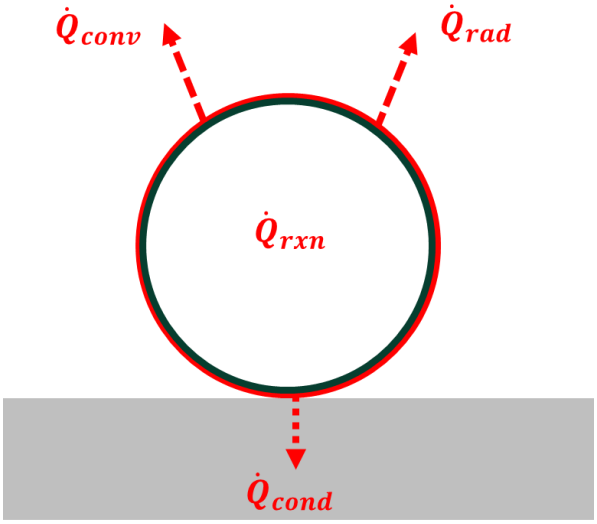

Figure 3-5: Schematic of simplified heat balance of hot firebrand particle in contact with target fuel. Arrows show heat losses through convection and radiation to surroundings, and conduction to the target fuel. Adapted from (Wessies et al., 2019).

$$m_f c_f \frac{dT}{dt} = \dot{Q}_{rxn} - \dot{Q}_{rad} - \dot{Q}_{cond} - \dot{Q}_{conv} \qquad \textit{Equation 6}$$

Studies have investigated the necessary firebrand mass and temperature to ignite various materials including: structural wood (Santamaria *et al.*, 2015), and fuel beds with varying properties, such as water content, vegetation type, and geographical origin (Hadden *et al.*, 2011; Viegas *et al.*, 2014; Urban *et al.*, 2019). This section focuses on reviewing firebrand ignition research related to firebrand accumulation and firebrand building ignition, as this most directly relates to this thesis.

Kwon and Liao experimentally measured the influence of spacing distance between flaming and smouldering firebrands on their combustion dynamics observing that decreasing the spacing increased flame height and mass loss rate until eventually air entrainment limited combustion, smouldering firebrand groups were also observed to burn hotter and longer compared to single samples (Kwon and Liao, 2022). This comprehensive experimental investigation confirms why the accumulation of firebrands increases their spotting and ignition risk. Although after a certain threshold of spacing between firebrands the air entrainment limited the ongoing combustion reaction, in a high wind flow environment this restriction is likely to be avoided, and the close proximity of smouldering and flaming firebrands is likely to increase the probability of firebrand ignition of target fuel.

Larger-scale experiments have been investigating the probability of firebrand ignition on vulnerable structural elements, focused on wildfire firebrand ignition of WUI buildings. The NIST dragon is an experimental apparatus which creates a continuous feed of adaptable speed airflow with burning firebrands matching the size and mass flux distribution of real wildfire scenarios; thus allowing the experimental investigation of realistic firebrand exposure (Manzello and Suzuki, 2013). This apparatus has been used to study the response of many building targets, including roofing assemblies (Manzello, Hayashi, *et al.*, 2010), wall sidings and eaves set ups (Manzello *et al.*, 2012), decking assemblies (Manzello and Suzuki, 2014), and fences (Suzuki *et al.*, 2016). The combined exposure effect of radiative heat flux and embers on ignition of fuel has been recently studied through laboratory experiments using the NIST dragon, providing more detail and insight of the detailed heat transfer dynamics which create firebrand ignition risk (Suzuki and Manzello, 2021a).

Experiments of firebrand ignition have also been designed by directly placing burning firebrands on investigated structural fuels to observe the response. Meerpoel-Pietri et al. experimentally compared the ignition propensity of two decking materials used in WUI constructions in France to firebrand ignition; the research presents the location, minimum firebrand mass, and minimum firebrand number observed before ignition for wooden and thermoplastic decking materials (Meerpoel-Pietri *et al.*, 2021). Wessies et al. experimentally tested the firebrand ignition propensity of various attic insultation materials used in WUI constructions (polyurethane foam, expanded polystyrene (EPS), extruded polystyrene (XPS), denim, and cellulose) (Wessies *et al.*, 2019). In these experiments two firebrand exposure patterns are compared: a single firebrand or five firebrands of equal total mass; the five separate firebrands more consistently ignited the materials.

This brief overview of firebrand ignition literature highlights the different scales at which firebrand ignition can be investigated. On a smaller scale, it is possible to zoom in to the firebrand exposure configurations and specific material response. Firebrand ignition has also been investigated on a larger scale by mimicking the continuous feed within a wind flow and the exposure of firebrands on component-scale size assemblies of various building components. All types of investigations are

needed to address different research questions and provide insight in the material and component response of WUI constructions.

3.1.4 Deposition, creep, and accumulation

In both indirect (firebrands ignite building-adjacent fuel, resulting in spot fire which ignites the building) and direct (firebrand ignite building component or interior) ignition pathways, the location and the amount of firebrands that come to contact with the building fuel are significant in characterizing firebrand exposure and, therefore, ignition risk. Firebrand accumulation refers to the process of firebrands reaching stationary state due to the local solid boundary and flow field characteristics. When these local conditions cause firebrand particles to cease moving and remain stationarily in contact with target fuel, firebrand particles will group together and the probability of transferring enough heat to ignite target fuel is elevated. Between firebrand wind-driven transport and ignition, firebrands experience different landing subprocesses that determine where firebrand accumulation will occur.

Figure 3-6 illustrates the landing subprocesses we have identified as significant in firebrand exposure: firebrands first deposit when they contact a solid obstacles, subsequently firebrands creep, moving adjacently to the solid obstacle, and lastly firebrands accumulate when they reach a stationary position, grouping with other firebrands. These landing subprocesses have been explored to varying extents in firebrand exposure literature both numerically and experimentally, with a specific recent focus on firebrand accumulation regions. Firebrand exposure research is increasingly focusing on accumulation near building and direct building ignition as the impact of wildfire firebrand ignition on WUI areas continues increasing.

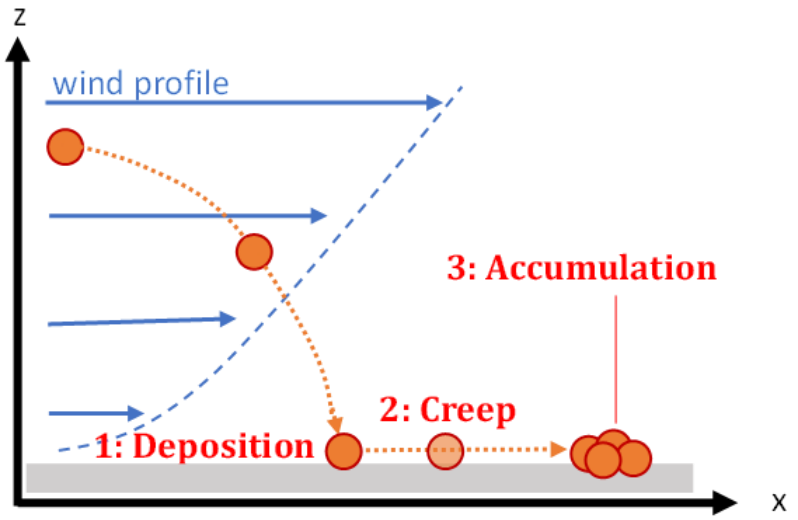

Figure 3-6: Schematic diagram of significant firebrands landing subprocesses: deposition, creep, and accumulation.

Anthenien et al. presented a numerical model considering the wind-driven trajectory for spherical, cylindrical, and disk firebrands landing on different terrain conditions. Although considering the impact of terrain conditions and roughness on the wind profile begins considering the factors influencing landing subprocesses, this approach still only considers the first deposition location of firebrands, a common practice in firebrand transport studies (Tse and Fernandez-Pello, 1998; Anthenien *et al.*, 2006). Firebrand deposition around cubic obstacles has been modelled using the Fire Dynamics Simulator (FDS) CFD software; this work initiated computational numerical simulations of firebrand deposition around solid obstacles, investigating the interactions between wildfire firebrand transport and possible WUI target fuels (Mankame and Shotorban, 2021).

Experimentally, Suzuki and Manzello have published two wind tunnel experimental investigations of firebrand accumulation patterns around solid obstacles using the NIST dragon firebrand generator; these studies observed the accumulation process around a vertical wall of varying heights, and two cubic obstacles with varying spacing distance (Suzuki and Manzello, 2017, 2021b). Wind tunnel experiments were also conducted to investigate the firebrand accumulation and deposition patterns on WUI building roofs of different geometries, and the impact of surrounding buildings on this accumulation (Nguyen and Kaye, 2022b). Recently, full-scale building wind tunnel experiments at 10.3 m/s and 14.3 m/s were conducted to observe firebrand accumulation and its influencing factors (Quarles *et al.*, 2023); results agreed with smaller scale observations that higher wind speeds increased the amount of firebrands reaching and accumulating around the building. Furthermore, observations indicated that when firebrands are involved in flow recirculation zones which form around the building, they are likely to travel down toward the ground surface thus promoting accumulation especially when the surface is characterised by high roughness.

The most significant factors influencing firebrand accumulation have been qualitatively identified as building geometry, local wind field conditions, and ground surface roughness characteristics (Quarles *et al.*, 2023). A significant portion of the presented research is dedicated to quantifying and scientifically explaining the impact of local flow field, and solid obstacle geometry on firebrand accumulation process on a building-component scale size. Section 3.2 and 3.3 of this chapter aim to provide in-depth theoretical physical background regarding these factors' influence on firebrand accumulation, and Chapter 4 and 5 present computational simulations of firebrand landing subprocesses under various conditions.

3.2 Particle Transport in Wind: Physical Mechanisms

Particulate transport in fluid flow has been investigated and characterised for a number of applications for a wide range of particle characteristics and fluid flows (Wadhwani *et al.*, 2022). Scientific fields which have investigated this phenomena include pollutant particle movement in human lungs (Tsuda *et al.*, 2013), solid-gas mixtures flow through pipes and reactors , deposition of aerosol particles on surfaces in manufacturing. The most transferable research topics to firebrand

exposure and hazard are sand and snow movement and hazard to infrastructures investigations; which deal with a similar spatial scale of particles and landscapes (Giudice *et al.*, 2019). This section describes the general physical processes involved in particulate transport in gaseous flow and deposition on solid surfaces. Starting from the general physical mechanisms which govern particulate transport and deposition, and transitioning to recent relevant research methodology and findings, this section provides an overview of the mechanisms involved in firebrand transport and deposition with the objective of describing the physical phenomena, identifying the most significant influencing parameters, before justifying the computational approach utilised in this thesis in section 3.3.

3.2.1 Solid Particles and Fluid Flow

There are a number of particle properties influencing solid-gas mixture transport. Here we give an overview of these properties and how they influence particle transport and deposition, relating to wind-driven firebrands. The focus of this overview is to isolate and contextualise firebrand particles physical processes in the wider field of particulate fluid transport.

Particle density and shape are the two most commonly measured properties in wildfire firebrand collection studies, and important influencing parameters of particulate transport and deposition. Both parameters' significance varies depending on the particles size ranges and the transporting fluid properties. An important particle size threshold is the relative size between particle diameter and the gas molecules mean free path; the ration between these two values is known as the Knudsen number, given by Equation 7 where Kn is the Knudsen number, d_p is the particle diameter, and ℓ is the mean free path between gas molecules (Tsuda *et al.*, 2013).

$$Kn = \ell / d_p \qquad \textit{Equation 7}$$

When Kn is significantly larger than 1, describing the particle movement behaviour requires integrating the kinetic theory of gases; alternatively when the particle diameter is significantly larger than the gas molecules mean free path, the gas impact on particle transport is mainly through the drag force, as is explored in more detail in the next section. For wildfire firebrands, estimating an ℓ value of 9×10^{-8} m (assuming standard pressure, a temperature of 40°C, and CO_2 gas molecules) and taking the smallest firebrand particle average diameter from literature, 8×10^{-3} m (Filkov *et al.*, 2017), gives $Kn = 1.1\times10^{-5}$ which is significantly smaller, approximately 8.9×10^{4} times smaller, than 1.

When particle size and weight are below a certain threshold, particles remain suspended in gaseous fluids and are defined as aerosol particles (Liu, 2009). Suspension is caused by the collisions between small particles and air molecules, which overcomes the force of gravity. General size threshold in literature characterise particles with d_p < 0.001 mm as aerosols which do not deposit in turbulent fluid flows, and take as long as days and weeks to deposit in low speed flows (examples include viruses, tobacco smoke, soot); particles with 0.001mm < d_p < 0.1mm will deposit slowly, usually with sedimentation velocities > 0.2 m/s and include fine dust and ice crystals (Liu, 2009).

Lastly, particles with d_p > 0.1 mm belong to the largest range of airborne particles, exhibit sedimentation velocities > 0.5 m/s and include larger sand grains, rain drops and wildfire firebrands which, as covered in section 3.1.1, range between diameters of 4 – 10 mm.

Firebrand particles shape vary significantly; wildfire firebrands have been observed as having generally cylindrical (usually formed from burning branches and bark burning), spherical, and disc shape (most often associated with buildings and structural fuel burning) (Koo *et al.*, 2010). For irregularly shaped particles the equivalent diameter, defined as the diameter of a sphere of equivalent volume size to the particle, is often used to characterise particle size. Although the general firebrand shape can be characterised as closely relating idealised geometrical shapes; wildfire firebrand particles have irregular shapes due to the heterogeneity of vegetative fuel composition, condition, and the nature of firebrand generation mechanism.

A useful parameter to quantify the relative irregularity of a particle shape is its sphericity (ψ). Sphericity is the ratio of the surface area of a sphere with equal volume as the particle, to the particle surface area (Chhabra *et al.*, 1999). The higher the sphericity ratio, the more accurate are spherical particle assumptions, in drag calculation. In this research we focus on idealised spherical particles, focusing on the surrounding conditions influencing particle deposition, creep movement and accumulation; equivalent diameter and sphericity description can be used to extend presented results to research involving more complex firebrand particles shapes in the future.

The particulate transport and deposition in influenced by ambient wind flows (e.g.: sand, dust, snow, firebrands) occur inside the Atmospheric Boundary Layer (ABL); the ABL is the lowest layer of our planet's atmosphere, it has varying height generally under 2 km above Earth's surface and characterised by high turbulence (Randerson, 1978). Although accurately simulating the ABL flow is challenging, research advancements in this area have provided guidelines and insight into the flow development and characteristics under various influencing parameters – the roughness of the ground being one of the most significant ones (Giudice *et al.*, 2019). Assuming a flat ground surface, and minimum thermal stratification influence, the ABL wind flow equilibrium mean velocity profile can be described by Equation 8 where ϗ is the Von Karman constant, z_0 is the roughness length, and $\overrightarrow{u_*}$ is the friction velocity**.**

$$\left|\overrightarrow{\vec{u}(z)}\right| = \frac{\overrightarrow{u_*}}{ϗ} log \frac{z+z_0}{z_0} \qquad \textit{Equation 8}$$

3.2.2 Particulate Transport Mechanics

Different forces acting on and between the particles and fluid medium result in specific particle movement and trajectories; here we list and explain the primary forces considered in research studies on particulate transport. Forces significant in aerosol particle transport, for example Brownian diffusion is the dominant transport mechanism for particles of diameter smaller than 0.1μm travelling over short distances (Liu, 2009) are not considered. Firebrand particles, especially those carrying

enough thermal energy to pose ignition hazard, are not aerosol particles, and have significantly higher dimensions and mass; these forces are therefore not considered or significant.

F_g is the gravitational force, F_d is the drag force which is present whenever there is a difference in fluid velocity and particle velocity, by the fluid on the particles in the direction parallel to fluid flow, and F_b is the buoyancy force, the force exerted by displaced fluid in the opposite. Equation 9, Equation 10, and Equation 11 provide the equations for these forces respectively; where the parameters necessary for calculation are particle mass (m_p) and gravitational constant (g) for the gravitational constant; the particle drag coefficient (C_D), particle area (A_p), fluid density (ρ_f), and relative velocity between local flow and particle velocity (v_R) for the drag force acting on the particle; fluid density (ρ_f), particle volume (V_p) and gravitational constant (g) for the buoyancy force acting on the particle.

$$F_g = m_p g \qquad \textit{Equation 9}$$

$$F_d = \frac{1}{2} C_D A_p \rho_f v_R^2 \qquad \textit{Equation 10}$$

$$F_b = -\rho_f V_p g \qquad \textit{Equation 11}$$

These equations clearly illustrate the relationship between the magnitude of the forces experiences, and the size and weight of the particle. A lift force also acts on particles in the direction perpendicular to fluid flow; this force is specifically significant for aerofoil shapes, and its significance depends on particle geometry and conditions. Although lift force can act on spherical particles in shear flows near solid surfaces; it is often neglected for spherical particles and for all free-falling particles.

Particle movement calculations are usually first validated by looking at particle falling in a stationary fluid: particles first experience acceleration until the drag and gravitational force balance, then the particle reaches a constant falling velocity called terminal or sedimentation velocity given by Equation 12. Terminal sedimentation velocities of various vegetative firebrand materials was tested for non-burning material samples, and presented ranging between 1.3 – 5.6 m/s (Babrauskas, 2003).

$$u_t = \sqrt{\frac{2gm_p(\rho_p - \rho_f)}{\rho_p \rho_f A_p C_D}} \qquad \textit{Equation 12}$$

Once the particle reaches the solid ground, through deposition, the energy it is carrying from its transport is transferred partially tangentially to the ground surface through friction force, given by Equation 13; calculated with the friction coefficient (μ) and the normal force acting on the particle (N).

$$F_f = \mu N \qquad \textit{Equation 13}$$

Figure 3-7 provides a simple schematic illustrating how these different forces act on an idealised spherical firebrand particle once the particle comes to contact with a straight solid surface perpendicular to the ground. A number of additional complexities including the influence of irregular

shapes of the particles, the particle heat transfer and mass changes occurring due to the smouldering combustion, and the roughness and geometrical complexities of the solid ground surface, are influencing particle movement.

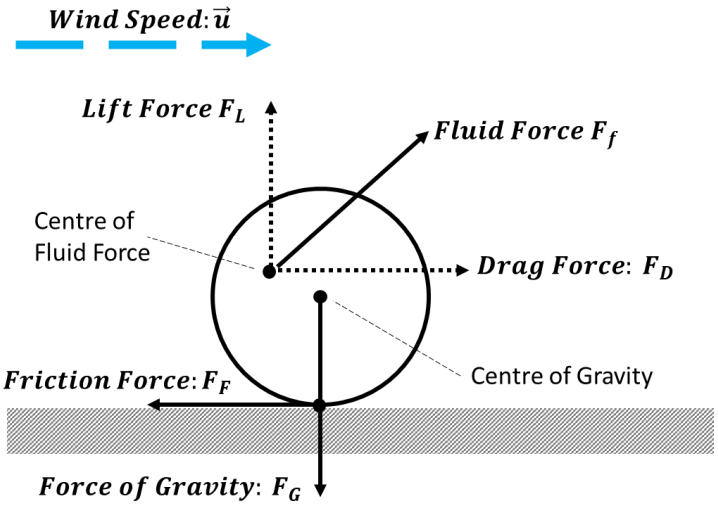

Figure 3-7: Schematic diagram of different forces acting on idealised spherical firebrand particle moving along a ground solid surface.

3.2.3 Sand Transport Modes

Following the general theory on the physical properties and forces influencing particulate transport in gaseous flow, this section focuses on the research conclusions from sand transport field to conclude the significant lessons and principles applicable to wildfire firebrand deposition. Different transport modes have been identified for the different movements experienced by sand grains in wind flows: suspension, saltation, reptation and creep. These transport modes influence and are experienced by particles depending on their sizes. The movement characterisation for particles with diameters in the following ranges are: suspension (d_p < 0.07mm), saltation and reptation (0.5 > d_p > 0.07mm), and creep (d_p > 0.5mm) (Kok *et al.*, 2012). Suspension lifts smaller particles and entrains them in the lower atmosphere. Saltation is considered the dominant transport mode for sand and refers to a series of parabolic trajectories experienced by the grains which, upon landing, cause more particles to lift and experience reptation. Reptation refers to a shorter, usually below 1cm, hop from the ground sand bed. Due to significantly larger size range of hazardous firebrands (~4-10 mm), the most applicable transport mode leading to accumulation is creep, particle movement through rolling or sliding along solid obstacle surface (Giudice *et al.*, 2019). Saltation is initiated when the wall shear stress (τ) where the particles or grains are resting exceeds a specific threshold, dependent on particle properties, under the local wind flow.

The forces discussed in section 3.2.2 determine which size range particle will experience specific types of transport dominating particle movement. Bagnold's pioneering book "The Physics of Wind

Blown Sand and Desert Dunes" began the experimental and theoretical research which set the basis to characterise these different transport modes mathematically (Bagnold, 1974). Bagnold first proposes an estimation of this threshold by equating the competing drag and surface friction forces acting on the particle. This static threshold concept can and has been applied to the threshold values for firebrand accumulation; inversely looking at the lowest wind speed needed for friction to overcome drag. Recent experimental investigations of firebrand accumulation by Suzuki and Manzello calculated this threshold velocity specifically for Douglas-fir and Japanese Cypress wood particles accumulating on gypsum board (Suzuki and Manzello, 2022). Equation 14 calculates this threshold by equating forces; where C_D is the drag coefficient, ρ_a is the air density, v_R is the relative velocity between the particle movement and local air flow velocity $A_p$the area of the particle experiencing the drag force, μ is the frictional coefficient, m_p is the particle mass, and g is gravitational force. For spherical non-burning particles, this balance is expressed by Equation 15 and simplified to Equation 16.

$$\frac{1}{2}C_D\rho_a v_R^2 A_p = \mu m_p g \qquad \textit{Equation 14}$$

$$\frac{1}{2}C_D\rho_a v_R^2 \pi r^2 = \mu\rho_p(\frac{4}{3}\pi r^3)g \qquad \textit{Equation 15}$$

$$v_R = \sqrt{\frac{8\mu g}{3C_D}\frac{\rho_p}{\rho_a}r} \qquad \textit{Equation 16}$$

Equation 16 is solved for particles with 50 kg/m³ density (as particles simulated in Chapters 4, 5, and 6) for three magnitudes of $\frac{\mu}{C_D}$, the resulting relationship is presented in Figure 3-8. The frictional coefficient, μ depends on the particle and ground material properties, and the drag coefficient C_D on the Reynolds number characterising flow and particle interactions.

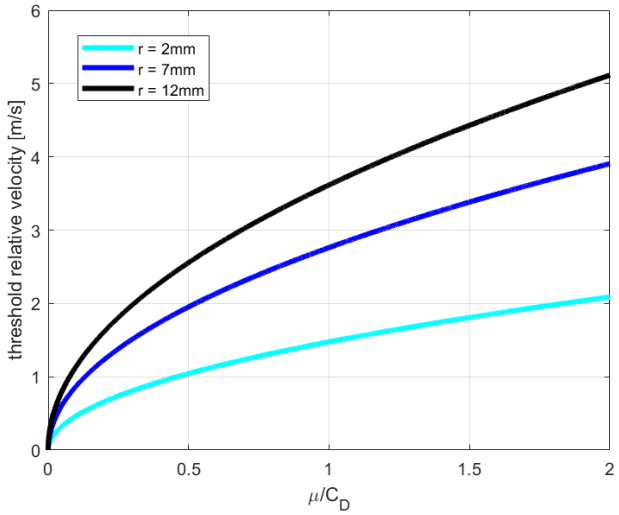

Figure 3-8: The relationship between $\frac{\mu}{C_D}$ and the threshold relative velocity for creep movement of spherical particles of 50 kg/m³ density and three particle radii magnitudes 2, 7, and 12 mm.

Since Bagnold's pioneering work, experimental data has continued to be collected and analysed and new models, both empirical and physical have been developed. Two different wind threshold velocities have been identified: a statistic threshold which is more relevant to stationary granular beds, like sand beds, where from a stationary stance wind initiates movement of, and dynamic threshold which is the minimum wind speed for sustaining transport of particulate matter, more relevant for the case of wildfire firebrand exposure. An analytical solution for the dynamic threshold speed was developed by Kok and given by Equation 17 (Kok, 2010).

$$u_{dt} = \left(\frac{700}{P}\right)^{\frac{1}{6}} \left(\frac{220}{T}\right)^{\frac{2}{5}} exp(-5.1 + 280\sqrt{d_p} - 3.6 \times 10^3 d_p) \qquad \textit{Equation 17}$$

Comprehensive reviews of the analytical and empirical models developed for sand saltation are available (Kok *et al.*, 2012). The development of sand transport models continues to be improved and more recent research methods have been applied recently, like statistical approaches analysing large amount of experimental data for different sand and fluid conditions to improve and compare models' applicability (Raffaele *et al.*, 2016) It is important to note that sand transport modelling studies often only include particle diameters up to 1 mm, as this is often the largest equivalent diameter for sand particles. There is a need in wildfire firebrand exposure research to extend this research to larger particle diameters, as well as couple the effect of firebrand combustion.

3.3 Particulate Transport in Wind: Computational Models

This thesis includes computational numerical simulations of simplified firebrand exposure scenarios, in Chapters 4, 5, and 6, using the FDS (version 6.7.7). FDS is a Large Eddy Simulation (LES) Computational Fluid Dynamics (CFD) most applicable to low Mach flows. The presented firebrand exposure investigations serve the objective of quantifying the error of, and analysing the influence of wind profile and different obstacles on firebrand deposition, creep and accumulation simulated in FDS. From the previous section's overview on the physical mechanisms of solid particle transport and deposition in wind flow we know that sufficiently accurate air flow dynamics at high Reynolds numbers including the interaction with solid obstacles, simulations are necessary to simulate these processes. The following section provides a brief overview of the available computational models and the FDS model governing equations and characteristics.

3.3.1 Wind Flow

CFD models can produce accurate wind flow profiles, and their interaction with obstacles by solving the conservation equations of mass and momentum for air with appropriate boundary conditions. Wind flow is usually assumed an incompressible viscous fluid with a single gas specie and its movement can be described by the Navier-Stokes equations given by Equations 18 and 19; where $\vec{u}$ is wind velocity, $\widehat{\rho_f}$ is the air density, p is pressure, and v_f the kinematic viscosity (Anderson, 1995).

$$\nabla \cdot \vec{u} = 0 \qquad \textit{Equation 18}$$

$$\frac{\partial \vec{u}}{\partial t} + \vec{u} \cdot \nabla \vec{u} = -\frac{1}{\widehat{\rho_f}} \nabla p + \nabla \cdot \left[v_f (\nabla \vec{u} + \nabla \vec{u}^T) \right] \qquad \textit{Equation 19}$$

Because directly resolving the Navier-Stokes equations for the complex flows present in wildfire application is unfeasible given the computational resources required, turbulent flow dynamics are estimated by either the Reynolds Average Navier Stokes equations (RANS), or Large Eddy Simulation (LES) approaches. FDS utilises LES, more detail and emphasis are therefore dedicated to LES approach in this section.

RANS is a statistical approach where each flow value is described with a mean value and a fluctuation component; where wind velocity is modelled as a composition of the time averaged speed and the fluctuating term representing everything not included in the time average ($\boldsymbol{u}(\boldsymbol{x},\boldsymbol{t}) = \overline{\boldsymbol{u}} + \boldsymbol{u}'$). This assumption is inserted in the Navier-Stokes equations allowing a simpler solution to the time averaged velocity component ($\overline{\boldsymbol{u}}$). Note a temporary change in vector notation in equation 20 due to the average notation impeding standard vector notation. The RANS equations are given by Equation 20 and Equation 21 (Piomelli, 2014).

$$\frac{\partial \overline{\boldsymbol{u}}}{\partial t} + \overline{\boldsymbol{u}} \cdot \nabla \overline{\boldsymbol{u}} = -\frac{1}{\widehat{\rho_f}} \nabla \bar{p} + \nabla \cdot \left[v_f \left(\nabla \overline{\boldsymbol{u}} + \nabla \overline{\boldsymbol{u}}^{\boldsymbol{T}} \right) \right] - \nabla \cdot R \qquad \textit{Equation 20}$$

$$R_{ij} = \overline{u_i' u_j'} \qquad \textit{Equation 21}$$

Because the RANS models are semi-empirical, defining various parameters is necessary to successfully run the model; these parameters are deducted from approximations created based on specific flow scenarios. LES, on the other hand, resolve the large eddys present in turbulent flow, and alongside Direct Numerical Simulations (DNS), solve most of turbulence scales and therefore theoretically describe turbulent flow in larger detail than RANS models do (Piomelli, 2014). The LES approach consists of applying a spatial filtering method; this method was developed from energetic considerations from Kolmogorov's theory of turbulence. In FDS, LES applies a filter of width Δ to the DNS equations where Δ depends on the computational domain grid cell volume (McGrattan *et al.*, 2021).The LES filtered momentum conservation equation in FDS is obtained by applying the box filter to the DNS equations; the resulting filtered equation is commonly known as the LES momentum equation.

The calculation of the produced sub-grid kinetic energy is especially important in LES; the term calculating this value allows energy transfer between the resolved turbulent scales of movement, which are large enough to be included and resolved in the specified computational domain grid sizes, and the smaller unresolved scales. The turbulence model which can be defined in LES refers to how the SGS flux terms are mathematically resolved. This thesis uses the FDS default turbulence model, the Deardorff model, defined by Equation 22 and Equation 23.

$$\mu_t = \rho C_v \Delta \sqrt{k_{sgs}} \qquad \textit{Equation 22}$$

$$k_{sgs} = \frac{1}{2}((\bar{u} - \hat{u})^2 + (\bar{v} - \hat{v})^2 + (\bar{w} - \hat{w})^2) \quad \textit{Equation 23}$$

In terms of the simulations conducted and presented in this thesis, the most relevant flow velocity and profiles are those simulated near solid surface ground, the FDS boundary conditions computations are therefore of particular interest. The normal velocity component in FDS at any boundary (solid, mesh, or open) is defined indirectly through the pressure boundary condition. Near wall flow dynamics include the challenge of resolving the viscous stress (τ_w) when the SGS stress term at the wall boundary is essentially non-existent. Important properties at the wall boundaries include the friction velocity (u_*), defined by Equation 24, which is used to nondimensionalise the streamwise flow velocity, (u^+) given by Equation 25. The non-dimensional wall normal distance (y^+) is calculated with Equation 26, using the viscous length scale (δ_v) given by Equation 27 (McGrattan *et al.*, 2021).

$$u_* = \sqrt{\frac{\tau_w}{\rho}} \quad \textit{Equation 24}$$

$$u^+ = u/u^* \quad \textit{Equation 25}$$

$$y^+ = y/\delta_v \quad \textit{Equation 26}$$

$$\delta_v = v/u_* \quad \textit{Equation 27}$$

Finally, FDS approximates the law of the wall, with the logarithmic profile given by Equation 28, where κ is the von Kármán constant with value of 0.41 and B is a constant with value 5.2 (McGrattan *et al.*, 2021).

$$u^+ = y^+ \qquad \text{for } y^+ < 11.81$$

$$u^+ = 1/\kappa \ ln(y^+) \ + \ B \qquad \text{for } y^+ \geq 11.81 \quad \textit{Equation 28}$$

3.3.2 Solid Particles

Similarly to wind flow simulations, there are different approaches to simulate solid particles in fluid flow, characterised by either a compromise in realistic representation of the flow, or necessary computational resources. On the more realistic side of the numerical approaches, there is the possibility of describing the fluid flow as two-phase, considering the particulate solid phase, by introducing the phases volume ratios directly in the Navier Stokes equation. The volume ratios of air (ϕ_f) and of the dispersed solid phase (ϕ_s), referring to the solid particles dispersed in the fluid medium, can be calculated by Equation 29 (Tilton, 1984).

$$\phi = V_i/V_j \quad \textit{Equation 29}$$

There are three main classifications that can be used to classify how different models characterise solid particles in fluid flow. Firstly, particles can either be described by the Lagrangian or Eulerian modelling approach. Lagrangian particle models consider individual particles, and compute each individual particle trajectory, Eulerian particle models treat a group of particles as a

continuum in the fluid and the bulk movement is calculated by resolving the conservation equations, as the fluids are modelled and described in CFD calculation (Giudice *et al.*, 2019).

Secondly, there are different types of equations that different types of models solve to output the particle position and velocity. The simplest type of model doesn't solve any physical equations relating to the particle movement and interactions, rather it utilises empirical relations to compute different particle fluxes. Alternately, mass and momentum conservation equations are solved for the fluid phase, while only mass conservation is solved for the solid particles; this assumes that the solid particles are passively carried by the fluid; this is an acceptable assumption for flows with low concentration of particle. Additional terms and forces can be included as is significant for the specific considered scenario to take into account variations in the particle velocities and positions (Giudice *et al.*, 2019). This is the most common modelling approach, and how FDS models solid particle movement in fluid flow. The most complex computational simulation approach solves mass and momentum conservation equations for both phases of the flow and interaction forces acting between the phases.

Lastly, models can differ in the amount of coupling consideration between particles and the fluid flow. 1-way coupling refers to the particles being passively carried by the wind flow without any feedback between particles and flow field. 2-way coupling considers the solid particles when computing the fluid flow, and 4-way coupling inter-particle interactions are considered in the model as well as interactions between the particles and wind flow.

FDS is an open source software commonly used in fire safety modelling. FDS includes a Lagrangian particle model which is used to model firebrand particles in the presented research (McGrattan *et al.*, 2021). Lagrangian particles are used in FDS for a variety of purposes including modelling water droplets to model sprinkler mitigation of fire, and modelling vegetation by creating stationary particles with appropriate characteristics intermixed with void space, for example leaves and smaller vegetation elements.

Lagrangian particles are modelled through the force term ($\overrightarrow{f_b}$) which is included in the gas phase conservation of momentum equation. This term is calculated by Equation 30 and computed the force transferred from the particles to the surrounding fluid flow in a computational grid cell.

$$\overrightarrow{f_b} = \frac{1}{V}\sum[\frac{1}{2}\rho C_d A_p(\overrightarrow{u_p} - \vec{u})|\overrightarrow{u_p} - \vec{u}| - \frac{dm_p}{dt}(\overrightarrow{u_p} - \vec{u})] \qquad \textit{Equation 30}$$

The force term is related through Newton's second law of motion (Equation 31) to the particle acceleration. Each particle acceleration, velocity and position are then resolved using Equation 32; where C_d is the drag coefficient, A_p is the particle cross-sectional area, r_p is the particle radius, ρ is the gas density, $\vec{u}$ is the gas velocity , $\overrightarrow{u_p}$ is the particle velocity, and m_p is the particle mass.

$$\overrightarrow{f_b} = m_p\overrightarrow{a_p} \qquad \text{Equation 31}$$

$$\overrightarrow{a_p} = \frac{d\overrightarrow{u_p}}{dt} = \vec{g} - \frac{1}{2m_p}\rho C_d A_p(\overrightarrow{u_p} - \vec{u})|\overrightarrow{u_p} - \vec{u}| \qquad \textit{Equation 32}$$

FDS contains drag coefficient equations for spherical and cylindrical particles given by Equation 33 and Equation 34 respectively for different Reynold's number (Re) ranges.

$$C_{d,spherical} = \begin{cases} \frac{24}{Re} & Re < 1 \\ \frac{24(0.85+0.15Re^{0.687})}{Re} & 1 < Re < 1000 \\ 0.44 & Re > 1000 \end{cases} \qquad \textit{Equation 33}$$

$$C_{d,cylindrical} = \begin{cases} \frac{10}{Re^{0.8}} & Re < 1 \\ \frac{10(0.6+0.4Re^{0.8})}{Re} & 1 < Re < 1000 \\ 1 & Re > 1000 \end{cases} \qquad \textit{Equation 34}$$

In a published validation of FDS simulation for short-range firebrand transport, the default FDS drag model for spherical particles (Equation 33) is used due to the high particle sphericity, ψ=0.8, of the cuboid particles used in experiments (Wadhwani *et al.*, 2017). Wadhwani, in their PhD thesis investigating firebrand short-range transport, reviewed and selected the four most applicable drag coefficient models for generic shaped particles based on empirical data and sphericity particle measurements in literature, and modified the FDS code to test their accuracy (Wadhwani, 2019). Results concluded that the drag model developed by Haider and Levenspiel (Haider and Levenspiel, 1989), performed reliably accurately in the FDS simulations for all the particle shapes and Reynolds numbers tested.

3.3.3 FDS Applicability

The FDS is a software specifically developed and regularly applied to simulate fire scenarios and their impact on various materials and situations (McGrattan and Miles, 2016). The fire engineering focused context of the software development, revision, and its primary purpose significantly influenced the justification of applying it the presented research. As firebrands pose a significant and growing hazard to worldwide infrastructure, there is a need in fire safety engineering to advance understanding of the simulation accuracy and applicability of FDS simulation of firebrand exposure; this is reflected in recent literature applying FDS to various aspects of firebrand exposure (Wadhwani *et al.*, 2017; Mankame and Shotorban, 2021; Wickramasinghe *et al.*, 2022). Furthermore, the vast research and practice of simulating fire scenarios with FDS can easily aid a future advancement of connecting the firebrand deposition simulations and knowledge to probable spot fire propagation and impact.

FDS is used to simulate the published wind-tunnel experimental investigations of firebrand deposition and accumulation in front of vertical wall obstacles (Suzuki and Manzello, 2017) in chapter 4, to simulate firebrand deposition around wall, re-entrant corners, and steps solid obstacles in chapter 5, and finally to simulate the application of a trench protection measure in a simple exploratory domain, and in front of a re-entrant corner obstacle in chapter 6. Two different FDS modalities within the Lagrangian particle model, regarding particle deposition on solid surfaces

considering infinite kinetic friction, and non-existent kinetic friction of the solid surfaces are applied and compared in both chapters.

FDS is a CFD software applicable for low-Mach number Newtonian fluids conditions, modelling turbulence through Large-Eddy Simulation (LES). The most significant FDS numerical models for this study are the Lagrangian particle and solid boundary layer in turbulent flow. The Lagrangian particle model neglects particle-particle interactions, and individually calculates momentum transfer between each particle and the carrier fluid (two-way coupling); literature has concluded this is a reasonable assumption for firebrand wind-driven transport given the assumed spacing length between particles (Wadhwani *et al.*, 2017).

Two FDS modalities are used and presented due to their different approach and result in calculating particle interaction with solid boundaries. One modality codes the Lagrangian particles to remain stationary when the particles make contact with the solid boundary. This mode essentially simulates particle-ground interactions as having infinite friction. The alternative mode, and version 6.7.7 default mode for the Lagrangian particle, simulates the particle-ground interactions as essentially exhibiting zero friction. FDS in this modality continues solving the Lagrangian transport equations for the u and v velocity components (x and y, horizontal plane, directions); the particles will therefore keep contact with the solid boundary and move based on the local flow conditions.

The primary limitation of FDS in simulating particle landing subprocesses, creep movement, and accumulation, is that the physical interactions between the particles and solid boundary are not calculated, but rather approximated through mathematical limits and rules. One of the main objectives of this thesis research is to quantify and characterise this limitation through comparison with experimental results, and application of firebrand exposure simulation to relevant WUI obstacles; providing results and methodologies that can serve in effectively applying the FDS Lagrangian model to retrieve useful information on firebrand exposure. The friction of the boundary does not influence the speed or interaction with the Lagrangian particles. Another limitation is te availability of only spherical and cylindrical drag models; this limits the possible testing of the diversity of particle shapes which may impact creep and accumulation. As expanded on in chapter 3, we introduce particles with a distribution of different diameters; thus, results capture the effect of diverse spherical particle sizes and weighs which can hopefully in future be related to realistic firebrand particle shapes. A section dedicated to informed suggestion to progression of research in simulating firebrand accumulation around solid obstacles is provided in Chapter 7, the conclusion.

Chapter 4 : Firebrand Deposition - computational model characterisation

4.1. Introduction

This chapter presents numerical simulations using FDS of the accumulation processes of firebrand particles in front of vertical walls, recreating published experimental wind tunnel set up for comparison and validation. Chapter 2 explored the literature of firebrand exposure processes and justified the research need to better understand firebrand deposition subprocesses, including creep movement and accumulation, to characterise firebrand exposure in the WUI and design safer buildings. Firebrand ignition has been attributed to up to 90% of WUI building ignition (Potter and Leonard, 2010); therefore, after quantifying building vulnerability as proposed in Chapter 3, firebrand exposure needs to be better understood and mitigated to meaningfully reduce wildfire damage.

Suzuki and Manzello investigated the firebrand accumulation patterns created windward of a simple wall obstacle, perpendicular to wind flow direction; smouldering firebrands were introduced via the NIST Dragon firebrand generator experimental apparatus, with inlet direction perpendicular to the wall obstacle (Suzuki and Manzello, 2017). The FDS computational domain created mimics the wind flow direction and pattern of the wind tunnel used in the experimental investigations; the measurements describing the firebrand accumulation patters are recorded and compared. In the process of simulating experimental conditions, relevant FDS modalities available and the particle characteristics assumptions are tested and commented on. The aim of this chapter is to quantitatively characterise the FDS error and applicability to model firebrand accumulation by comparing simulation and experimental results. Since the completion of this research chapter, a similar experimental wind tunnel experiment by the same author has been published conducted in the same wind tunnel with nearly the same experimental set-up, this time testing two different firebrand materials (Suzuki and Manzello, 2022).

4.2 Methodology

Figure 4-1 includes a photo of the Suzuki and Manzello wind tunnel experimental set up (Suzuki and Manzello, 2017) and a schematic of the final FDS computational domain plane at y=0. Figure 4-1 computational domain schematic indicates the relevant domain dimensions and features: the particle inlet vent located at coordinate ranges y= [-0.4, 0.4] and z= [1.6, 1.8], x=0; the wall obstacle is located at x = 7.5 corresponding to the 7.5m distance between the NIST dragon and wall obstacles in the experimental set up, the general location of accumulated firebrand particles windward on the wall obstacle, and the separation distance, which is the distance between the wall obstacle and the closest perimeter edge of the firebrand accumulated pile measured in the experiments. The wind tunnel

dimensions are 5 m width, 14m height, 15 m length leeward of the NIST dragon, and a 5 m length wind development zone windward the NIST dragon apparatus of 4 m height. The same dimensions are recreated in the computation domain as the experimental wind tunnel.

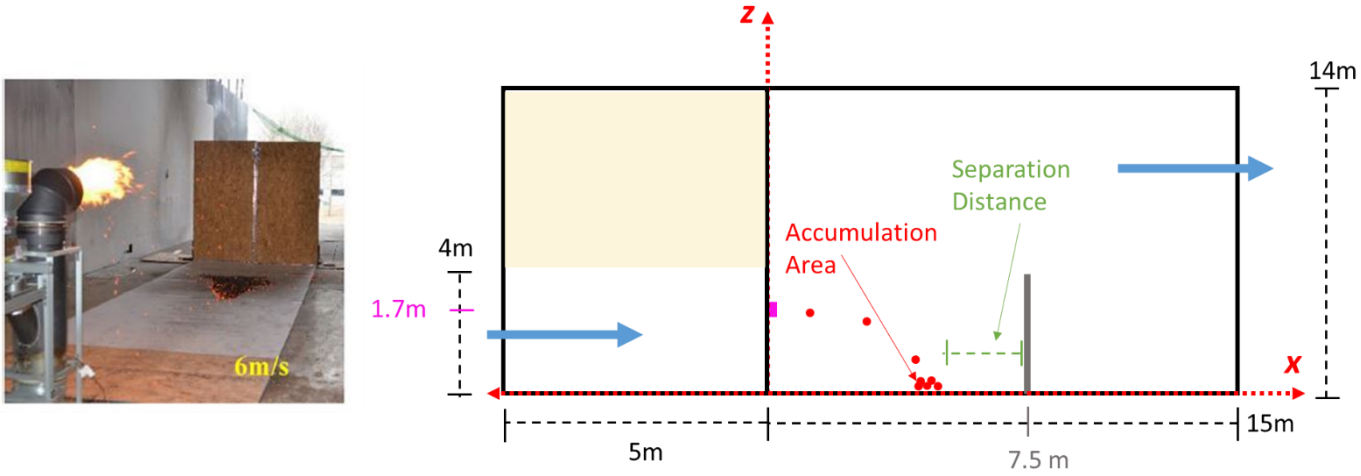

Figure 4-1: Photos of experimental set up from (Suzuki and Manzello, 2017) (left) and schematic of computational domain at y=0 cross section with labelled obstacle, particle inlet, and experimental measurements: accumulated area and separation distance (right).

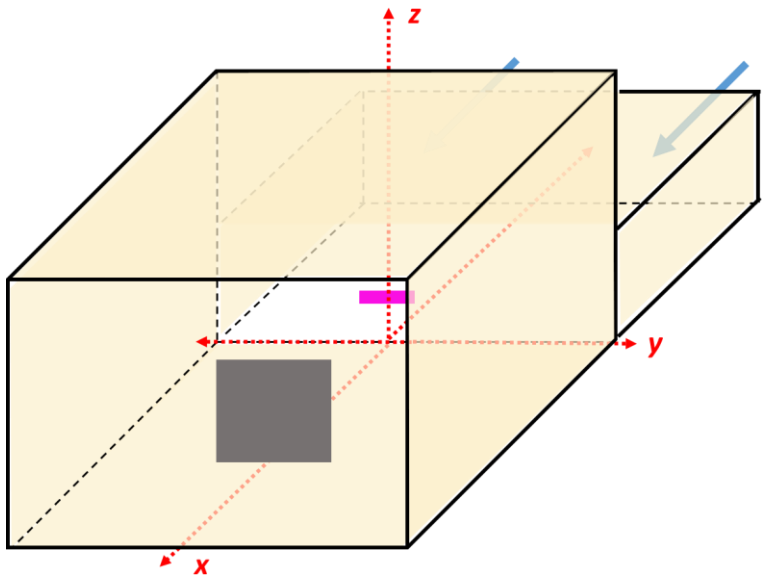

Figure 4-2: 3D schematic of wind tunnel FDS computational domain with main features illustrated: yellow surfaces are inert nonslip solid boundaries, blue arrows indicate wind flow inlet, pink rectangle is firebrand inlet vent and grey square represents the vertical wall obstacle.

Wind tunnel dimensions are recreated in computational domain due the significant effect on wind flow profile which was tested in a preliminary sensitivity analysis. The analysis conducted of running a number of domain dimensions (domain height for section of the domain varied between 5 – 15 m) to test the impact on simulated wind flow profile. Decreasing computational domain size can save computational power and resources; this analysis investigated how sensitive the wind tunnel flow is to domain volume. The average wind speed in the firebrand accumulation region was recorded and used to compare different computational domain configurations. This method was used to define the final computational domain dimensions and to determine the time wind flow developed and reached a quasi-steady state rate , after which firebrand particles are introduced in the simulation.

Figure 4-3 shows the average wind speed in the x-direction (u component) of the wind flow plotted for the first 60 seconds of simulation time for two computational domain heights (15 m and 10 m). Only the wind in the windward region of the wall obstacle, close to ground boundary (z: 0 - 0.1m) is considered to concentrate on the most relevant computational domain region for the particle deposition and accumulation. Wind speeds of 4 m/s and 6 m/s were both tested and showing larger discrepancies in the average wind speed for the 6 m/s wind tunnel speed. Computational domain heights of 5, 10, 12, and 15m were tested (experimental wind tunnel actual dimension was 14m height); we present two heights showing the different in wind speed experienced as this comparison alone shows the significant impact of computational domain height on the average wind speed in the region of interest.

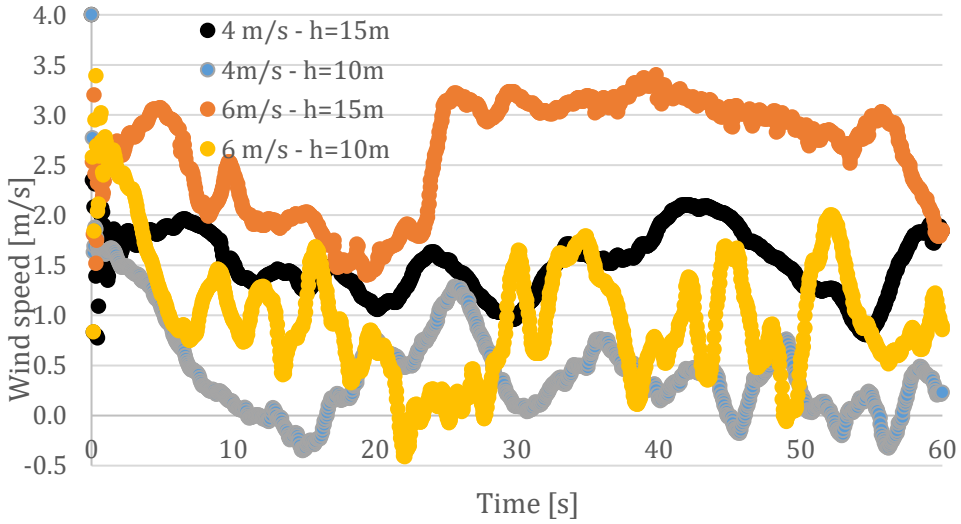

Figure 4-3: average wind speed (u) within selected computational domain region over time for two different computation domain heights: 10m and 15m.

The change between 12m and 15m computational domain heights, a relatively small 3m difference in computational domain height, resulted in the average wind speed in the firebrand accumulation region to difference between results with a maximum of 33%. This is considered a significant enough difference in local flow field to keep the original experimental wind tunnel

dimensions of 15m in our simulations to simulate the wind flow as accurately as possible. By comparing various regions within the computational domain following the same method, quasi-steady state developed flow is found to be reached after 5 s simulation time. These conclusions were also complemented by qualitative observations of flow visualisation.

To further quantify the flow field of the computational domain, wind flow streamlines of the u-component velocities at 60 s simulation time were examined to qualitatively compare and further understand the flow characteristics in the firebrand accumulation region. Figure 4-4 shows the streamlines generated with Paraview in the firebrand accumulation region grid location in context of the full computational domain from different angles, for wind tunnel speed of 4 m/s. The grey spherical shape is the point cloud used to define which streamlines are generated; the computed streamlines are those included in the point cloud volume.

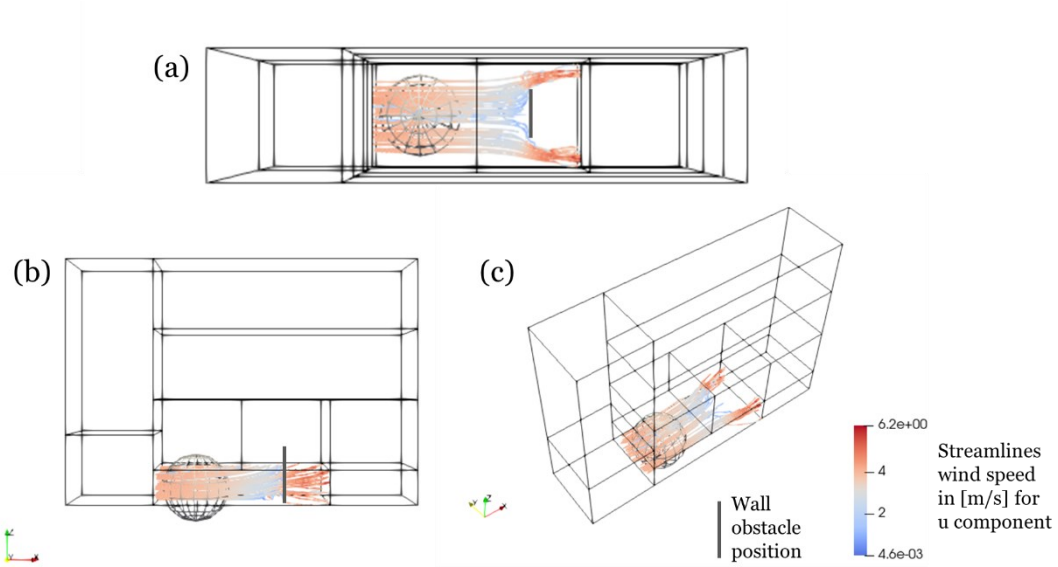

Figure 4-4: Full computational domain of FDS simulations including mesh grid boundaries outlines shown from (a) bird's eye view, top xy plane, (b) side view, xz plane, and (c) angled view. Streamlines are shown for firebrand accumulation mesh for 4 m/s wind tunnel speed.

Figure 4-5 focuses on the firebrand accumulation region mesh streamlines for all wind speeds tested. The point cloud sphere used for these streamlines has a radius of 1 m and is centred at (7,0,0) coordinate, which corresponds to 0.5m windward of the wall obstacle on the ground surface. This location is selected to observe the local flow field patterns in the firebrand accumulation region. Figure 4-5 qualitatively illustrates the changes in the wind flow as the wind tunnel inlet speed increases. Upon wind contact with the vertical wall, recirculation zones windward and parallel to the obstacle are formed. The wind speed slows down as the recirculation zones are formed. The recirculation zones continue around the sides of the wall obstacle. The turbulence of the recirculation zones on both sides of the wall obstacle visibly increase as the inlet wind speed increases.

Side view: xz-plane from y = -2.5m

Bottom view: xy plane from z = 0m

Wind tunnel speed: 4 m/s

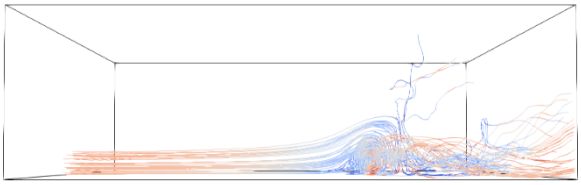

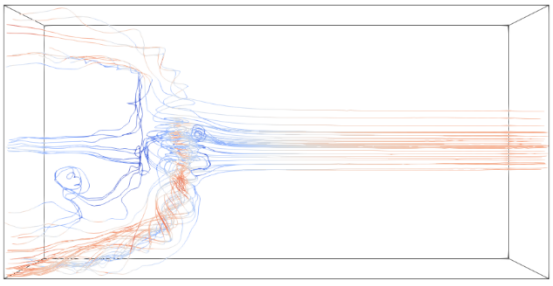

Wind tunnel speed: 6 m/s

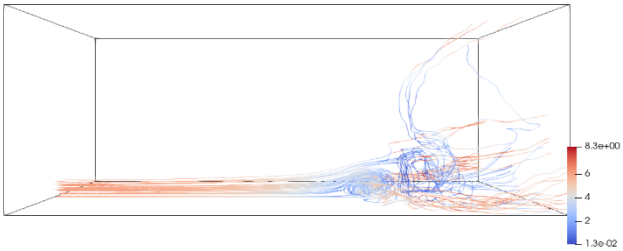

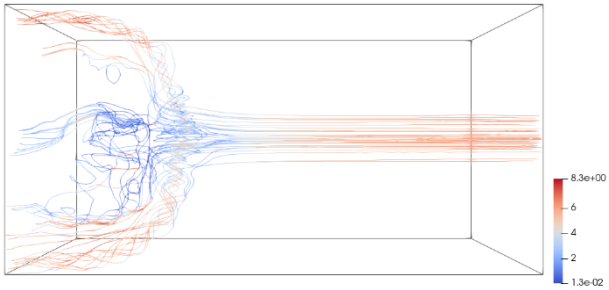

Wind tunnel speed: 8 m/s

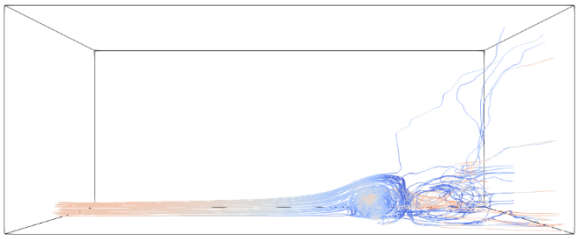

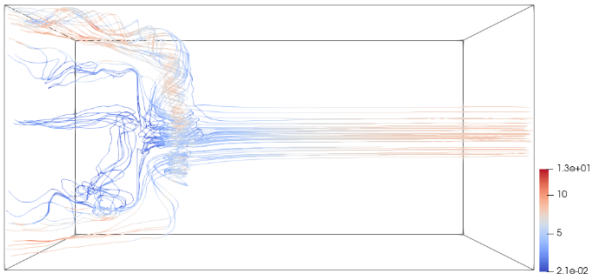

Wind tunnel speed: 10 m/s

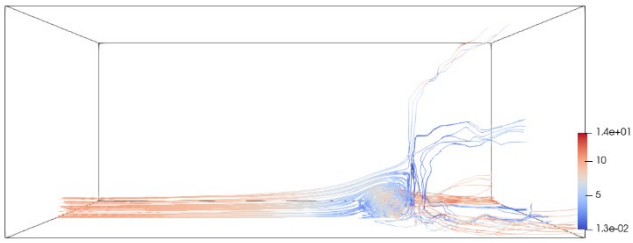

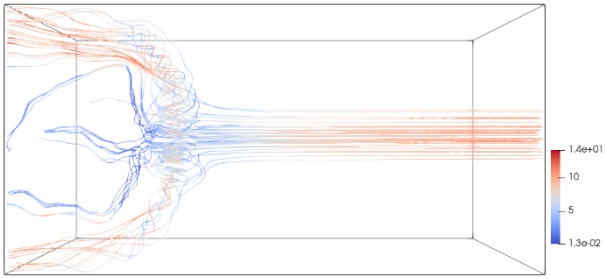

Figure 4-5: Streamlines in firebrand accumulation region mesh grid at 60s of simulations for wind speeds 4 – 10 m/s in two different orientations per each wind speed simulated.

Mesh grid sensitivity analysis resulted in average 7% error of final particle position with chosen grid sizes: 125cm^3 grid cells (δ = 5cm) in particle accumulation area (x: [0-15], z: [0-6]), and 1000cm^3 grid cells (δ = 10cm) in remaining computational domain. Domain is divided in 9 meshes, each assigned to a separate MPI processors and solved on high performance computer systems. To quantify the model sensitivity to various input parameters, the one-at-a-time (OAT) sensitivity analysis is conducted using Equation 35. The results of the sensitivity analysis are presented independently in Figure 4-6 and also in terms of the Tachikawa (K) nondimensional number in Figure 4-7. K is calculated with Equation 36, which describes the aerodynamic properties of flying objects or debris; it quantifies the ratio of aerodynamic to gravitational forces for an object.

$$S_i = \left| \frac{Y(X_{io}+\Delta X_i)-Y(X_{io})}{\Delta X_i} \times \frac{X_{io}}{Y(X_{io})} \right| \qquad \textit{Equation 35}$$

$$K = \frac{\rho_f u_0^2}{\rho_p g d_p} \qquad \textit{Equation 36}$$

Where Si is the sensitivity coefficient, X_{io} is initial input value, Y_{io} is associated output value, and ΔX_i is the incremental increase in input applied. Table 4-1 presents all the calculated K for the tested particle and wind flow parameters combinations, sensitivity coefficients and respective K values are plotted in Figure 4-7. The initial input values used in the sensitivity are given in the first line of Figure 4-1. The bars in Figure 4-6 are colour-coded corresponding to which property, particle density, diameter, geometry, or wind speed, inlet height, inlet flow was tested in the sensitivity analysis.

Table 4-1: Properties tested in sensitivity analysis, particle diameters, particle densities, inlet wind tunnel speed, and the corresponding calculated Tachikawa dimensionless number(K).

K	d_p [mm]	ρ_p [kg/m^3]	u_0[m/s]
7.5	4.0	71	4.0
40	4.0	13	4.0
16	4.0	33	4.0
3.7	4.0	142	4.0
23.0	1.3	71	4.0
11	2.6	71	4.0
7.5	8.0	71	4.0
0.47	4.0	71	1.0
17	4.0	71	6.0

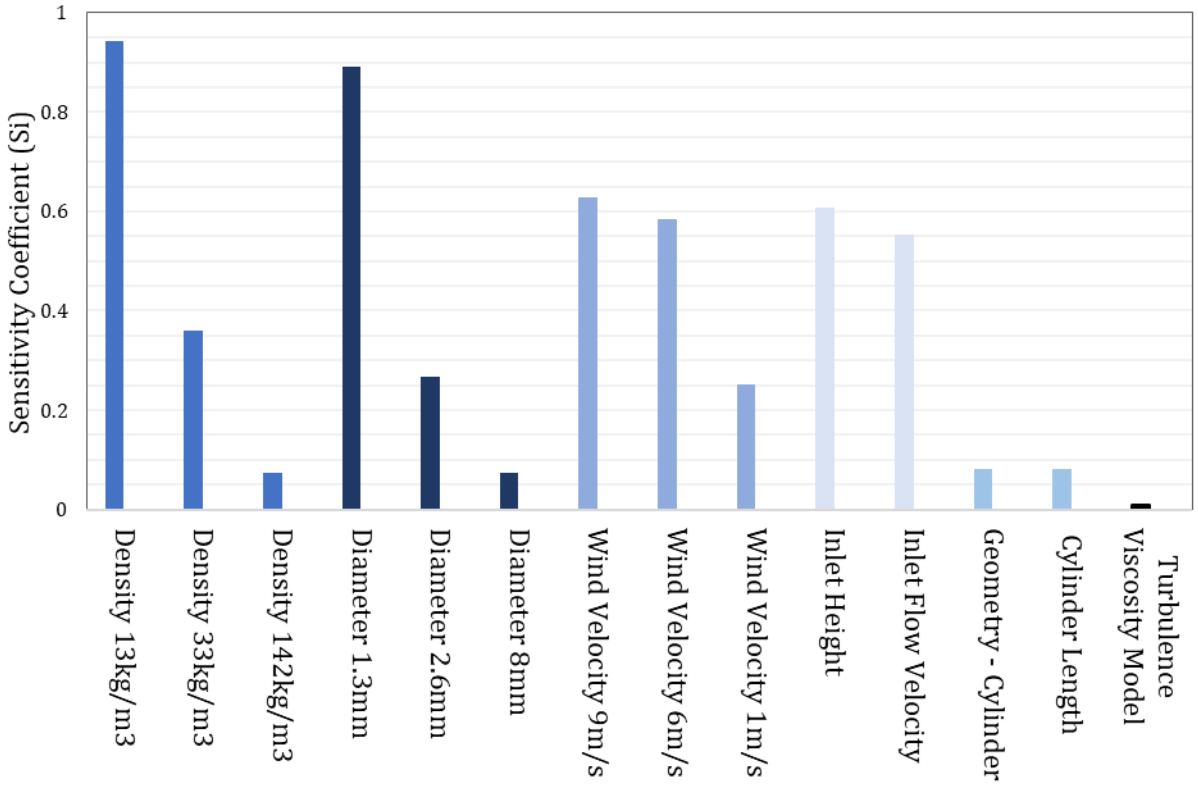

Figure 4-6: Bar graph of sensitivity coefficients for all input parameters tested in OAT sensitivity analysis for particles final position output, colour-coded based on types of property tested in the sensitivity analysis.

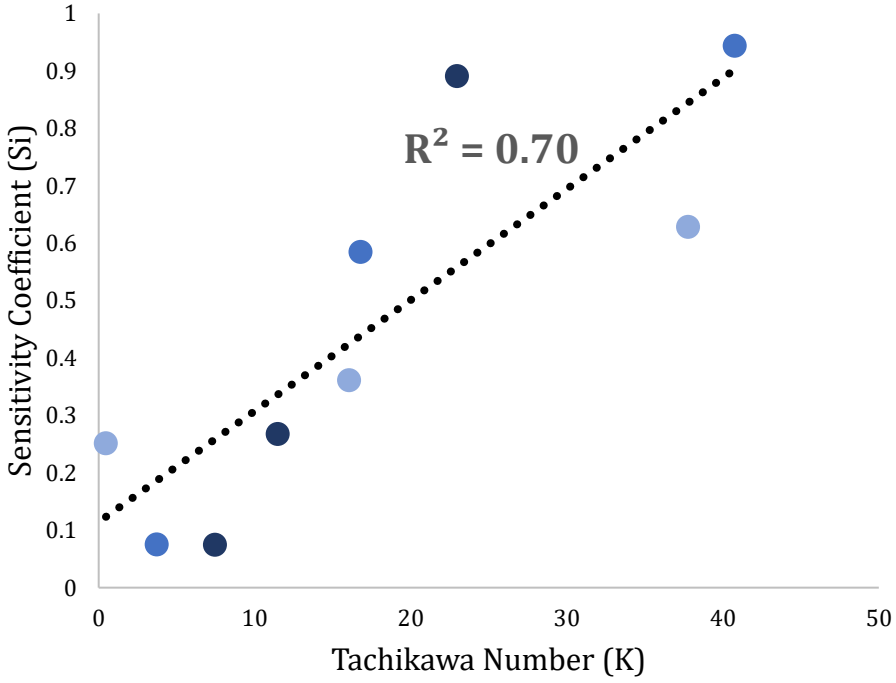

Figure 4-7: Sensitivity Coefficient plotted against the particle Tachikawa Number, colour-coded based on types of property tested in the sensitivity analysis.

The sensitivity analysis shows the Lagrangian particles final position is most sensitive to particle density (ρ_p) for lighter particles, particle radius (r_p) for smaller particles, high wind speeds, inlet height and flow velocity. The significant sensitivity variation relative to the magnitude of particle density, particle diameter, and wind speed indicates there are relative interdependent threshold values which, if reached, significantly impact the particle accumulation position. The relationship expressed in Equation 37 between particle acceleration and particle density and diameter is isolated from the FDS Lagrangian Particle mathematical model. Equation 37, coupled with the particle properties of firebrands used in the experiment, can inform the particle properties chosen in FDS.

$$a_p \propto \begin{cases} \rho_p^{-1} r_p^{-2} & Re < 1 \\ \rho_p^{-1} r_p^{-2} + \rho_p^{-1} r_p^{-1.313} & 1 < Re < 1000 \\ \rho_p^{-1} r_p^{-1} & Re > 1000 \end{cases} \qquad \textit{Equation 37}$$

This chapter presents simulations conducted with two different particle distributions: test A introduced four different particle types ranging from the smallest and lightest of 3.6 mm radius and 50 kg/m^3 density, to the largest heaviest of 3.9 mm radius and 400 kg/m^3. Test B introduces particles all with 50 kg/m^3 density and normally distributed particle radii over the 2.5mm - 7.5 mm range.

Particle density is selected based on the density of Douglas-fir wood (500 kg/ m^3), which is used in experiments to generate firebrands. Literature suggests to estimate char density as 10% of unburnt wood density (Ragland *et al.*, 1991). Test A aims to simulate a ranges of particle size and density mimicking wood densities at various stages of combustion from unburnt wood to completely charred wood; this is to address the limitation of simulation firebrands as non-burning, constant volume Lagrangian particles. The particle radii and density are also chosen to match the final firebrand weight range distribution reported in the experiment (0.01 g – 0.1 g) (Suzuki and Manzello, 2017).

Table 4-2 summarises the firebrand particles properties in the experimental investigation, and in the two FDS tests presented. In the experiment Douglas Fir wood cuboids (7.9 mm x 7.9 mm x 12.7 mm) are fed to the NIST Dragon which ignites and blows them with a 17.1 g/m^{2}s mass flux. The Lagrangian particles are inserted through a vent, with 17.0 g/m^{2}s mass flux for 15s; this inlet time duration is chosen by dividing the experimental inlet mass flux by the NIST dragon inlet wood mass (8 kg) and multiply by its outlet area ~730.6 cm^2. Two wall obstacle heights are tested in the experiment (1.36m and 2.44m); in test A two similar wall heights are tested (1.3m and 2.4m). Because no significant difference in particle accumulation location was measured, only wall height 2.4m is tested in test B. All solid boundaries in simulations are set to no-slip boundary condition.

Table 4-2: Parameters from published experimental investigation (Suzuki and Manzello, 2017) and from FDS test A and B presented.

Parameters	**(Suzuki and Manzello, 2017) Experiment**	**Test A**	**Test B**
Particle Geometry	Initial: Cuboid	Sphere	Sphere
Particle Dimension	Initial: 7.9 × 7.9 × 12.7 mm	• r = 3.6 mm, ρ = 50 kg/m³ • r = 3.7 mm, ρ = 100 kg/m³ • r = 3.8 mm, ρ = 200 kg/m³ • r = 3.9 mm, ρ = 400 kg/m³	ρ = 50 kg/m³ Normal Distribution between: r_i = 2.5 mm r_f = 7.5 mm
Particle Density	Douglas Fir Wood (ρ = 530 kg/m³) Smouldering combustion		
Firebrand Inlet	NIST Dragon - cylindrical geometry.	Inlet vent – no Dragon structure	Inlet vent – no Dragon structure

4.3. Results

The position distributions of particles on the computational domain floor plane (z = 0), with varying wind speeds, wall obstacle heights, and particle characteristics are presented. Final simulation results are compared with measured experimental results: separation distance between particle accumulation and wall obstacle, and accumulated area size.

4.3.1 Lagrangian particle properties and wind speed impact

Figure 4-8 presents particles' position on the xy-plane at z=0 (computational domain floor) with wind tunnel wind speed of 0 m/s for models A and B. The graphs show the final particle distribution on the computational domain floor for the two different particle properties simulated. This simulation comparison objective was to investigate the influence of the different particle properties, without any induced wind, on final particle distribution. In test A particles of same size and density are colour-coded and introduced separately, allowing to visually assess the impact of varying particle density and size on final accumulation position. Test B introduced particles with varying radii with constant particle density of 50 kg/m³. Figure 4-8 confirms test A and B result in similar final particle position distribution ranges; both ranging between 0.6 m and 1.6 m from the particle inlet in the x direction.

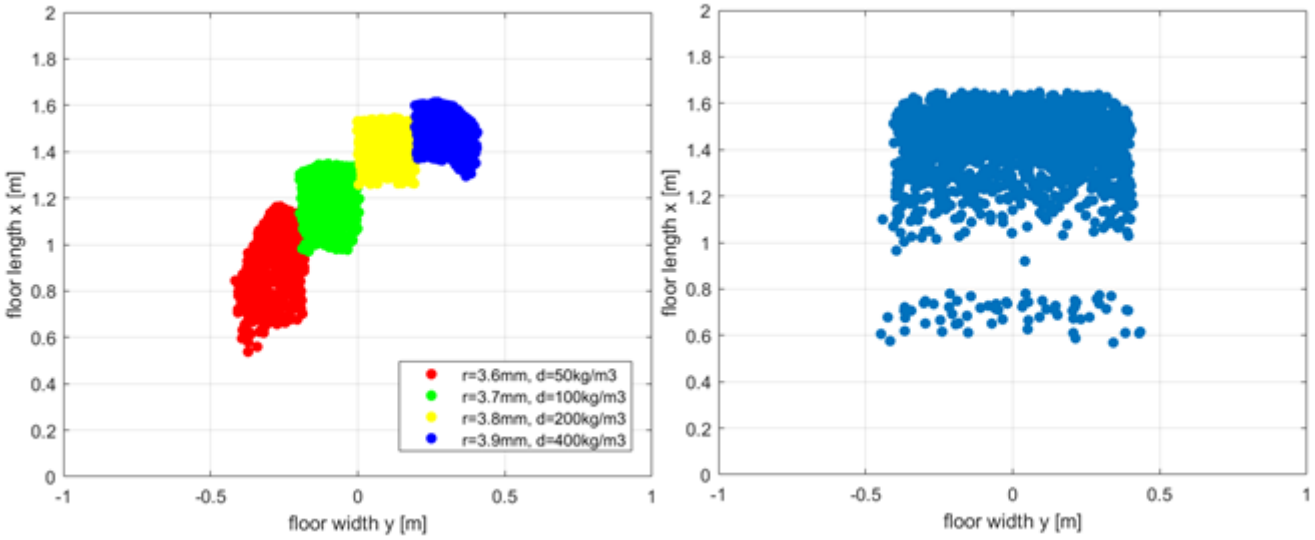

Figure 4-8: Position of particles on computational domain floor (z = 0) at 0 m/s wind for (left) test A, and (right) test B: particles have constant density with normally distributed radii.

Figure 4-9 presents boxplots of test A final particle positions on the computational x-axis (the wind flow direction) at t=15s for all wind speeds tested (0, 4, 6, 8, 10 m/s). The black line indicates the position of the wall obstacle at x=7.5. The lightest and smallest particles introduced (50 kg/m^3 density), never reach deposit at wind speeds ≥ 6 m/s; these particles move around and behind the wall obstacle without possibility of stationary accumulation. The two wall obstacle heights tested in the experimental investigation are also simulated although give no significant difference in particle accumulation location, as shown in Figure 4-10.

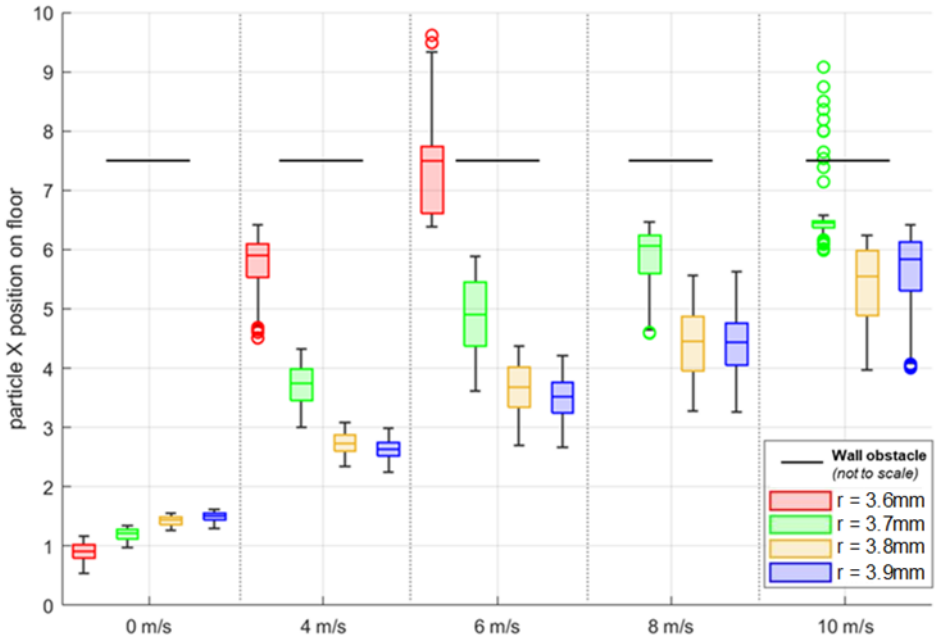

Figure 4-9: Boxplots of test A particle distribution on computational domain floor (z=0) at t=15s for all wind speeds tested. Black line indicates wall obstacle position at x=7.5 m

Figure 4-9 and Figure 4-10, which compares the simulation results with varying obstacle wall heights, show that two heaviest and largest particles tested (200 kg/m3 and 400 kg/m3 densities), have similar accumulation distribution; this supports the concept that above a size and weight particle threshold (relative to local flow field), particle parameters are less significant in determining landing and accumulation location.

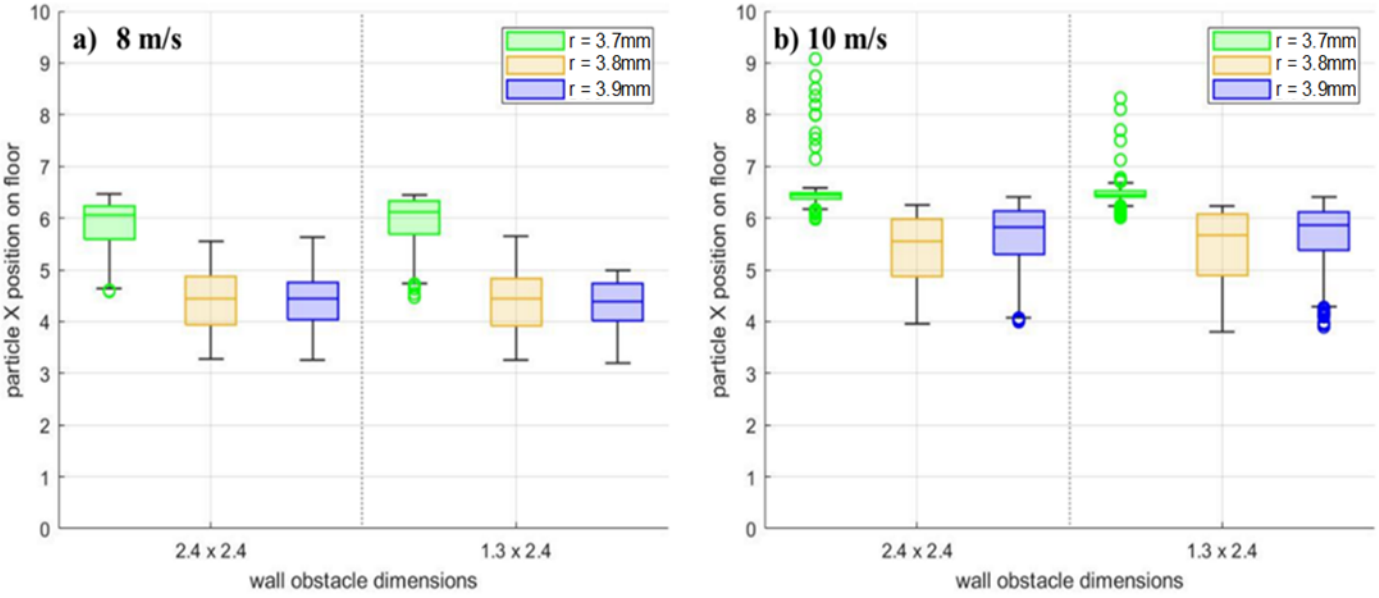

Figure 4-10: Boxplots of test A particle distribution on computational domain floor (z=0) at t=15s for 8m/s(a) and 10 m/s(b) wind speeds for two different wall heights tested: 1.3m and 2.4m

4.3.2 Investigation of creep

As introduced in Chapter 2, section 2.2.3, creep refers to the movement firebrands experience after deposition, or coming into contact with the ground solid obstacle, as particles roll or slide along the surface. Creep movement has been investigated in established sand movement literature and precedes accumulation (referring to when particles reach stationary position and therefore group together). Test B particle parameters are selected to explore FDS ability to simulate this phenomenon.

As briefly introduced in Chapter 3 section 3.3.3, two FDS modalities of FDS version 6.7.7 are tested. In one mode, which we will name 'infinite friction' mode, creep movement is not observed. The friction between particles and solid boundaries is essentially assumed as infinite, and no secondary particle movement is observed after particle come to contact with solid boundaries. The second mode tested, and FDS 6.7.7 default mode will be named 'zero friction' and simulates an extensive creep movement which we characterise for different wind speeds. Particle position on the floor is recorded after various time steps in both FDS modalities simulations. Figure 4-11 presents the particle distributions for different wind speeds (6 -10 m/s) after 10 to 300s in FDS 'infinite friction' mode. 4 m/s ambient wind speed simulations are not conducted with FDS 'infinite friction' mode, because

experimental results record no firebrand accumulation at 4 m/s wind tunnel speed and there are therefore no results to compare and validate. Figure 4-12 presents the particle distributions for different wind speeds (4 -10 m/s) after 10 to 120s in FDS 'zero friction' mode. The creep movement calculated by FDS 'zero friction' mode, and the absence of creep movement in FDS 'infinite friction' mode is quantified in Figure 4-13; where the arithmetic mean particles x-coordinate (distance from inlet in the wind direction) on the simulated wind tunnel floor (z=0 plane) is plotted against time after particle insertion. FDS 'infinite friction' mode mean x-coordinate values stay constant throughout simulation time, with higher wind speeds leading to particle accumulation closer to wall obstacle. FDS 'zero friction' mean particle x-coordinate position show convergence toward a steady state position; mean x-axis position steady state is reached and equal for 8 and 10 m/s wind, while 4 and 6 m/s wind do not reach steady state in the 150s simulated particle insertion time.

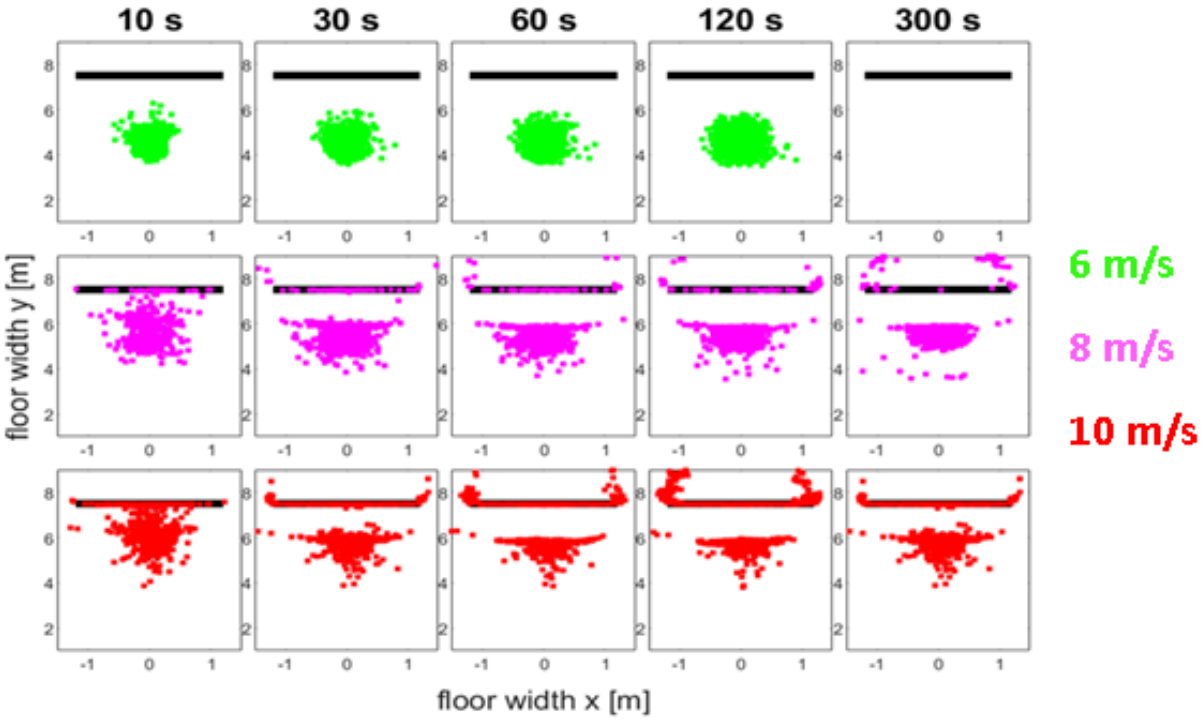

Figure 4-11: FDS 'infinite friction' mode computational domain floor plane (z=0) particle distribution for 6 - 10 m/s wind speeds at t=10 - 300s post particle insertion time

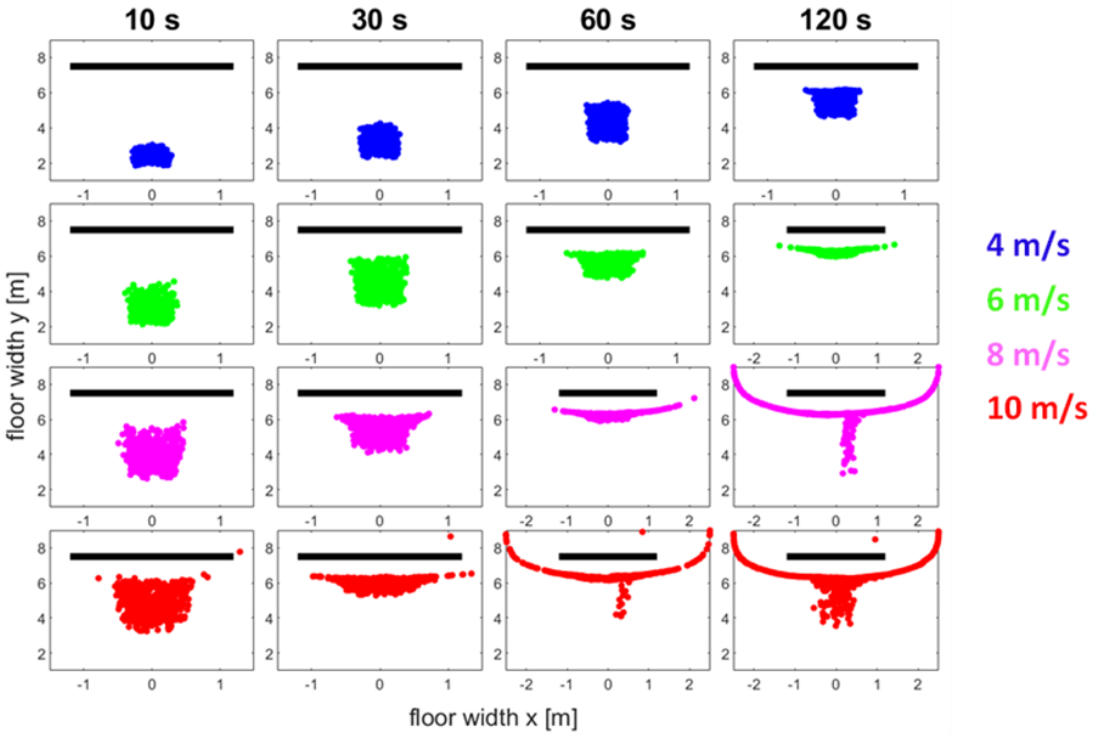

Figure 4-12: FDS 'zero friction' mode computational domain floor plane (z=0) particle distribution for 4 - 10 m/s wind speeds at t=10 - 120s particle insertion time.

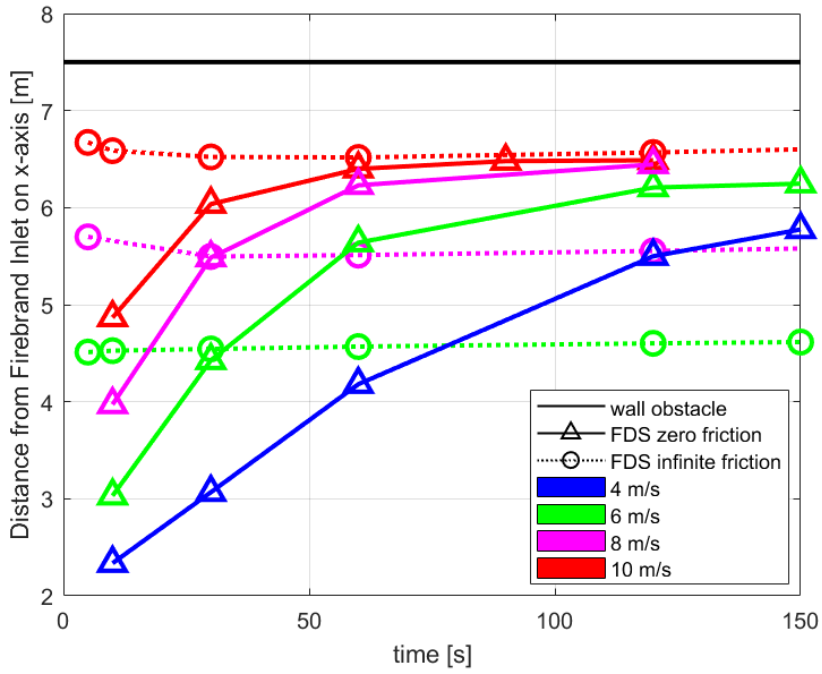

Figure 4-13: Line graph showing mean x-axis coordinate position of particles on computation domain floor plane (z=0) 10 - 150 seconds after particle insertion. Results from FDS 'zero friction' and 'infinite friction' mode for 4-10 m/s wind speeds.

4.3.3 Validation with experimental results

The simulated particle distributions are compared to experimental results reported in (Suzuki and Manzello, 2017). The experimental measurements reported are separation distance, referring to the distance between the particle accumulation area and wall obstacle, and the accumulation area size. Figure 4-14 and Figure 4-15 compare these measurements to simulated particle distributions, experimental measurements are marked as red squares and numerical distribution results are shown in black and grey. Firebrands in 4 m/s wind experiments did not accumulate and are therefore excluded from both figures due to limited experimental results for comparison. Although steady state is not reached for 4 m/s FDS 'zero friction' mode simulations, particles seem to accumulate in same manner as higher wind speeds in FDS simulations. The simulated particles distributions at t=120s for both FDS modalities are selected as final particle distributions, as this is longest simulation for FDS 'zero friction' mode and there is no change in distribution for FDS 'infinite friction' mode at t>120s.

Figure 4-14 and Figure 4-15 compare the FDS floor particle distribution windward of the wall obstacle as grey boxplots to the published separation distance measurements, converted to x-coordinate position by subtracting the separation distance from 7.5m. For 8 and 10 m/s only windward particles (x< 7m) are selected as this is relevant particle accumulation area.

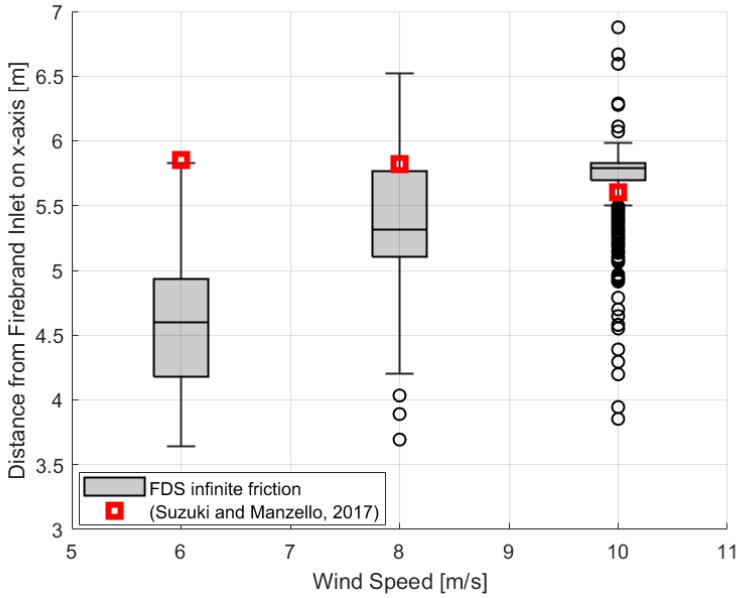

Figure 4-14: Boxplots showing FDS 'infinite friction' mode floor particle distribution windward of wall obstacle at t=60s and experimental measurements of separation distance between wall obstacle and accumulated firebrands from (Suzuki and Manzello, 2017).

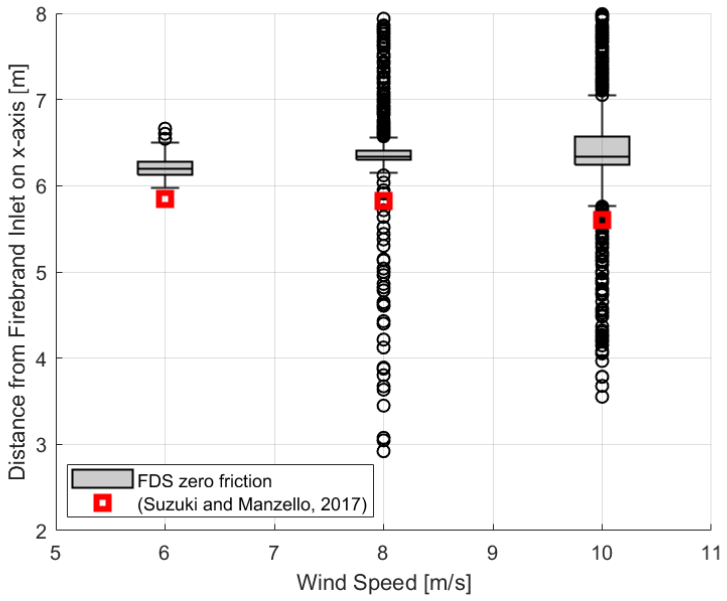

Figure 4-15: Boxplots showing FDS 'zero friction' mode floor particle distribution windward of wall obstacle at t=60s and experimental measurements of separation distance between wall obstacle and accumulated firebrands from (Suzuki and Manzello, 2017).

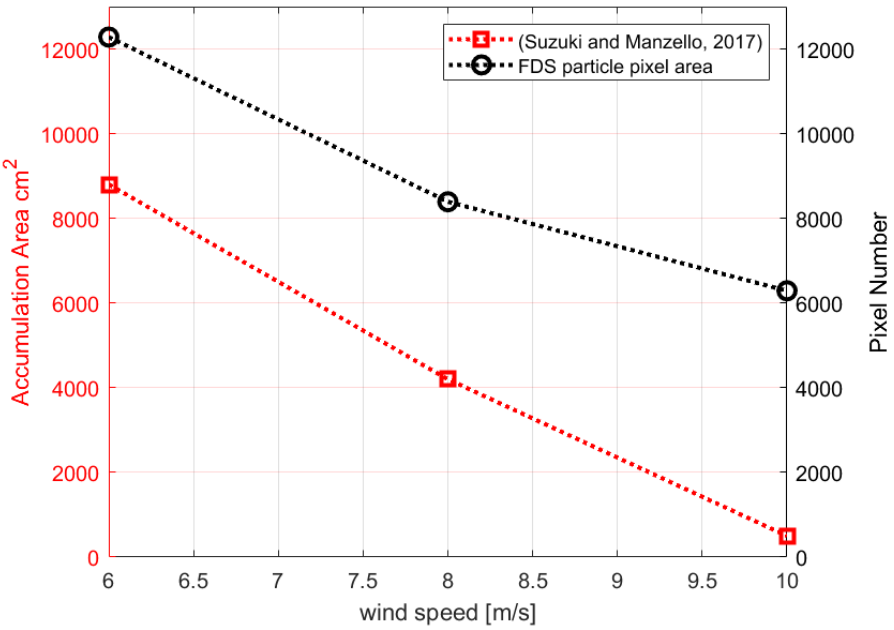

Figure 4-16: Accumulation Area approximated via number of pixels of accumulated particle distribution in FDS 'infinite friction' mode simulation compared to experimental measurements from (Suzuki and Manzello, 2017).

Figure 4-16 plots the pixel number area quantification alongside accumulation area measurements reported in (Suzuki and Manzello, 2017). The image analysis software QuPath is used to quantify the accumulated particle area windward of the wall obstacle in a standardised manner. Note experimental results follow the red left y-axis, and numerical simulation quantification the black right y-axis.

Particle accumulation areas location, or separation distances between particles and wall obstacle disagree with experimental measurements. Experiments recorded an increase in separation distance of 0.25m as wind speed increases from 6 to 10 m/s; this trend is not observed in either FDS modalities which result in comparable separation distances across wind speeds except for 6 m/s in FDS 'infinite friction' mode which results in a higher separation distance compared to 8 and 10 m/s. Although both FDS modalities simulate a separation distance caused by the local flow recirculation zone formed windward of the wall obstacle, this distance length and location does not match experimental results. Furthermore, experiments report no firebrand accumulation occurring at 4 m/s wind, FDS does not simulate any significant change in particle accumulation or creep movement at 4 m/s wind speed. FDS 'infinite friction' mode separation distances.

Differences between computational and experimental parameters can explain result disagreements; most significantly the flow boundary layer conditions which would define the recirculation zones size and location windward of wall obstacle. In presented FDS model, all solid boundaries are defined as no-slip surfaces without considering specific wind tunnel floor material roughness. Furthermore, FDS does not consider the friction between Lagrangian particles and ground floor, thus not fully simulating the creep movement dynamics. Lastly the Lagrangian particles are non-burning while experimental firebrands are experiencing combustion. Ambient wind speed would influence, not only the particle transport, but also the particle combustion dynamics. Future work will test these assumptions and their impact on the particle creep movement and accumulation to iteratively increase model complexity to accurately model movement dynamics.

4.4.4 Quantifying difference between FDS results and experimental measurements

To quantify the FDS results and experimental measurements difference, we compare the simulated separation distance between accumulate particles and wall obstacle, to the separation distance reported in (Suzuki and Manzello, 2017); this is presented in Table 4-3. The experimental separation distance results are published as single values measuring the distance between the observed accumulated firebrand piles and the wall. FDS simulations provide all firebrand particles coordinate locations over the simulation course; we present their distributions with statistical parameters. Different calculations are applied to select a value for each FDS particle coordinates samples which best represents the accumulated firebrand pile edge closest to the wall to calculate the separation distance.

Figure 4-11 and Figure 4-12 show the particles positional distribution resulting from the different FDS modalities and are used to assess which calculation is most applicable for each scenario tested to select the separation distances. For 'infinite friction' mode at 6 m/s the particles located closest to the wall are part of the accumulated firebrand pile; therefore the maximum value of all particle coordinates is selected, indicated with the top whisker of Figure 4-14 respective boxplot. At 8 and 10 m/s Figure 4-11 show there are particles that have reached and surpassed the wall edge location; therefore the 75th percentile coordinate out of all particle positions, indicated by the top edge of the grey box in Figure 4-14 boxplots, are selected.

Similarly, in the 'zero friction' mode simulations, Figure 4-12 shows particles extend beyond the accumulated particle pile at 8 and 10 m/s, with considerably higher number of particles surpassing the wall obstacle at 10 m/s. The maximum non-outlier value of the 6 m/s particle coordinate distribution (shown by the top whisker in the Figure 4-15 boxplot) is therefore selected, and the 75th percentile coordinates are selected out of the particle locations at 8 and 10 m/s.

A general trend is noticed: the difference between simulated values and experimentally measured values increases as wind speed increases in both FDS modalities tested (zero friction and infinite friction) and for both measurements compared to experimental results (separation distance and change in accumulated area). This can be explained by the increasing turbulence and therefore increasing complexity of fluid dynamic interactions which occur in the computational domain which limit the simulation capabilities of local flow conditions which determine the correct firebrand accumulation area position.

Table 4-3: Difference calculation of accumulation location measurements in meters from firebrand inlet between experimental observations (Suzuki and Manzello, 2017) and FDS 'infinite friction' mode and 'zero friction' mode results

	6 m/s	**8 m/s**	**10 m/s**
Suzuki & Manzello, 2017	5.85m	5.82m	5.6m
FDS 'infinite friction'	5.8m	5.75m	5.8m
Difference *[%]*	0.86%	1.22%	-3.45%
FDS 'zero friction'	6.5m	6.4m	6.6m
Difference *[%]*	0.82%	-9.06%	-13.85%

An important characteristic of the difference computed by the FDS modalities is that for 6 and 8 m/s wind speed, FDS 'infinite friction' mode overestimate the separation distance between particle accumulation and solid obstacle location (therefore, underestimates the distance from inlet firebrand particles accumulate at); in contrast, FDS 'zero friction' mode underestimates the separation distance and overestimates the location from inlet where particle deposit. At 10 m/s ambient wind speed, both

FDS models underestimate the separation distance between particle accumulation and solid. The maximum accumulation location difference is ±4% for FDS 'infinite friction' mode and ±14% for FDS 'zero friction' mode. In the 6-8 m/s ambient wind speed range, the comparative analysis of the tested FDS modalities reveals a marginal discrepancy, with FDS 'infinite friction' mode slightly overestimating separation distance, and FDS 'zero friction' mode slightly underestimate; it can therefore be inferred that the true value lies within the margin of the two modalities results.

4.4 Discussion

To characterise the FDS Lagrangian Particle model sensitivity to firebrand accumulation position; a sensitivity analysis concluded that particle radius and density have the highest impact on landing location at low values, the impact decreases as the radius and density increase. An inverse sensitivity trend is calculated for ambient wind speed. The Tachikawa nondimensional parameter, ratio of aerodynamic to gravitational forces for a given particle, reveals a correlation between sensitivity coefficient and Tachikawa parameter for a given Tachikawa number (R^2 of 70% for linear trend). Particle position is also highly sensitive to inlet height (S_i=0.61) and inlet flow velocity (S_i=0.55). Equation 37 quantifies the relationship between particle acceleration and particle radius and density for different Reynolds numbers in FDS.

Particles creep movement is explored by reviewing established literature on sand bed movement in fluid flows and by comparing FDS 'infinite friction' mode and 'zero friction' mode simulations of a wind tunnel experimental set up investigating firebrand accumulation. FDS 'infinite friction' mode results can be interpreted as assuming infinite friction between particles and solid ground, and 'zero friction' mode as assuming zero friction. In the latter, particle trajectory is not influenced by contact with surfaces, and are moved by local wind flow until either being blown out of computational domain, or getting entrapped in local flow recirculation zones. This study explores the viability of both FDS modes to model firebrand creep movement and accumulation around a vertical wall obstacle by comparing simulation results to previously published experimental measurements.

The furthest accumulation location from firebrand inlet, measured by separation distance, difference between FDS results and experimental measurements is ±4% for 'infinite friction' mode and ±14% for 'zero friction' mode. Furthermore FDS 'infinite friction' mode better agree with qualitative observations presented in (Suzuki and Manzello, 2017) regarding particles accumulating in same area without increasing area size contrastingly to FDS 'zero friction' mode which shows accumulated area visibly decreasing as simulation time progresses. The particle accumulated area variation between 6 and 8 m/s wind speeds simulated with FDS 'infinite friction', corresponds to the change in area measured in experiments. Although the area is not calculated with FDS, the variation is recorded by comparing graphed accumulated particle position number of pixels. Figure 4-16 compares the slope, or area variation, of accumulated particles at different wind speeds. FDS 'zero friction' results of accumulated area are not compared to experimental results because its assumption

impedes any particle steady state accumulation to form. Particles are continuously moved by the local flow.

Results indicate that FDS 'infinite friction' mode is best suited to simulate and predict firebrand accumulation location and accumulated area, compared to FDS 'zero friction.' The accumulated area and location is estimated in simulation based on defined particle and inlet flow properties. Investigations connecting the size of firebrand accumulation and location to heat exposure value ranges can couple FDS results to more detailed estimate firebrand exposure.

FDS 'zero friction' mode includes firebrand particle creep movement and is therefore useful to simulate firebrand particles interaction with obstacles, or to simulate particles trajectories unlimited by effect of solid surfaces. In the next chapters, FDS 'zero friction' mode is selected to investigate the particle interactions with different obstacle configurations, exploring firebrand contact exposure on different obstacle shapes under 4-12 m/s ambient wind. The FDS mode unlimited by friction is selected to observe the most severe creep movement possible, estimating the possible particle trajectories in the computational domain. Results are interpreted as the worst-case scenario in terms of firebrand contact exposure with solid surface area; a methodology is proposed to quantify the simulation results in terms of firebrand exposure.

This study considered particle creep movement phenomenon in relation to wildfire firebrand exposure and accumulation for the first time. Although FDS Lagrangian Particle model has been leveraged to simulate firebrand trajectories on single building spatial scale (Moinuddin and Wadhwani, 2019; Mankame and Shotorban, 2021), the secondary particle movement trajectories influenced by interaction with obstacles and surfaces have never been included in the analysis. The current FDS capabilities to simulate firebrand creep movement and accumulation are measured and discussed in this study; the main limitation identified is that the physical interactions and forces between particles and the solid surfaces and particles are not calculated. FDS simulations with both assumptions still simulate particle trajectories with extreme or non-existent creep, providing estimation of the firebrand accumulation location and amount under varying ambient wind speeds.

A research need for firebrand particles creep rates and speeds for various surface roughness, and particle characteristics is identified. Creep movement has been investigated for sand particles experimentally to record creep rates; experimental methods include designing and testing sand traps which collect particles experiencing creep movement under various conditions, and photogrammetric methods which record particle trajectory and speed (Zhang *et al.*, 2021). Similar experiments can investigate the creep velocity for various firebrand particle; exploring different vegetation and materials (varying shape and weight), and the influence of firebrand combustion. Experimental measurements on the characteristics of firebrand creep under different conditions can provide data to improve simulation accuracy, and to inform decision on the most applicable simulation parameters for a given exposure scenario.

Recent full scale building wind tunnel experiments of firebrand exposure reported the firebrand accumulation amount in firebrand mass per area, by collecting firebrands in water pans located by the building walls; different collection locations, wind speeds and orientations are compared (Quarles *et al.*, 2023). Quarles et al. also observed increased accumulation at higher wind speeds, and in either the wall and ground intersection, or in recirculation zone windward of the building wall; showing transferability of the presented FDS simulation results to full scale building experiments. Quarles et al. commented their collection method prevented secondary creep firebrand movement on smooth ground surfaces that could occur on decks or patios. This investigation characterises the FDS model applicability to test both creep and accumulation, providing a methodology to simulate secondary movement that was not considered in experimental investigations. Combining both research tools and findings provides opportunity for a further-validated, estimation method for firebrand accumulation regions for different building designs and ambient conditions.

The results presented in this chapter characterise how FDS results can be applied and interpreted to quantify firebrand accumulation, and connect the field of sand creep movement to wildfire firebrand exposure; thus, introducing a possible research need to understand firebrand exposure on a single building spatial scale.

Chapter 5 : Firebrand Contact Exposure - varying solid obstacle geometry

5.1 Introduction

This chapter focuses on investigating the impact of different solid obstacle geometry on firebrand landing and accumulation processes. Chapter 4 explored the impact of firebrand particle properties and especially of local wind flow conditions with two FDS Lagrangian particle model modalities on simulating firebrand creep movement and accumulation. Here we extend the understanding of firebrand deposition subprocesses by simulating two additional solid obstacle geometries mimicking common WUI building component shapes, a re-entrant corner and a single horizontal step, as well as testing an additional higher ambient wind speed, 12 m/s.

The solid obstacles were primarily selected due to the simple shapes, which commonly occur in rural buildings. Steps and re-entrant corners are often present on the external walls, and around decks and windows of buildings; all components identified as vulnerable to wildfire ignition in Chapters 1 and 3. The re-entrant corner geometry has been highlighted in fire safety literature as creating a higher vulnerability to external fire hazard; façade tests highlight the importance of façade configuration, and have specifically tested re-entrant corners due to the additional associated fire hazard (White *et al.*, 2013). The vertical recirculation zones which can form with high wind speeds around this geometrical arrangement favour vertical flame spread and firebrand transport (Hakes *et al.*, 2017); this hazard-enhancement has been specifically identified in wildfire building damage surveys (Blanchi *et al.*, 2006). Steps are also very common WUI building features, which can occur around decks, windows, or other vulnerable regions of the external building constructions. This chapter investigates the horizontal flow recirculation zones which can form above steps, and its implications for firebrand accumulation hazards for the first time in literature.

The lowest ambient wind speed tested in the simulations presented in this chapter is 4 m/s, corresponding to the lowest wind tested in Chapter 4. This speed is selected to compare results and extend the previous analysis and results. Subsequently, 8 m/s, 10 m/s and 12 m/s wind speeds are tested; continuing the repetition of wind speeds tested in Chapter 4 for result comparison, and including an additional higher wind speed to the analysis. Wind speeds cited in literature during wildfire events repeat an average 12-13 m/s wind speeds, with maximum wind speeds reaching significant higher values. Testing the firebrand accumulation behaviour at a higher wind speed is, therefore, important. Santa Ana winds, strong and dry winds which regularly drive intense California wildfires, have been defined as having 13 m/s average speed (Billmire *et al.*, 2014); composite 'Santa Ana cluster' analysis resulted in maximum average wind speeds of 12 m/s (Hughes and Hall, 2010). In the European region, maximum mean wind speed of 13 m/s with gusts up to 30 m/s in northern

Adriatic have been measured (Tomašević *et al.*, 2022). 12 m/s is chosen to balance the high demand of computational resources associated with CFD simulations of high wind speeds, and assuming the maximum wind speeds are reached in open wildland settings, without solid obstacles slowing the flow speed.

5.2 Methodology

To minimise needed computational resources, simplify the computational domain used, and to maintain similarity between the simulations of each different solid obstacle geometry tested, the FDS computational domain dimensions are reduced. Figure 5-1 shows two computational domain schematic diagrams alongside relevant domain dimensions and features. The domain is a 10m × 10m × 6m cuboid, all boundaries are open except the solid ground floor boundary which is an inert non-slip boundary (shown in yellow in the schematic diagram) and the inlet wind flow boundary (the same boundary with the firebrand inlet vent shown), which introduces wind with a specified speed.

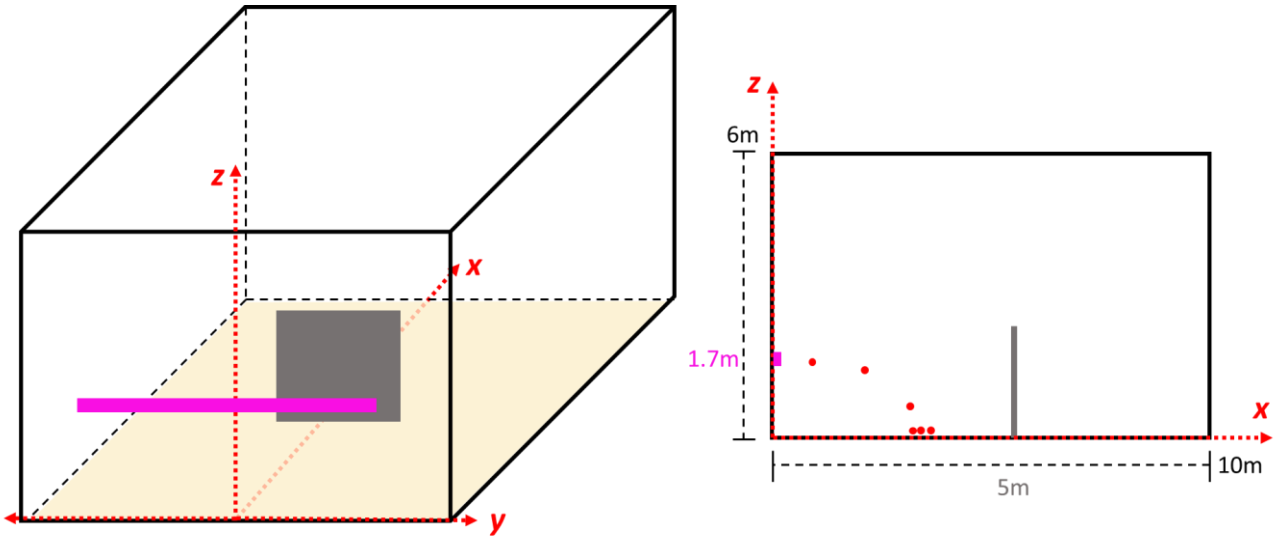

Figure 5-1: Schematic of FDS computational domain shown in 3D (left) and in 2D at the y=0 plane (right). Diagrams include firebrand inlet as a pink rectangle, and the solid obstacle location as grey square. Yellow surfaces represent inert non-slip solid boundaries.

The firebrand inlet vent is kept at the same height as the simulations presented in Chapter 4 (z_{in} = [1.6, 1.8]), with an extended width length, y_{in} = [-3, 3]). The inlet is extended in the y direction to enable observation of how the particles interact with the obstacle edges and. In real wildfire scenarios firebrands are lofted at the flaming fire front, and subsequently experience wind-driven transport from various initial heights and locations depending on the wildfire front location, fire intensity, and related smoke plume dynamics. Although the varying heights of firebrand injection are not tested in this investigation, the wider inlet expands the horizontal inlet locations, and the number of firebrands introduced in the simulation. Furthermore, the same particle properties as test B (presented in

Chapter 4 Table 4-2) are introduced; spherical particles of constant 50 kg/m^3 density and normally distributed radii between 2.5 and 7.5mm.

The obstacles are shown as a general wall in Figure 5-1; all obstacles include a wall component which is positioned in the same location (at x = 5, 5 m away from firebrand inlet, and y = 0). Four mesh grids are used to compute this domain: three meshes divide the bottom half of the domain (z = [0 -3]), at y = -2.5, and at y =2.5. One mesh covers the entire width for the top half of the domain (z = [3 -6]). The mesh grid size is δ = 0.05m in all meshes in the bottom half (z: [0-3]), and δ = 0.1m in the top half mesh (z = [3 -6]).

The different solid obstacles tested shown in the schematic diagrams in Figure 5-2: a vertical wall with the same dimensions (2.4m × 2.4m) as the wall tested in Chapter 4, a single horizontal step, and a re-entrant corner. The latter two shapes are added to a wall with the same dimensions, their additional solid obstacles are both 0.5 × 0.5m in cross-sectional area. The step location, therefore, is located at x_{step} = [4.5, 5] and z_{step} = [0, 0.5]; the re-entrant corner is located at x_{rec} = [4.5, 5] and y_{rec} = [-0.25, 0.25]. These dimensions are chosen to be realistic, and easily non-dimensionalised in relation to the firebrand and wind flow inlet, so this test can be repeated under various conditions.

The FDS Lagrangian particle model modality 'zero friction' is selected to observe the most severe creep movement conditions in the path of firebrand particles around these obstacles. Results are interpreted as the worst-case scenario in terms of firebrand contact with the largest possible amount of fuel surface area. The quantification of FDS results is conducted to provide insight on firebrand contact and accumulation risk areas.

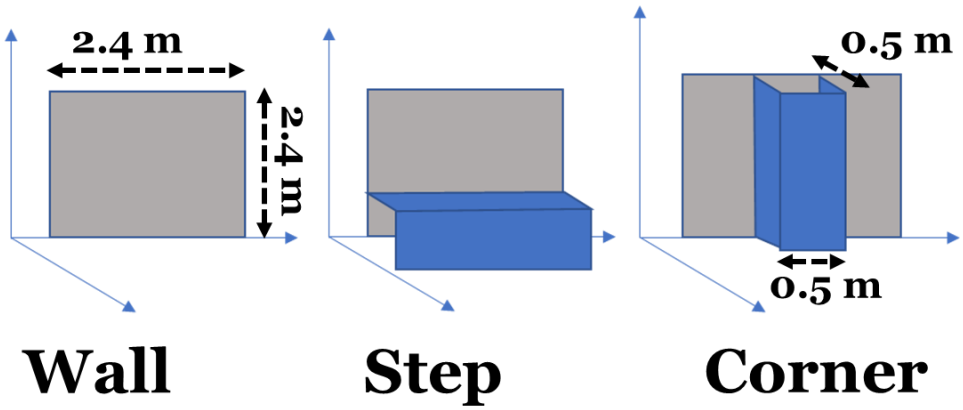

Figure 5-2: Schematic diagrams of three solid obstacles tested in simulations with dimensions. From left to right: vertical wall, step, and re-entrant corner.

Paraview 5.10.1 allows visualisation of wind flow streamlines around the obstacles in the simulations. The wind flow path around the obstacles can be observed, and the maximum wind velocity reached in the simulation is measured and located. The point cloud sphere determines which streamlines are visualised; this virtual sphere is set to have 0.5m radius, and to be centred at the (4,0,0) coordinates in the computational domain with the re-entrant corner and step obstacles. For

the vertical wall obstacle, the point cloud is centred at (4.5,0,0); therefore, the sphere is always centred 0.5m windward of the windward obstacle edge. This position is selected to best visualise the flow characteristics at the ground floor solid boundary, windward of the solid obstacle. Figure 5-3 presents the streamlines for the firebrand accumulation region mesh (located at y=[-2.5, 2.5], x=[0.10], and z=[0,3]) for 8 m/s wind speed at 60s simulation time. The figure shows the different re-circulation zones formed in front of each obstacle geometry. The flow characteristics around the vertical wall obstacle are discussed in section 4.2 of Chapter 4 where a similar analysis is conducted. The wind exposure on the re-entrant corner creates vertical recirculation zones that gradually decrease in diameter as the flow moves vertically upward. Instead of the horizontal windward recirculation created in front of the wall obstacle, the re-entrant corners create waves in the flow of the wake leeward of the obstacles. Two distinct flow patterns in the wake are observed, a primary more laminar streamline pattern originating from the impact with the obstacle section closest and perpendicular to the wind inlet, and a secondary stream which flows closer to the obstacle edge, characterised by more vorticity which originates from the vertical recirculation zones. Alternatively, Windward of the step obstacle, two recirculation patterns form in front of the step and above it; similarly to the re-entrant corner, the flow creates two wake flow patterns originating from each recirculation vortex.

The simulations are conducted for a total time of 60s to minimise computational resources; firebrand particles are introduced only once the flow in the domain is fully developed and reaches a quasi-steady state profile (t=10s). The analysis conducted uses the recorded particles position on the solid ground throughout the simulation duration and quantifies the number and location of firebrands path trajectory and the amount of time particles spend in any position.

Firstly, only the particle position coordinate on the ground floor ($z < 0.001$m are isolated). A bivariate histogram function is then applied to the particles x and y coordinates, the two variables of interest, for all simulation time steps conducted. We specify 50, 100, or 150 bins for each variable, this divides the computational domain ground floor length in the x and y direction (6m x 10m respectively) in either 50, 100, or 150 bins depending on the necessary resolution to interpret the data; unless otherwise specified, 100 bins are applied. The function calculates the number of data points, corresponding to particles, that pass within each bin. Given that data from the full 60s simulation is analysed, results provide the relative number of firebrand particles, and amount of time spent, in each bin location. Lastly the results are normalised: 0 corresponds to no particles passing the location indicated throughout the simulation, and 1 corresponds to the highest number of particles spending the longest time. This resulting number can be interpreted as the relative probability of firebrand contact with solid obstacles.

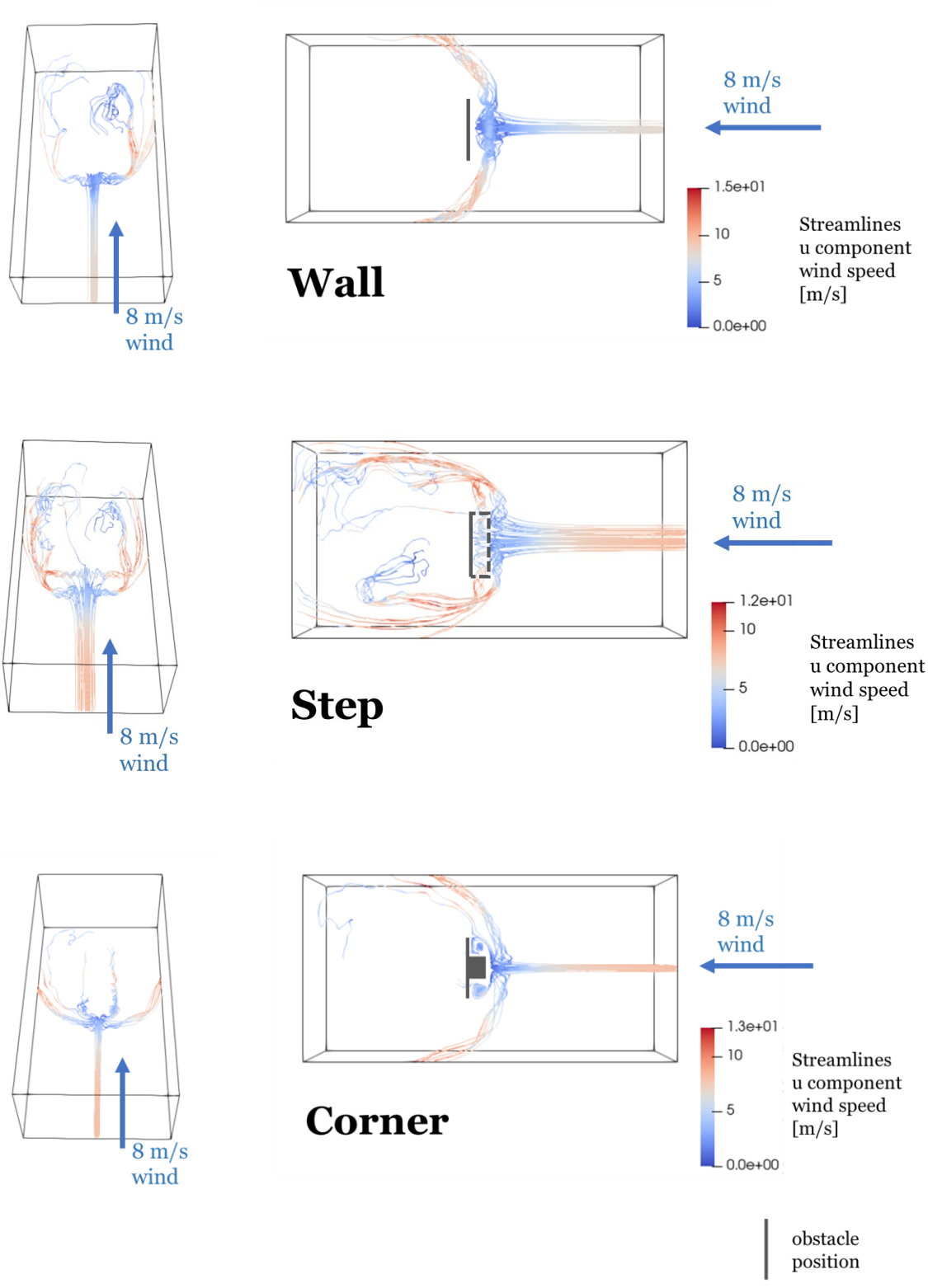

Figure 5-3: Streamlines in firebrand accumulation region for different obstacle geometries tested. From top: Re-entrant corner, vertical wall, and step geometry at 8m/s wind. Figures show the xy plane at z = 0 (left), and a 3D view from the (0,0,0) coordinate viewing angle.

5.3 Results

4 m/s wind speed is the lowest ambient speed tested, and resulted in nearly identical particle path for each solid obstacle geometry tested. This is illustrated by boxplots and histograms showing particle distribution along the x-axis of the computational domain ground floor for each obstacle tested at t=20s and t=60s in Figure 5-4. These graphs show that both at the initial landing particle locations, and after experiencing 40 seconds of creep movement, there is negligible variation between particle position at this ambient wind speed. The contact exposure maps showing particle path over time around the vertical wall obstacle are provided in Figure 5-5; showing particles approaching and following wind ward recirculation regions around the obstacle. Particle for all obstacle geometries landed on the ground in the same locations with negligible variation, creeping forward from the landing position without reaching the obstacle in the 60s simulated.

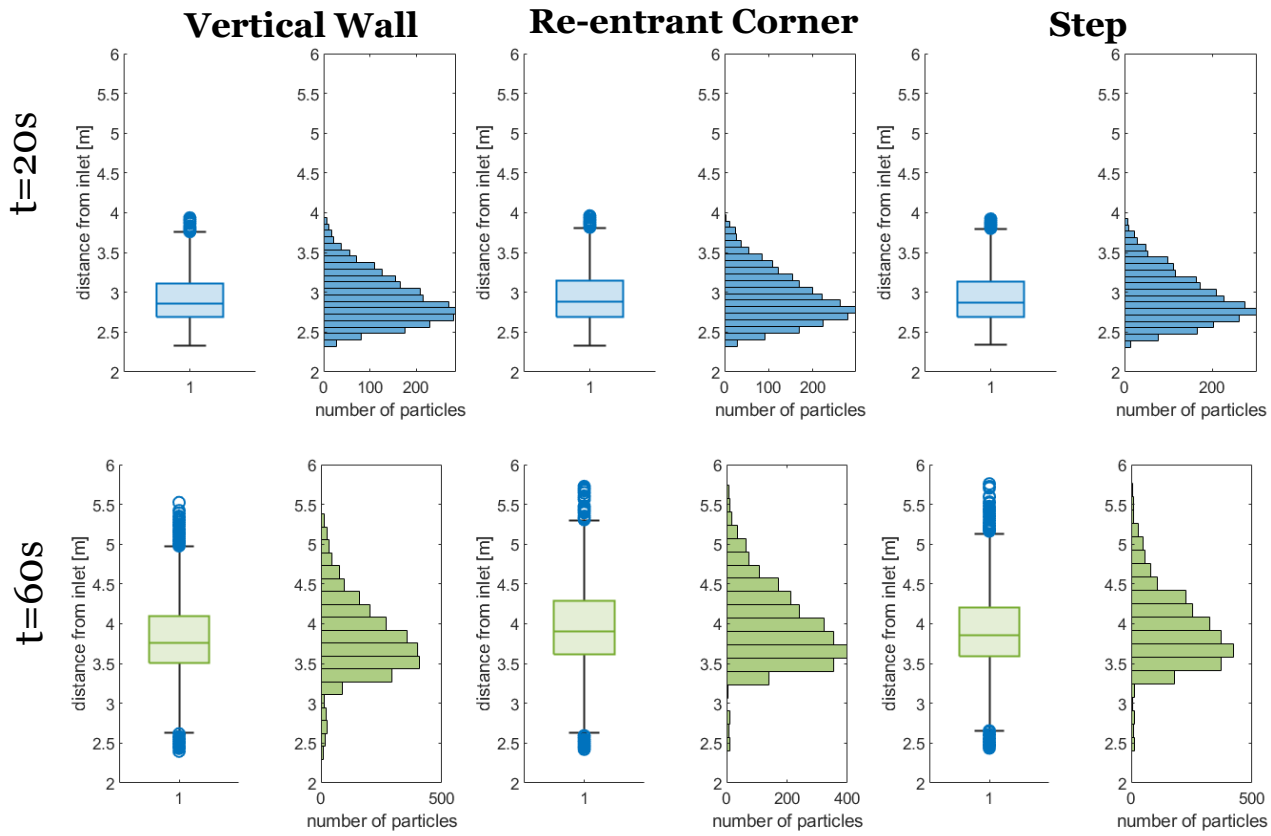

Figure 5-4: First deposition location at t = 25s (a) in blue, and particle location at t=60s (b) in green, of particle distribution on computational domain z=0 plane for each obstacle at 4 m/s wind simulated.

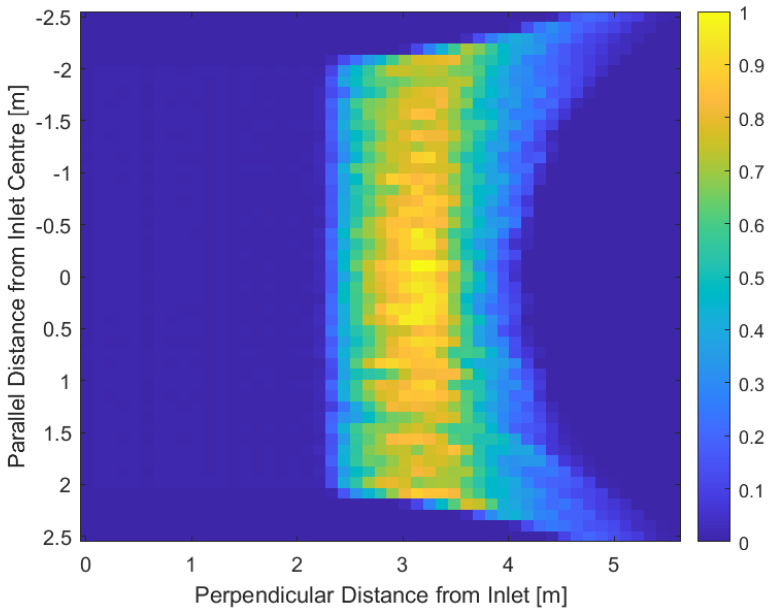

Figure 5-5: Firebrand contact exposure map showing firebrand particles position on computational domain floor around all obstacle geometry tested over 60 seconds of simulation at 4 m/s inlet wind speed with 50x50 histogram bins

In Sections 5.3.1 – 5.3.3 the firebrand contact exposure maps of relative particles path and contact with the computational domain solid ground (z=0 plane) are presented for each solid obstacle geometry: re-entrant corner, vertical wall, and single step respectively. In each section all ambient wind speed tested (8 m/s, 10 m/s and 12 m/s) are presented for comparison. The results are normalised: 0 corresponds to no particles passing the location indicated throughout the simulation, and 1 corresponds to the highest number of particles spending the longest time in the given location. This normalisation can be interpreted as following: at locations marked with 0 there is no firebrand contact, and therefore no probability of firebrand ignition; at locations marked as 1 there is the highest firebrand particles contact for the longest simulation time, and therefore the highest probability of firebrand ignition. The firebrand contact exposure map values do not, however, directly correspond the firebrand ignition probability, however, as this occurrence is influenced by a higher number of other factors (e.g.: target fuel material properties and conditions, firebrand particle temperature) which are not considered in this analysis.

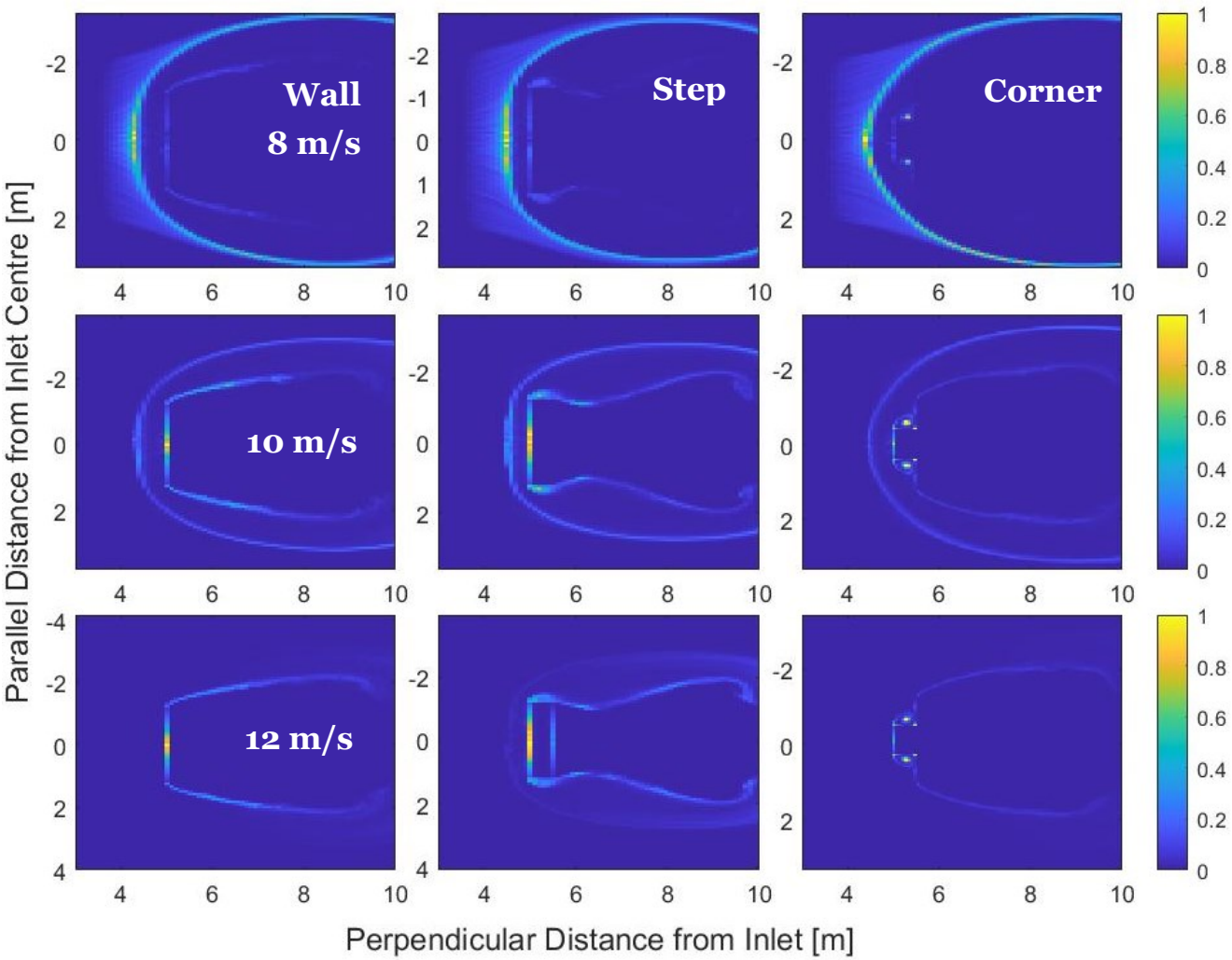

Figure 5-6: Firebrand contact exposure maps matrix showing firebrand particle position on computational domain floor over 60 seconds of simulation at 8 - 12 m/s inlet wind speed (top to bottom rows), for all obstacle geometries tested: wall, step, and re-entrant corner (left to right columns).

By coupling the understanding of the wind flow around the different obstacles with the probability of particle interaction with solid obstacle analysis; we observe two distinct regions of interest across solid obstacle geometries: the region windward of obstacles, and the leeward wake region. At the lowest ambient wind speed tested, 4 m/s, firebrand particle contact is limited to the windward region of all obstacles tested in the 60 seconds simulated. Firebrand particles first land 2-3m ahead of the firebrand inlet, and subsequently travel, through creep movement, towards the obstacle until approximately 4.5 m ahead of inlet, or 0.5 m windward of the obstacle, following the windward re-circulation zones formed around the solid obstacles; firebrands follow the same path pattern across all three obstacles tested. These results indicate that at low wind speeds, wildfire firebrands spend the longest amount of time in the vicinity of their landing location, experiencing

creep movement in the local wind flow direction. The creep movement which follows is slows and doesn't overcome the flow recirculation zones formed windward of the obstacles. In terms of WUI building safety, results are interpreted as indicating defensible space and indirect firebrand ignition are more probable at low ambient wind speeds.

8 m/s ambient wind speed simulations show the highest amount of firebrand contact with the ground floor occurring at the windward edge of the windward recirculation zone created in front of the solid obstacles, and follow recirculation zone edge along the outermost edge of the leeward wake. This thin region of high firebrand contact is very similar for the wall and step obstacles; characterised with highest contact in the region directly perpendicular to wind flow direction and firebrand inlet location. For the re-entrant corner obstacle, the highest contact region is this windward recirculation zone edge and the inner corners connecting to the vertical wall. The leeward wake shape is slightly narrower for the re-entrant corner obstacle compared to the wall and step obstacles. The path from the initial landing location (2-3m in front of firebrand inlet) to the recirculation zone windward of the obstacle, experiences the second highest particle contact, as particles move through creep movement toward the obstacle; this creep movement is expected in decrease with increasing surface roughness, increasing the amount of particle contact, and therefore increasing firebrand exposure hazard, in this windward floor region ahead of the obstacle. There is relatively minor particle contact recorded at the windward edge of all obstacles; the firebrands then follow the inner region of the wake flow leeward of the wall and step obstacles, but remain entrapped in the inner corners of the re-entrant corner obstacle without following the wake flow.

The higher ambient wind tested, 10 m/s and 12 m/s, illustrates how at higher wind speeds firebrand paths and contact with solid boundaries concentrate mostly at the intersection edge between the wall obstacle and ground floor solid boundaries. At 10 m/s the highest firebrand contact is at this intersection, with second highest firebrand contact traced at the edges of the leeward wake flow path (once again more so for the vertical wall and step obstacle, while firebrands are entrained longer in the inner corners of the re-entrant corner obstacle). Firebrand contact is also recorded, at a lower extent, at windward recirculation zones edges.

At the highest wind speed tested, 12 m/s, particle path regions differ most significantly between each solid obstacle. For the re-entrant corner geometry, the particles concentrate in the inner corners of the obstacle and in the related vertical vortices' centres, formed within the corners. The second most exposed section of the re-entrant solid obstacle is the section between re-entrant corners perpendicular to the wind flow direction and firebrand inlet. Particle contact is not observed in any other region of the ground floor. For the wall and step obstacle geometries, the highest particle contact is also experienced at the obstacle edge facing the wind flow and particle inlet direct, and the leeward wake edges. Around the step obstacle, however, an additional high-risk region is observed at the corner intersection between the wall and the step, this occurs at z = 0.5m. Particles at higher wind speeds spend the highest about of time at the intersection between solid obstacle and ground floor,

and any additional solid corner intersections of the obstacle; the second highest risk area is the edges of the wake especially at the immediate lateral sides of the solid obstacle. Results agree with published full-scale building experiments of firebrand exposure at 10.3 m/s and 17.4 m/s which observed greatest amount of firebrand accumulation at the ground and wall obstacle intersection and at a windward recirculation zones away from the building (Quarles *et al.*, 2023).

5.4 Discussion

This chapter presents FDS 'zero friction' mode simulations of wildfire firebrands, simulated as Lagrangian particles of constant mass and density with normally distributed radius between 2.5mm and 7.5mm, introduced with four ambient wind speeds (4, 8, 10, and 12 m/s) towards three different solid obstacle geometries mimicking common WUI building components. A re-entrant corner wall obstacle and a vertical wall obstacle are tested to represent common geometries of building external walls, fences, or sheds. A single step addition to a wall is tested to represent stairs, or any horizontal addition to vertical walls which can be present under doors and windows. The wildfire vulnerability of building components mentioned is discussed and justified in Chapter 1.

Following the particulate wind transport theoretical overview in Chapter 3, and the computational investigation of particle and wind flow characteristics influence on particle deposition and accumulation in FDS 'infinite friction' mode and 'zero friction' mode in Chapter 4; this Chapter explores the impact of varying target obstacle geometry on particle landing and creep moment. FDS Lagrangian particle 'zero friction' mode is chosen to investigate how varying inlet speed will influence particle interaction with different solid geometries by computing an extreme interaction between particles and solid boundary without friction impediment. By computing the relative number and time spent by firebrand particles on the computational domain floor, we quantify the interaction between particles and possible target fuel surfaces. This quantification can be interpreted as the area locations with highest probability of firebrand exposure.

This chapter applied a practical quantification method of firebrand contact around solid obstacles, to observe firebrand exposure hazard zones. Results conclude, at all wind speeds tested, that the innermost corners of vertical re-entrant corners wall assemblies experience particularly high firebrand exposure. Around a step obstacle, the highest wind speed tested (12 m/s) allowed firebrand particles to come to contact with step's top surface and supporting back wall intersection; thus identifying an additional hazardous zone not reached by firebrands at lower speeds. Results indicate that the lower ambient wind speeds tested (4 m/s and 8 m/s) favour creep movement around the immediate firebrand landing location in the direction of local wind flow. The amount of particle creep movement will be influenced by surface roughness and firebrand shape qualities; quantifying and the impact of these influencing parameters on firebrand creep movement is a future research need. The presented quantification method allows quantification of firebrand contact hazard zones around

obstacles. The quantification method can be applied to any high-risk building component to quantify possible firebrand contact exposure under defined ambient conditions.

This research methodology and results contribute to current state of the art literature on quantifying and identifying WUI building wildfire ignition mechanisms. Vacca et al. presents a Performance Based Design (PBD) for single building scale wildfire vulnerabilities and design; a fault-tree is included identifying the commonly observed patterns of nearby flaming fire sources process of entering the building (Vacca *et al.*, 2020). Because the flaming fire sources of interest (identified as fuel burning in roof or in gutters, and various fuel types burning near building) are most often ignited by firebrands, the firebrand contact exposure map analysis can provide useful and quantitative estimation of where firebrand contact exposure is likely to occur around a given building. This analysis can be applied to the proposed PBD methodology to first identify the likely fire sources under different ambient conditions. Vacca *et al.*, 2020 proposed PBD approach then can be used to quantify the heat flux information that defines the building deisgn requirements.

The location most likely for firebrand accumulation can therefore inform the prediction of indirect firebrand ignition mechanism for building ignition. In direct firebrand ignition of buildings, the construction material is directly ignited from the heat flux produced by combusting firebrands. The ignition and heat transfer mechanisms of target fuels exposed to firebrands has been experimentally investigated for commercially used construction materials including woods (Santamaria *et al.*, 2015), insulation materials (Wessies *et al.*, 2019), decking slabs materials (Meerpoel-Pietri *et al.*, 2021). These investigations provided valuable specific insight into the heat transfer mechanisms, and specific material responses. The firebrand contact exposure maps can be used in the design of WUI buildings to identify which materials and regions are at high-risk; limiting the number of materials which these ignition tests are required for. Combining experimental and computational methods provides a road map for how to best consider and justify firebrand exposure in building design.

A limitation of the presented study is its consideration of simple obstacles in isolation, without considering the influence and effect of a full building structure and nearby obstacles and structure which influence the local wind flow. Firebrand exposure wind tunnel experiments considering the impact of full building construction and variation in wind orientation are available in literature (Nguyen and Kaye, 2021, 2022a; Quarles *et al.*, 2023). Experimental studies considering all influencing factors conclude that ember contact with roof top is a complex and not easily defined correlation to the building shape, roof angle, and wind angle; as with building vulnerable features, all influencing parameters are significantly contributing therefore retrieving simple guidelines to limit damage is challenging (Nguyen and Kaye, 2021). Observation note that increasing wind speed generally reduces the roof area with stationary firebrands, and a relationship high firebrand creep movement, no accumulation, and high rooftop pressure and shear stress loads (Nguyen and Kaye, 2021). However certain tests in the full scale building experiment collecting firebrands landing in the

immediate surroundings of buildings recorded increasing firebrand accumulation with increasing wind speed tested (Kadel *et al.*, 2021).

The presented investigation and quantification methodologies can be applied to test simpler exposure domains, with additional varying wind orientations, to test the repeatability of these observed trends in firebrand accumulation amounts. Coupled with selected wind tunnel experiments, simplified FDS computational domain exploring the relationship between wind flow, surface roughness of material, and firebrand accumulation amount can be validated; there is a research need for applicable methodologies and conclusions that can be directly applied in the WUI building design or retrofit process.

The presented methodology offers a valuable component that can be coupled with PBD and small-scale experimental investigations on firebrand accumulation and the firebrand ignition propensity of different materials to create a quantitative, tailored methodology to evaluate the ignition and damage risk of WUI buildings, or building components.

Chapter 6 : Firebrand Protection Measures

6.1 Introduction

6.1.1 Firebrand Protection Measures

Existing practical and applied protection measures for WUI buildings consist of maintaining defensible space in the immediate surroundings of the building to prevent indirect ignition, and installing screens to any vents or openings in the buildings to prevent entry and direct ignition. More specifically, WUI-tailored building construction regulations (the Australian Standard of buildings in bushfire-prone areas, the California Building Standard Chapter 7A, and the International Code Council WUI Code) require screens with openings ranging from 0.03 cm^2 to 0.40 cm^2 area size (Manzello and Foote, 2014). A recent systematic review of international WUI fire safety codes and standards highlights a lack of codes focusing on building construction and especially on firebrand exposure threat (Intini *et al.*, 2020). Although defensible space and vent screens are crucial for wildfire resistant buildings, these measures do not address direct firebrand ignition occurring through accumulation on building components. This is sometimes addressed by testing material response simulating firebrand ignition exposure as a pilot flame. Recent research began addressing this issue by proposing a standard fire curve for firebrand accumulation on building exterior calculated via experimental measurements of controlled burning firebrands (Cantor *et al.*, 2023).

In this chapter we review literature on firebrand ignition protection measures, and consider the more mature and practically applied sand mitigation measures to draw lessons for firebrand accumulation mitigation and protection. Table 6-1 lists recent studies on firebrand protection measures along with a brief description.

Table 6-1: List of academic research publications on firebrand protection or mitigation measures

Protection Method	**Brief Description**	**Reference**
Vent Screens	Experimental investigation of unconsidered characteristics influencing wire screens protection performance against firebrand entry. Results indicate screen porosity, screen type, and wind speed are significant influencing parameters for performance, while screen orientation is less influential on screen performance.	(Hashempour and Sharifian, 2017)
Full-house fire blanket	Takahashi tested building-scale fire blankets in the laboratory and under prescribed wildland fires exposures. By enclosing the full building in a fire blanket, firebrands are blocked from entering and accumulating on vulnerable feature. Laboratory tests resulted in 92% protection from convective heat and up to 96% protection from radiative heat.	(Takahashi, 2019)

Fire Retardants	Laboratory investigation of fire retardant treatment effect on firebrand production by wooden roofs. Wind tunnel experiments at 6 and 8 m/s found that roof assemblies (cedar shingles and cedar shakes) treated with retardant produced little or zero firebrands, while untreated assemblies produced more firebrands.	(Suzuki and Manzello, 2021c)
Acoustical Extinction method	Laboratory experiments found the minimum sound pressure threshold to extinguish a burning and moving firebrand particle. 20 mm diameter dry wood spheres, burning with a 250 W flame, are connected to a pendulum system to simulate firebrands. The extinguishment sound pressure threshold increases with sound frequency, and decreases significantly with increasing firebrand traveling speed.	(Xiong *et al.*, 2021)

In an effort to meaningfully connect and learn lessons from the mature research field on sand hazard and accumulation on infrastructure, this chapter objective is to analyse applied sand mitigation measures to extract transferable knowledge and propose applicable measures for firebrand direct ignition mitigation. Section 6.1.2 reviews different sand mitigation measures and justifies which types of mitigation measures are applicable for firebrands exposure mitigation by evaluating their physical driving processes. Section 6.2 presents a simple exploratory computational methodology to investigate the application of one type of sand mitigation measure to a previously tested firebrand exposure scenario (previously tested in Chapter 5). In closing, Section 6.3 reflects over the exploratory results and simple methodology considered, to offer comments on the application of this mode of particulate accumulation mitigation, and reflect on research and engineering gaps for more comprehensive wildfire firebrand protection for houses.

6.1.2 Sand Mitigation Measures

Section 3.2.3, Chapter 3 reviewed the transport modes of sand particles and outlined the relevant comparison between the physical considerations of sand and firebrand exposure processes. In this section we look at larger scale engineering solutions for sand accumulation on infrastructure to analyse whether valuable lessons and principles can be transferred to firebrand exposure. Although there are inherent differences between sand and firebrand hazards on infrastructure, there are also important similarities. In Figure 6-1 three of the most important physical differences and similarities between the two exposure processes are outlined. Sand and firebrand particles share the similarity of being compromised by varied chemical composition, mass, size and shape. The size distribution of sand particles average range is smaller compared to firebrand particles distribution; this results in the four modes of transports experienced by sand particles, reptation, saltation, creep and suspension, which were discussed in Section 3.2.3. Firebrand particles are involved in an ongoing combustion reaction and the heat they transfer to the target solid obstacles they interact with defines the extent of their exposure hazard. There are also important differences in the characteristics of the two exposure

processes. Although both are particulate transport in the atmospheric boundary layer processes, sand transport and accumulation are relatively slow gradual and nearly continuous processes occurring over extended periods of time; contrastingly firebrand exposure is sudden, occurs seasonally during fire events, and is characterised by high intensity temperatures and wind.

In this introduction section we highlight the applied engineering mitigation developments for both hazards and compare and contrast their applicability.

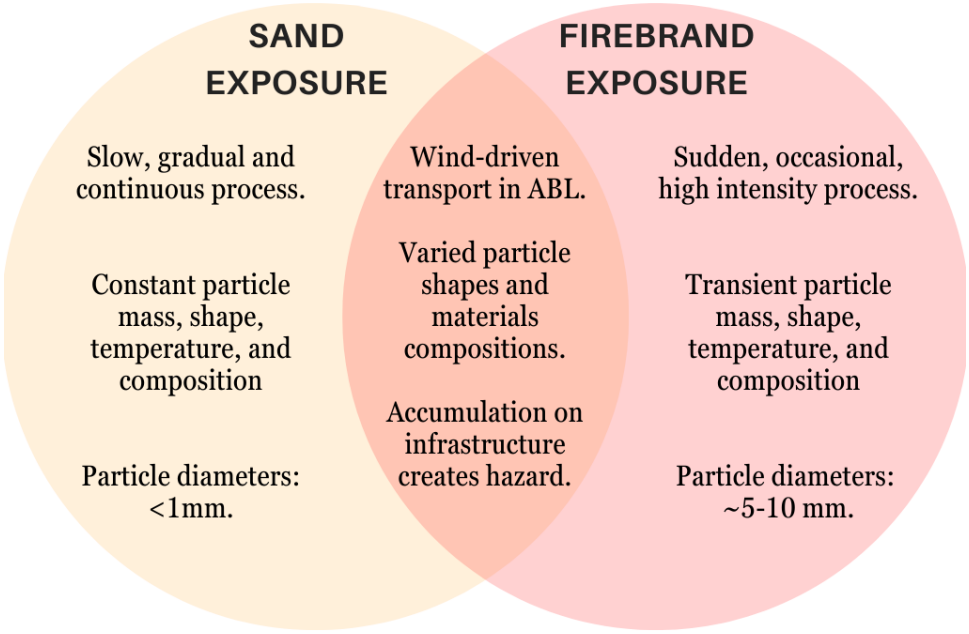

Figure 6-1: Venn Diagram comparing sand transport process and hazard on infrastructure, to wildfire firebrand processes and hazard.

A number of different sand mitigation measures have been explored in literature and applied as practical infrastructure protection. Characterisation frameworks have been presented in literature to group the available protection systems based on different relevant aspects (Rahim, 1945). One framework characterises whether the mitigation measure provides protection, stabilisation, or land management to mitigate the hazard impact (Stipho, 1992), based on which protecting principle the mitigation measure offers, e.g. sand-resistance, sand-stabilisation, or sand-guidance (Cheng and Xue, 2014). In this section we focus on a more recent framework, which divides mitigation measures based on which part of the component in the sand-infrastructure interaction system is influenced; "the source, path, and receiver" characterisation (Bruno *et al.*, 2018). The mitigation measure are, in this characterisation, divided based on whether they act on the particle origin location, transport trajectory location, or target location; these location areas are labelled in Figure 6-2 for both sand hazard and firebrand hazard. Given we are analysing the theoretical applicability of sand mitigation measures to wildfire firebrands, without the practical details of a specific application site and wildfire occurrence event; the origin, transport trajectory, target characterisation framework will aid us in

reviewing the theoretical principle behind mitigation measures, and to extricate the most applicable protection measures for wildfire exposure.

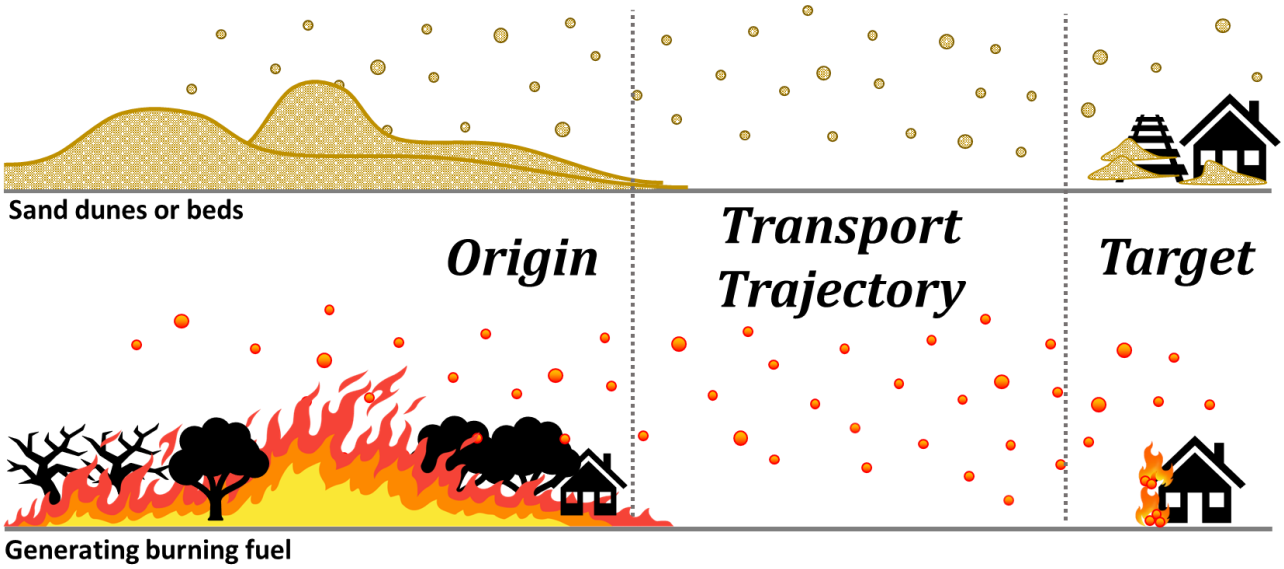

Figure 6-2: Diagram illustrating the origin, transport trajectory, and target parts of the sand-infrastructure and firebrand-infrastructure interaction systems. Wildfire flames illustration is from (*Fire Illustration*, 2023).

Origin mitigation measures aim at reducing the amount of wind-blown sand by either modifying the sand beds properties, or the local wind flow field at the origin location of wind-blown sand; an applied example is (Escadafal *et al.*, 2011). Layer systems, for example, refer to protection methodologies that increase the moisture content of sand and thus increase the cohesive forces between sand grains thus increasing the wind velocity threshold necessary to mobilise sand (Belly, 1964). Hedge systems, on the other hand, create obstacles across the sand bed which hold the sand grains by increasing the aerodynamic roughness of the ground and thus reducing the shear stress of the exposed sand bed. The most commonly applied hedge system consists of a number of obstacles arranged to create half-buried square or rectangular compartments (Gillies *et al.*, 2006; Gillies and Lancaster, 2013). The created compartments in the hedge protection method modify the local wind flow; the aspect ratio (width: depth) of the compartment enclosure is the principal determinant of the flow regimes which occur within the compartments (Oke, 1987). Most applications for sand flow mitigation using this system have an aspect ratio of approximately 10; within this geometry the flow creates one large vortex immediately downwind of the windward compartment edge, and secondary smaller vortex where flow recirculated again windward of the down-wind compartment edge (Bruno *et al.*, 2018). Another common arrangement using the aerodynamics change principle consists of line obstacles placed perpendicularly to the predominant wind direction.

For firebrand exposure, the layer origin mitigation measures are conceptually parallel to wood retardant protection treatments used to inhibit firebrand generation because moisture or chemical modification to generating firebrand fuel can reduce the amount of generation from a given flaming fuel; as the example cited in Table 6-1 which studied fire retardant impact on urban fuel firebrand production (Suzuki and Manzello, 2021c). Contrastingly, origin hedge mitigation systems for firebrands will likely not be especially effective because in contrast to sand which is lifted from the ground by the local wind flow, firebrands are generated from higher lofting heights; therefore, modifying the aerodynamic conditions at the generating location is more challenging. Furthermore, the generating origin will involve a wildfire, an unpredictable uncontrolled burning location with smoke plume and highly transient and unpredictable aerodynamic conditions. Given this thesis research focuses on firebrand landing processes, and the firebrand generation properties and processes have not been investigated in depth, the origin of mitigation measures will not be considered in more detail.

Transport trajectory mitigation measures also act to impact the aerodynamic principles driving wind-blown particulate hazard, focusing on the location of the wind-blown particle trajectory between the origin and the target infrastructure (Bruno *et al.*, 2018). The introduced trajectory obstacles promote particulate sedimentation by decreasing wind speed along the trajectory and inducing flow recirculation in designed areas. The general aerodynamic conditions around fences are widely researched in literature (Hong *et al.*, 2015), and this has been applied strategically to inhibit sediment accumulation. Mitigation measures against sand (McLaughlin, 1942) and snow (Tabler, 1994) accumulation have been applied as (i) fences altering the wind flow towards the impacted infrastructure, and (ii) ground surface geometry modifications, e.g. creating trenches, hills. All measures promote the sedimentation of sand in a safe area away from the protected infrastructure. The orientation of these protecting fences or features is important; implemented solutions are usually designed with a 90° between the fence longitudinal axis and the prevailing wind direction (Bruno *et al.*, 2018). Both experimental and computational investigations of the aerodynamics and particulate sedimentation behaviour occurring around various types of fences are available in literature (Hotta and Horikawa, 1990; Dong *et al.*, 2007). The surface geometry modifications are influence by their size and geometry (determine by their height, width, and the slope of their contours). In this chapter we conduct a simple preliminary analysis, using FDS, testing the applicability of a trajectory surface geometry trench mitigation measure for firebrand protection.

Lastly, the target mitigations are protections installed directed on the potentially impacted infrastructure. Aerodynamic-based target mitigation measures protect specific portions of the infrastructure with shields impeding accumulation of sand particles on crucial components. A shield modifies the particulate wind-driven trajectory by accelerating the particulate flow over the crucial infrastructure and encouraging deposition and accumulation in safe areas (Bruno *et al.*, 2018). Patents for these protection systems applied to sand (Guangyong and Peng, 2012) and to snow (Sato

and Ono, 1990) are available. Similar protection systems can be designed for WUI building components vulnerable to firebrand ignition; such as gutters, where dry vegetation can often accumulate and wildfire firebrands can easily land and ignite combustibles, or on decks and porches (see Chapter 1 and 3 for detailed discussion of vulnerable building components to wildfire ignition). Target mitigation measures can also modify the target itself, through specific material selection and design to render the target exposure-resistant. Using fire-resistant materials, and applying finely-meshed screens to any vents or openings, are examples of available target-protections proposed and applied to protect WUI building targets from firebrand exposure. Specific protective structures as used for sand and snow can be explored and tested in the future for possible additional firebrand exposure protection.

In Chapter 5, the FDS investigations of firebrand particle contact exposure with three obstacles geometries at different ambient wind speeds, firebrand exposure location for different conditions were defined. For lower ambient wind speeds ($\vec{u}$ < 8 m/s) the trajectory location, windward of the obstacle, are most exposed to firebrand particles. Trajectory mitigation measures are therefore most important for these conditions. As wind speed rises ($\vec{u}$: 8 - 10 m/s) the edges of the recirculation zones formed around solid obstacles and the intersection between solid obstacle and ground experience a higher firebrand exposure. As wind speed rises the leeward wake edges experiences higher firebrand exposure. At the highest wind speed tested ($\vec{u}$: 12 m/s) the highest firebrand exposure regions are at the solid obstacle and ground floor intersection, and to a lower extend at the edges of the leeward wake region.

6.2 Methodology

In this section, we present simple exploratory FDS simulations testing the effectiveness of a transport trajectory trench protection measure to mitigate firebrand exposure. Integrating the knowledge regarding firebrand deposition and accumulation processes physics, and FDS computational model characterisation from earlier chapters, we provide a preliminary methodology to use this computational tool to test the impact of a trench mitigation measure for firebrand exposure protection.

6.2.1 Simple Exploratory Domain

Figure 6-3 shows a schematic of a the computational domain that is first tested. As shown in the 2D computational domain slice at y=0 schematic, the 1 m wide trench was tested at four different locations (5 - 6m, 6-7m, 7-8m, and 8-9m distanced from firebrand inlet). The same computational meshes and mesh grid sizes are used as those presented and described in Chapter 5. The wind inlet flow is introduced at x=0 computational plane, where the firebrand inlet vent is located. For this exploratory simulations, wind speeds of 8 m/s and 10 m/s are tested.

The presence of the trench in the ground boundary changes the flow profile by creating a recirculation zone characterised by much slower flow movement. Streamlines, computed with Paraview at the centre (relative to the y-axis) of the trench protection feature, visualise this recirculation zone in Figure 6-4.

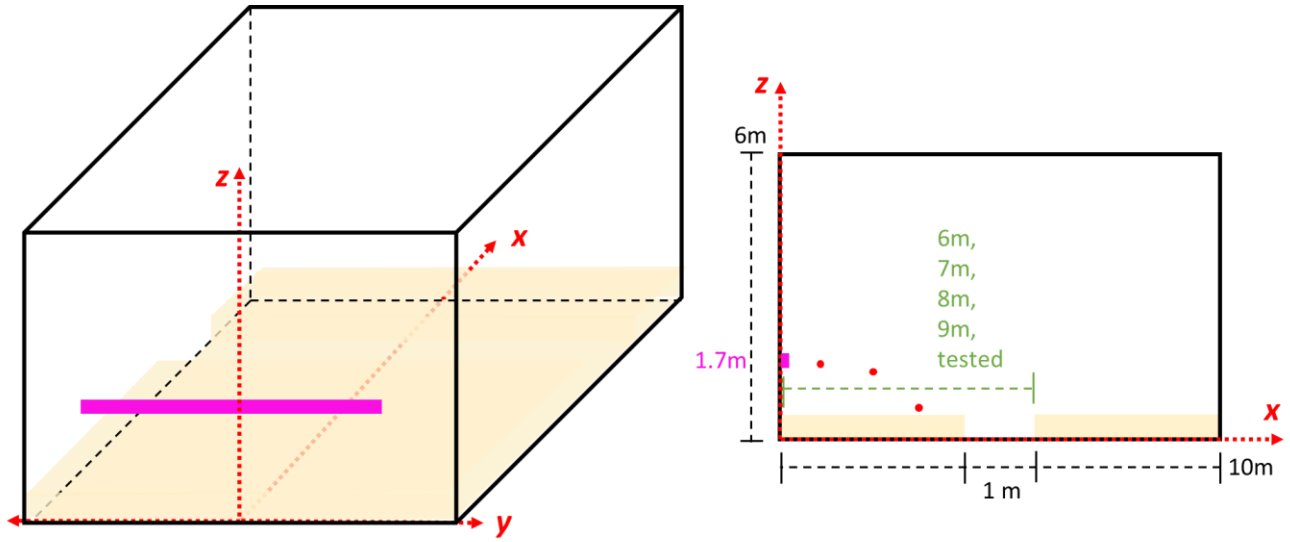

Figure 6-3: FDS Computational domain schematic of (left) 3D domain description and of (right) 2D slide at y = 0 which firebrand inlet illustrated as pink rectangle, and solid non-slip boundaries as light yellow.

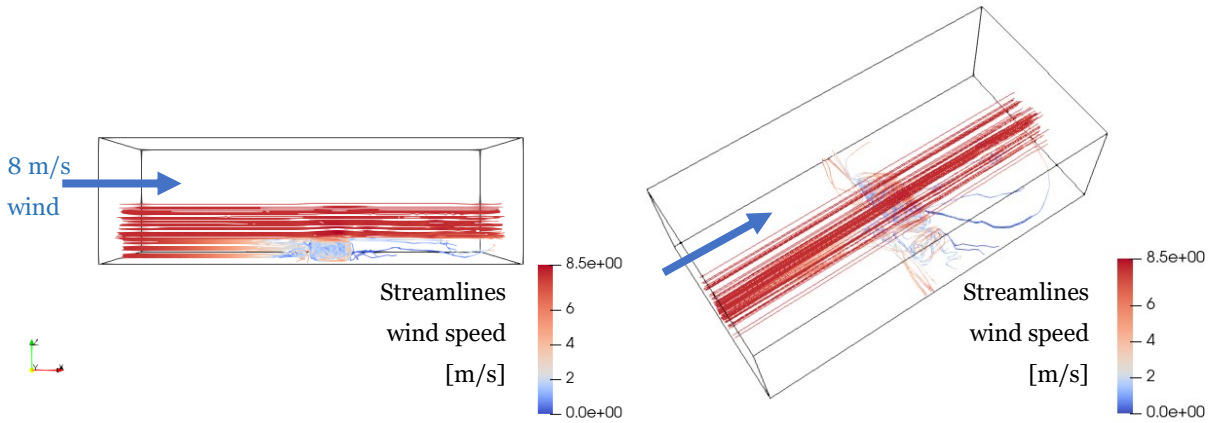

Figure 6-4: Streamlines computed for flow occurring at the center of the y-axis of the computational domain, and the streamlines passing through 0.5m depth inside the trench, and 0.5m above the trench with 8 m/s ambient wind speed.

In this illustrative analysis, ambient wind speeds of 8 and 10 m/s are tested, and FDS modality simulating 'zero friction' between particles and solid ground boundary used. This selection is applied in order to observe the particle path and their interaction with the trench protection in a simulation maximizing particle creep movement, and at wind speeds which would likely result in firebrand exposure to the ground floor in the particle transport path region, before reaching the solid obstacle.

6.2.2 Re-entrant Corner Application

To further test this trench protection measure, and apply it to a previously tested wall obstacle, we run a 8m/s wind simulation with a trench protection measure windward of a re-entrant corner wall obstacle. The trench protection introduced has 1.5m width, located at x_{trench} = [4, 5.5], 0.5m depth at z_{trench} = [0, 0.5], and 5m length y_{trench} = [-2.5, 2.5], (the full computational domain with in the y-axis direction), is introduced in a computational domain identical to the 8 m/s re-entrant corner wall obstacle tested in Chapter 5. The computational domain with the trench protection only varies in the firebrand inlet, and wall obstacle being raised 0.5m in the z-axis direction, to account for the additional 0.5m trench inserted in the ground floor. The impact of the trench protection on the local wind flow at 8 m/s ambient wind speed is visualized with Paraview streamlines in Figure 6-5. The streamlines are generated with a point cloud sphere centered in the middle (y = 0) of the computational domain and trench protection (x = 4.5, z = 0.5) and with a radius of 1m to also visualise the streamlines passing over the trench protection. Recirculation zones and stagnant linear streamlines are formed inside the trench protection. This modification in the local flow streamlines, also inhibits the formation of vertical recirculation zones around the re-entrant obstacle corners to a certain extent.

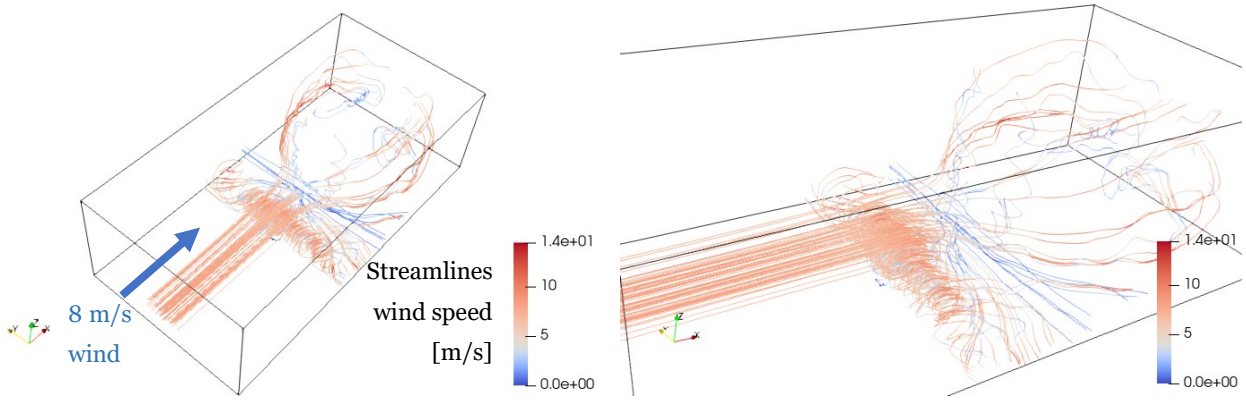

Figure 6-5: Streamlines computed in the trench protection y-axis centre, with ambient inlet 8 m/s wind and a re-entrant corner wall obstacle.

6.3 Results

6.3.1 Simple Exploratory Domain

Figure 6-6 shows the particle trajectories in the simple exploratory simulations with two trench location cases at each wind speed tested. The 'zero friction' FDS modality results in all particles landing between particle inlet and trench, moving through creep movement into the trench protection; the speed at which this occurs, and therefore the time length which firebrand particles will be in contact with the ground floor, depends on local flow conditions, and ground floor surface roughness. Both graphs included in Figure 6-6 also show that a percentage of particles land past the trench location and therefore miss the protection measure. This indicates a limitation of the simulated trench location, for the particular firebrand inlet, ambient wind, and solid boundary conditions simulated. This limitation, in a design process, can be addressed by either moving the trench location closer to the obstacle location, or designing a wider trench protection.

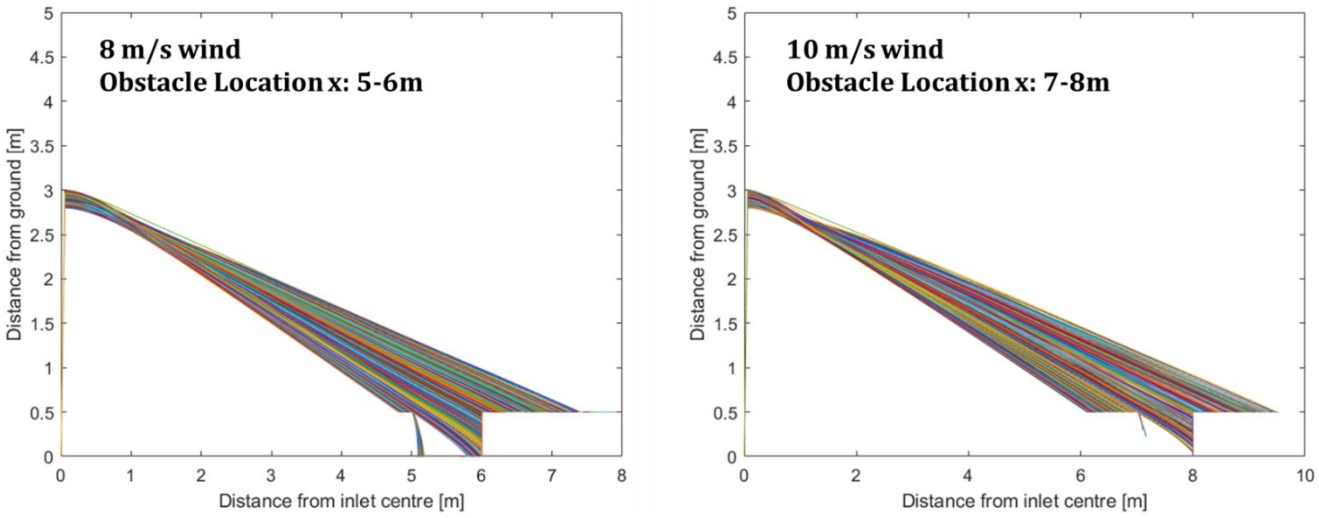

Figure 6-6: Particles trajectory in FDS simulation from inlet location to ground floor. (left) Graph shows trench located at 5m – 6m distance from inlet with 8 m/s ambient wind speed, and (right) graph shows trench located at 7m-8m distance from inlet with 10 m/s ambient wind speed.

The chosen mitigations for a more detailed design will depend on the most likely experienced wind speeds during local wildfire scenarios, and the vulnerability of the design the protection measure is designed to protect. Probable wind speed information can be accessed in local weather stations and local wildfire statistics or reports. Design vulnerability, as discussed in detail in Chapter 1, will depend on the geometry and construction materials of the target infrastructure components. For firebrand exposure specifically, the smoothness or roughness of the ground floor material which leads up to the protected building or infrastructure is of specific interest. The lower the surface roughness is the more valid will the zero-friction assumption be; cement, smooth stone, laminated timber, for example, can favor uninhibited creep movement of firebrands toward the obstacle. Alternatively, surfaces with

higher surface roughness, for example earth and grass, will inhibit the creep movement and favor firebrand accumulation. The flammability of the material in question should also be considered in the design decisions.

Figure 6-7 summarises the percentage of particles in the simulations conducted which end up being located inside the trench protection measure. In this simple computational domain tested, with the 'zero friction' FDS modality, there is a straightforward relationship between ambient wind speed, trench location, and the percentage of particles which end up in the protective trench. We note that this chapter, rather than a comprehensive and in depth research study of the feasibility of the trench protection measure serves as an exploration of (i) the applicability of this protection measure in protecting a specific vulnerable WUI obstacle from firebrands and (ii) of the applicability of using FDS, a widely used CFD software in fire protection engineering, to test the protective ability of such a measure. For these purposes, Figure 6-7 suggests a simple visualization calculation for how fire protection engineers can utilize FDS to test the extent of a similar protective measure for firebrand exposure around a given obstacle or vulnerability at different wind speeds and protection design parameters. For the trench protection to inhibit firebrand ignition and subsequent fire spread, the trench must be constructure or filled with a completely fire-resistant material. Sand is a known fire-resistant material which, as water, is used to extinguish fire. Filling a possible trench protection measure with sand or water can ensure fire cannot ignite and spread from the protection location.

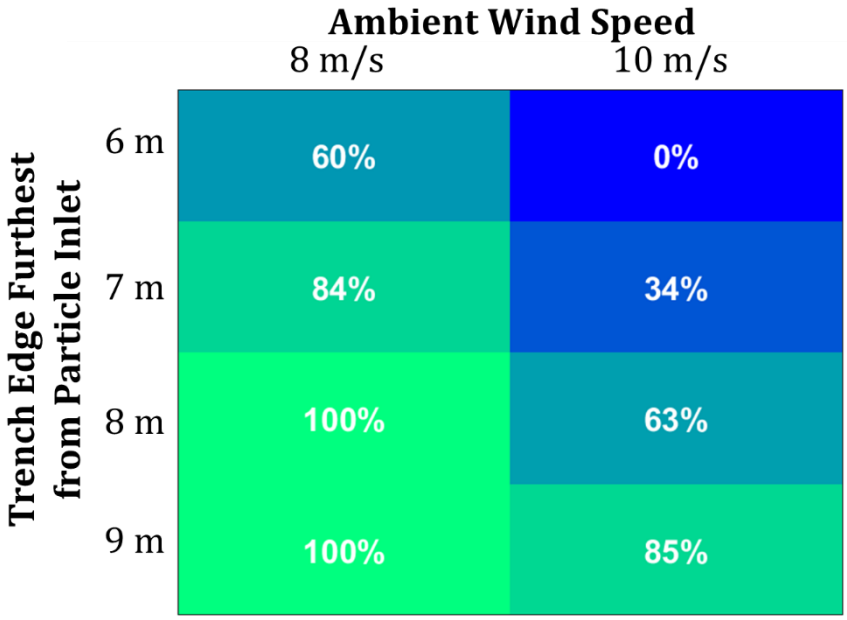

Figure 6-7: Matrix of percentage of particles which are located in protecting trench at completion of simulations for all ambient wind speeds (8 m/s and 10 m/s) and all trench locations tested.

6.3.2 Re-entrant Corner Application

The applied trench protection in the exploratory firebrand exposure domain on a re-entrant corner wall obstacle resulted in the prevention of most firebrand particles reaching and coming to

contact with the re-entrant corner wall obstacle. Figure 6-8 shows screenshots of SmokeView visualisations of the two FDS simulations with and without the trench protection measure at 30 seconds of simulation. Section 5.3.1 and Section 5.4 in Chapter 5 present and discuss the firebrand exposure contact with results when firebrand particles are exposure toward a re-entrant wall obstacle without any protection measures. Introducing a trench immediately windward of the re-entrant corner prevents most of the inserted particles from reaching the obstacle. This is further illustrated from the contact exposure map of firebrand particle contact with solid boundaries presented in Figure 6-9.

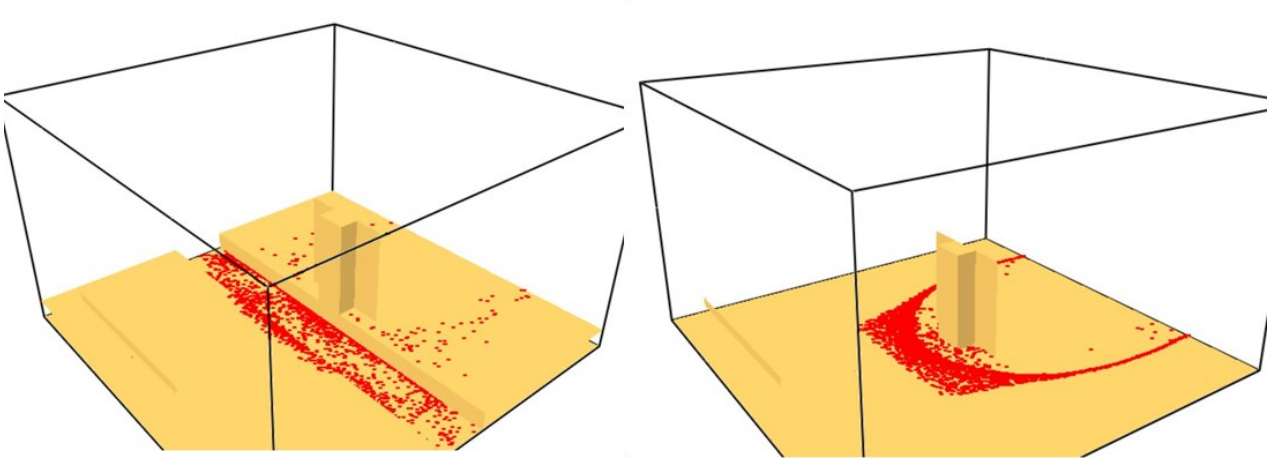

Figure 6-8: SmokeView visualisaiton of FDS simulations of firebrand exposure after 30 seconds toward a re-entrant corner (left) without a trench protection measure, and (right) with a trench protection measure.

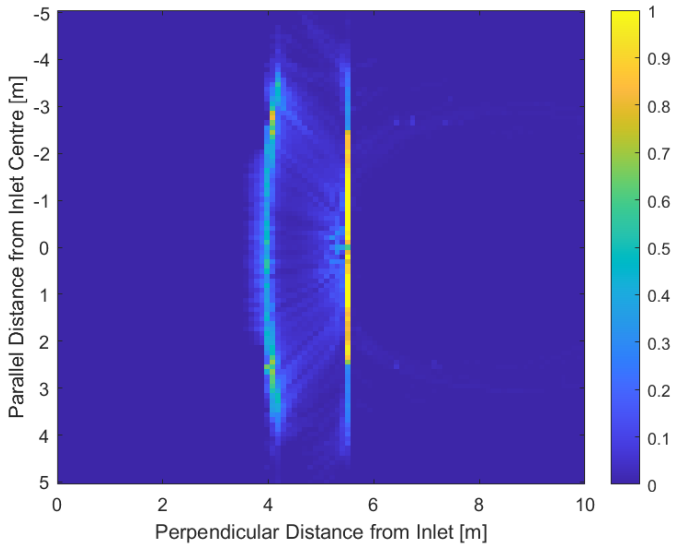

Figure 6-9 Firebrand contact exposure map showing firebrand particle position on computational domain floor around re-entrant corner geometry over 30 seconds of simulation at 8 m/s inlet wind speed with a 1.5m wide trench protection measure.

6.4 Discussion

This chapter aims to apply the conclusions and findings of the previous thesis chapter to the topic of firebrand protection measures. Firstly the existing literature on firebrand protection measures investigations and research is reviewed; the review is extended to the vast literature on protection measures safeguarding infrastructure from sand accumulation. The existing sand protection measures categorisation based on which component of the sand-infrastructure interaction the measure is applied to (sand origin, transport trajectory, or target infrastructure), are examined in terms of their applicability to wildfire exposure. Both the measures' characterisation and underlying physical principles are considered and discussed to relate the existing sand protection measures to wildfire firebrand exposure. Drawing upon the conclusions from Chapter 5, which concluded which spatial regions of the firebrand-infrastructure interaction system are most at risk under different firebrand exposure conditions, this chapter reflects on which measures can be effectively applied to firebrand exposure.

To computationally test the applicability of one a trench protection measure commonly used to inhibit sand accumulation, a simple FDS computational domain including this protection measure was tested. A trench measure operates on the transport trajectory region by altering local aerodynamic conditions at ground level, thereby preventing airborne particles from reaching and accumulating on vulnerable infrastructure. The presented computational approach presents a straightforward methodology that can be employed to implement tailored protection measures for firebrand exposure in specific design conditions. Furthermore, the same protection measure is applied to a simulation scenario investigated in Chapter 5, a re-entrant corner wall obstacle. In this simulation most of the firebrand particles introduced in the simulation remain in the trench protection created and do not reach the firebrand obstacle and leeward wake region. Comparing the simulations results with Chapter 5 results without any protection measure applied show that the majority of firebrand exposure can be controlled and limited to a pre-defined area. Notably, our investigations have revealed the promising potential of trench protection measures in safeguarding WUI structures from wildfire firebrand ignition when combined with highly fire-resistant materials or substances, such as sand or water. The most important consideration for effectively implementing this measure is choosing the most appropriate location for the specific wind conditions and obstacle materials and arrangement.

The contribution of this study to the state of the art in WUI building protection to wildfire exposure is the noted applicability of working principles of sand infrastructure protection measure to firebrand exposure protection. Modifying the aerodynamic conditions of possible target fuel can limit and modify the firebrand accumulation, and subsequently firebrand ignition, propensity. It is therefore possible to apply successful sand protection measures acting on the trajectory location, and target fuel infrastructure components to WUI vulnerabilities to firebrand ignition. Research is needed to further characterise the applicability of these existing protection measures on firebrand exposure

scenarios on a building and neighbourhood scale; this can be achieve through wind tunnel experimental studies following the methodologies already explored for firebrand exposure and accumulation investigations with the addition of protection measures (Manzello *et al.*, 2009; Quarles *et al.*, 2023). The methodology presented in this chapter can be used for exploratory and parametric computational investigation to identify the critical locations and parameters to investigate experimentally.

In summary, the insights presented in this chapter contribute to the field of fire protection engineering by elucidating the prospects of utilizing sand protection measures to mitigate wildfire firebrand ignition risks. The outcomes of this PhD study lay the groundwork for future research endeavours and serve as a catalyst for developing innovative solutions that effectively shield WUI infrastructure from firebrand exposure. By applying the knowledge and methodologies derived from this research, we can strengthen the resilience of vulnerable structures and minimize the devastating impacts of wildfire firebrand ignition.

Chapter 7 : Conclusion

7.1 Summarising Conclusions

This PhD thesis delves into the wildfire exposure and vulnerability to wildland-urban interface (WUI) buildings. The overarching research objective is to increase understanding of both the theoretical and practical aspects of wildfire exposure and damage of infrastructure, to contribute to better and more effective risk-reduction measures.

Chapter 1 starts with introducing literature that identifies the WUI fire hazard and damage context, and the WUI building components most vulnerable to wildfire ignition and damage. References investigating how each wildfire exposure mechanism: flame radiation, flame impingement and firebrand exposure, interacts with each building vulnerability are provided and commented on. The need for vulnerability building assessments and protection measures, particularly for European WUI buildings, is justified.

A statistical analysis investigating the relationship between building components and wildfire damage, is presented in chapter 2, concluding with the development of a preliminary building wildfire resistance index (WRI) validated with the 2013–2017 CAL FIRE (DINS) database from California, USA, and the 2017 Pedrógão Grande Fire Complex post-fire damage data from Portugal. Cramer's V, Bayes Factor, and Random Forest statistical dependence tests are applied and compared to evaluate the relationship between selected building features and damage. The most correlated building component to damage in the California database were the presence of vent screens and deck materials; while in Portugal the most vulnerable components were the exterior walls material and deck materials in Portugal. The research presented in this chapter is published in the International Journal of Wildland Fire (Dossi *et al.*, 2022).

The firebrand exposure processes, and their significance in causing wildfire damage are introduced in chapter 3. The chapter identifies that while firebrand deposition and accumulation processes are intimately tied to the ignition of solid obstacles, they have not been extensively studied in the literature. The physical mechanisms of particulate transport were thoroughly reviewed, drawing from the more established sand accumulation hazard field. The conclusion of this review is the need to combine firebrand exposure knowledge and wind-blown particulate transport knowledge to investigate firebrand deposition subprocesses around solid obstacles. To achieve this objective, our computational approach using FDS, a high accuracy CFD software widely employed in fire protection engineering practice and research, is introduced and justified. Overall, these initial chapters set the stage for the subsequent investigations by providing a comprehensive understanding of the vulnerabilities of WUI buildings and the importance of firebrand exposure.

Chapter 4 investigates the viability of using FDS 6.7.7 in computationally modelling firebrand creep movement and accumulation around a vertical wall obstacle. The study includes a sensitivity

analysis that quantifies the impact of particle, inlet, and ambient flow velocity on firebrand landing location. The results indicate that larger particles and higher densities tend to have a reduced influence on landing and accumulation location. This relationship is further quantified by finding the approximate linear relationship (R^2 = 70%) between the nondimensional Tachikawa number and FDS firebrand landing location. The results of FDS in 'infinite friction' mode and 'zero friction' mode, two possible modalities that need to be specified in the FDS Lagrangian model, are compared and commented on. Comparisons of both modalities simulated results to experimental results highlight limitations of the FDS model and useful similarities. The FDS 'infinite friction' mode shows the most significant agreement in terms of the simulated variation in accumulated area size with wind speed, although it tends to overestimate the accumulated area compared to the experiments. On the other hand, the FDS 'zero friction' mode exhibits an opposing trend to the experiments, and the accumulated area cannot be quantitatively compared due to the assumption of zero friction impeding steady state accumulation.

The simulations of particle contact with three different obstacles conducted in Chapter 5 illustrate the most hazardous regions for firebrand ignition around a simple wall, a step, and a re-entrant corner obstacle at 8 m/s, 10 m/s and 12 m/s ambient wind speeds. Results show how firebrands contact with solid boundaries are influenced by both the ambient wind speed and the geometry of the obstacles. At 8 m/s wind speed, the highest probability of firebrand contact occurs at the windward edge of the windward recirculation zone, with firebrands following a similar path around the solid obstacles. At 10 m/s wind speed, firebrand paths concentrate at the intersection edge between the wall obstacle and ground floor, as well as at the edges of the leeward wake flow path and windward recirculation zones. At the highest wind speed of 12 m/s, particle paths change significantly for each obstacle geometry, with firebrands concentrating in the inner corners and vertical vortices of the re-entrant corner obstacle.

The closing chapter aims to integrate previous findings and propose engineering protection measures approach to firebrand exposure; by exploring the applicability of more established and widely investigate sand protection measures. After reviewing existing literature on firebrand and sand protection measures, examining their categorization and underlying physical principles, a FDS computational testing method of a trench protection measure, commonly used to inhibit sand accumulation, is presented. This preliminary analysis demonstrates the potential of trench protection in preventing firebrand ignition when combined knowledge of firebrand behaviour under different wind speeds, and solid obstacle design. The findings contribute to fire protection engineering by providing insights into utilizing sand protection measures and lay the foundation for future research and innovative solutions to safeguard WUI infrastructure from firebrand exposure.

7.2 Future Research Needs

This research conclusions, inspire a number of research areas and questions beneficial in better understanding wildfire exposure and ignition of buildings. The identified gaps are specified with the objective supporting the development of more effective protection strategies for wildfire damage.

The statistical analysis of building damage discussed in chapter 2 inspired more detailed question in determining the detailed ignition pathways and resulting damage patterns for each building component and condition. After determining that the general condition of the identified features is statistically significant in the final damage level, more detailed questions of the processes which cause each component failure remain uncertain. Post-fire building damage data collection, with detailed accounts of the building condition and the building surrounding area can lead to more detailed recommendations on mitigating vulnerabilities to wildfire exposure. Connection to the fire regimes, and intensity of exposure can become more significant as wildfire regimes continue intensifying. The WRI methodology and concept can be applied, with relevant modifications, to more damage datasets to further validate and optimise its predictive capabilities. Machine learning methods can be applied to this methodology to consider larger datasets and more influencing parameters to increase accuracy and applicability. The WRI analysis revealed that quantitative assessments can be applied to diverse locations, both in terms of wildfire behaviour and building constructions; meaningful comparison between diverse WUI communities can be leveraged to apply knowledge across regions as communities adapt against evolving wildfire exposures.

Simulating firebrand accumulation and creep movement is introduced in this thesis. The need for experimentally measured firebrand particles creep rates and speeds for various surface roughness, and particle characteristics is identified. The large number of influencing parameters to firebrand exposure is well established in literature; and the identification of widely applied relationships between these parameters is challenging to extract. By focusing on small spatial scale, idealised and simplified scenarios relating local wind flow, firebrand characteristics and their resulting behaviour; the assumptions taken in CFD simulations of this phenomenon can be validated and their error defined, assisting computational tools to inform design decisions and vulnerability assessments.

Specifically, there is a need to conduct experimental tests to determine the kinetic friction between firebrand particles and various common building construction materials. Understanding the interaction between firebrands and building surfaces can better inform fire-resistance design and mitigation. Characterising with more detail the impact of firebrand inlet location and condition during different wildfire conditions, on firebrand landing is also necessary to better characterise firebrand ignition hazard zones on infrastructure. These investigation areas can be gradually increased in complexity, considering a number of different fuels, and firebrand burning conditions. Furthermore findings and methodologies presented in this thesis can be coupled with existing research to strengthen and optimise wildfire-resistant design decisions. The firebrand contact exposure mapping methodology can be applied to identify the likely fire sources used in proposed PBD approach for WUI

buildings (Vacca *et al.*, 2020), and to results regarding ignition conditions for construction materials (Santamaria *et al.*, 2015; Meerpoel-Pietri *et al.*, 2021), to improve the justification and reasoning of design decisions in high wildfire damage risk areas.

A promising future research area involves testing different sand protection measures and their effectiveness in protecting buildings from firebrand exposure. Such investigation could allow for a comprehensive evaluation of the effectiveness of sand as a protective measure against firebrands, and potentially lead to deployable protective tools for infrastructure. The principles of modifying aerodynamic conditions to prevent firebrand accumulation are transferable from the sand accumulation field, however more data on firebrand accumulation and creep movement processes is necessary to accurately design targeted protection measures.

In conclusion, applicable protection, prevention, and mitigation measures tailed to firebrand exposure are needed to reduce wildfire damage. Firebrand exposure has been established as the leading cause of wildfire infrastructure damage; this exposure is more complex to protect from compared to external flame exposure. Firebrands can travel as fast as the surrounding local wind speed allows, and come to contact with target fuel directly, jumping any existing fire breaks and defensible space. Increasing understanding through practical methodologies of firebrand movement, and subsequent heat exposure, around and on solid obstacles is of crucial importance to better design and protect infrastructure from this ignition hazard. Experimental and computational investigations targeted at characterising in more detail firebrand creep and accumulation movement can support more effective wildfire-resistant infrastructure designs.

7.3 Protecting Existing WUI Buildings

This section proposes practical applications of the presented thesis research findings to effectively safeguard existing WUI buildings from wildfire damage. In 2020 the WUI consisted of 15% of European land area, and is inhabited by approximately 44% of the global population worldwide (Schug *et al.*, 2023). Infrastructures at risk of intense fire exposure will increase as wildfire intensity increases; maintaining and retrofitting these constructions is a pressing safety concern. Figure 7-1 provides an illustrative representation of the suggested cycle of actions; the actions are intended as a general methodology that can be applied to diverse infrastructure. Each proposed action related to more specific methodologies and approaches either reviewed or created within particular chapter of this thesis; these are discussed below.

The first important step is to assess the building vulnerability. This thesis provides a comprehensive review of existing literature on building vulnerabilities to each wildfire exposure mechanism, and presents the preliminary Wildfire Resistance Index (WRI) which can be used to quantitatively assess building wildfire vulnerability. The relative vulnerability of buildings located in close proximity to one another is important; it is suggested to assess as many building constructions in a given WUI area as possible, and target the most vulnerable structures for the most impactful risk-

reduction results. Similarly, focusing on strengthening building components that are particularly susceptible on a given building, will target mitigation efforts most effectively as reflected in the WRI validation results.

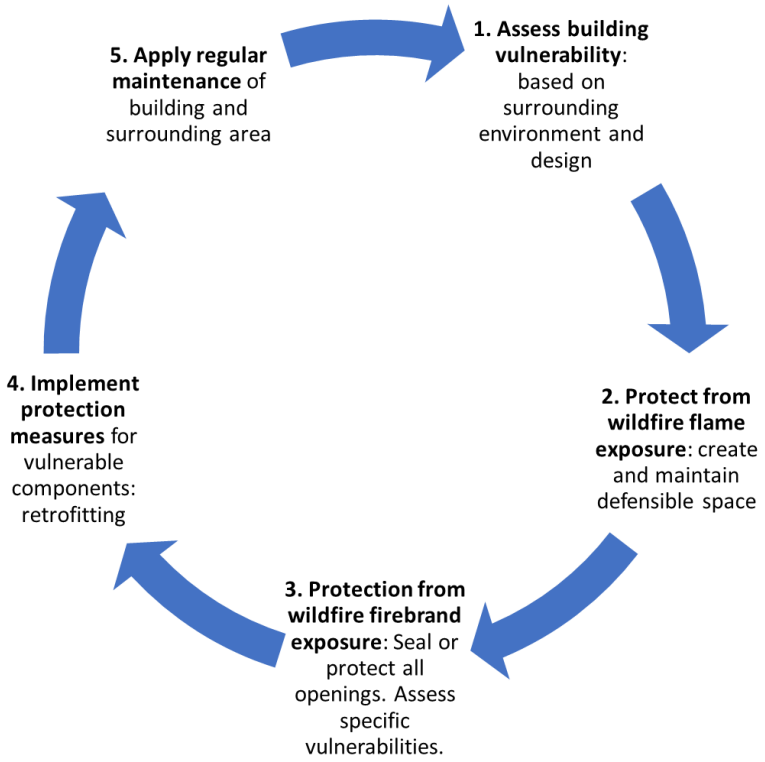

Figure 7-1: Cycle of suggested actions to reduce wildfire ignition risk of existing WUI buildings based on the research findings presented in this thesis.

Secondly, to protect from wildfire flame exposure it is important to create defensible space around the building construction. The existing practices and guidance available in literature and community risk reduction programs are referenced in the literature review of this thesis and authors suggest to prioritise defensible space in the immediate vicinity of the most vulnerable building components and buildings identified in step 1.

The majority of the presented thesis focuses on deepening understanding of wildfire firebrand exposure, specifically firebrand creep movement and accumulation. Mitigating firebrand exposure is crucial; the literature review presented revealed that firebrands have caused up to 90% of building ignitions in past wildfire events (Potter and Leonard, 2010). Direct firebrand ignition can occur through firebrands entering the building 1and igniting inside fuel, or by landing, accumulating on, and igniting external components. Indirect firebrand ignition occurs when firebrands ignite the fuel surrounding the building, which can in turn cause flame exposure on the building structure. Established firebrand ignition risk reduction actions include sealing all possible openings in the building external envelope and reinforcing vulnerable building components. This research presented in this thesis quantifies the firebrand paths that are most likely to occur around selected building

component geometries under various ambient wind conditions. Vertical re-entrant corners are shown to favour firebrand contact and should therefore be protected and strengthened as much as possible. Under high wind speeds the intersection of steps are also shown to favour firebrand contact exposure. Avoiding combustible materials in building components with such configurations is recommended.

The succeeding suggested hazard mitigation step relates to implementing building protection measures. At the moment, available firebrand protection include installing vent mesh screens, to protect firebrand penetration; and maintaining defensible space, to prevent indirect firebrand ignition. In this thesis, the existing firebrand protection measures, and recent research on this topic, are presented and discussed. Furthermore, this research explores the applicability of established sand protection measures for WUI firebrand protection. More advanced and effective protection measures, especially targeting direct firebrand ignition of external building components, are needed. Regular maintenance is of outmost importance in wildfire infrastructure protection; this is confirmed in the presented statistical analysis results regarding 'building preservation level' as statistically significantly correlated to wildfire building damage. All the cited risk-reduction measures require consistent maintenance for successful results.

This cyclical approach combining vulnerability assessment, wildfire flame and firebrand exposure protection, and regular maintenance, is proposed as a framework to protect existing buildings from wildfires; detailed methodologies and references to apply each step are provided in this thesis.

7.4 Designing Wildfire-Safe WUI Buildings

WUI areas are expanding in worldwide; urbanisation expansion near and inside forests has been documented in the USA, Europe, Canada, Chile, and Argentina (Godoy *et al.*, 2022). In central Patagonia, Argentina the WUI increased 76% in area and 74% in number of houses between 1981 and 2016 (Defossé, 2023). An increasing number of buildings will be built in areas with possibility of high wildfire occurrence and exposure. Consequently, there is a growing need to design and construct buildings able to withstand this hazard. This thesis contributes valuable insights that can be included in design procedures and couple with existing assessment methodologies to design constructions with higher resistance to wildfire exposure. Moreover, insurance companies can utilize the knowledge and tools presented to assess infrastructure vulnerability more accurately and assist and inform residents appropriately; this all contributes to strengthen the resilience of communities (including buildings, people, and institutional procedures) to wildfire exposure and damage.

Figure 7-2 illustrates four general steps that are recommended to be considered and followed during the design process of WUI infrastructure; the steps relate to information and methodologies presented in this thesis. Careful consideration must be given to the design of the building components defined as most vulnerable to wildfire ignition in this thesis. Assessing the vulnerability of a proposed building design in detail, considering all component design, materials, and surrounding environment

is a crucial step in the design process of WUI constructions. Chapter 1 and 2 of this thesis provide the background and a simple quantitative assessment methodology which can be applied as a first preliminary vulnerability analysis. New constructions should consider changing wildfire regimes, any novel or untested building material used, and predict the necessary maintenance required to maintain the preservation of the designed building.

Figure 7-2: Sequence of suggested general actions to reduce wildfire ignition risk when designing new WUI buildings based on findings presented in this thesis.

Once the vulnerability is assessed and considered fully, the high ignition risk components and areas around the building structure can be tested for potential flame and firebrand exposure. This is where PBD methodologies and the methodologies presented in chapter 4 mapping the firebrand contact exposure can be applied to quantitatively justify the design decisions in terms of arrangement and building materials for the selected components. The research presented offers methodologies regarding using FDS, extendable to other CFD software, to identify the most hazardous zones for firebrand exposure and ignition around specific obstacles. Once these areas are identified, appropriate fire-resistant materials and protective measures can be applied. These methodologies provide the opportunity of a simple framework which can quantify prospective wildfire exposure, and quantify the predicted resulting heat flux on the structure, and specifically test the response behaviour

of commercial components and materials to justified exposure scenarios. Chapter 6 explores the protection measures which have been designed and applied to protect infrastructure from sand accumulation; construction companies building and expanding the WUI areas have the responsibility to test and explore possible protection measures to protect residents and economic investments. Although the field of protection measures against firebrand exposure is still unmature, investment in innovative protection measures can assist in justifying WUI building designs.

The preservation level of a building, which results from regular maintenance of the external building structure and its surroundings, plays a crucial role determining wildfire vulnerability. To this end, in the designing, insuring, and selling new constructions, all relevant stakeholders (including all companies involved in construction supply chain, residents, fire emergency response agencies and local government) need to be educated about vulnerabilities and informed on how to maintain and improve the building's safety to wildfire threats. This process can also be inherently facilitated in the building design by including appropriate design features: for example: fire resistant patios or decks which mark a defensible space area, by ensuring roof gutters can be easily cleaned or protected from accumulated debris, by creating, testing, and including target fuel protection measures such as screens and barriers to prevent firebrand accumulation. The final suggested action is therefore to collect the investigations and considerations made during the design process, and provide them clearly to the relevant stakeholders to facilitate and enable collaborative and continuous risk reduction.

This thesis provides valuable insights and novel methodologies applicable in the designing buildings that can better withstand the increasing intensity of wildfire exposure threats. Regulating and standardising WUI building design procedures which consider wildfire exposure resistance from the beginning of the construction process can assist expanding WUI areas in considering and adapting to increasing wildfire exposure.

References

Albini, F.A. (1979) *Spot Fire Distance from Burning Trees: A Predictive Model*. Edited by U. Intermountain Forest and Range Experiment Station (Ogden. USDA, Forest Service (General technical report INT).

Albini, F.A. (1981) 'Spot fire distance from isolated sources - extensions of a predictive model', *USDA Forest Service Research Note*, INT-309, p. 9p.

Albini, F.A. (1983) 'Transport of firebrands by line thermalst', *Combustion Science and Technology*, 32(5–6), pp. 277–288. doi:10.1080/00102208308923662.

Andersen, L.M. and Sugg, M.M. (2019) 'Geographic multi-criteria evaluation and validation: A case study of wildfire vulnerability in Western North Carolina, USA following the 2016 wildfires', *International Journal of Disaster Risk Reduction*, 39. doi:10.1016/j.ijdrr.2019.101123.

Anderson, J.D. (1995) *Computational Fluid Dynamics*. New York: McGraw-Hill Inc.

Anthenien, R.A., Tse, S.D. and Carlos Fernandez-Pello, A. (2006) 'On the trajectories of embers initially elevated or lofted by small scale ground fire plumes in high winds', *Fire Safety Journal*, 41(5), pp. 349–363. doi:10.1016/j.firesaf.2006.01.005.

Babrauskas, V. (2003) 'Ignition Sources', in *Ignition Handbook*, pp. 497–590.

Babrauskas, V. (2018) 'Firebrands and Embers', in Manzello, S.L. (ed.) *Encyclopedia of Wildfires and Wildland-Urban Interface (WUI) Fires*. Cham: Springer International Publishing, pp. 1–14. doi:10.1007/978-3-319-51727-8_3-1.

Bagnold, R.A. (1974) *The Physics of Blown Sand and Desert Dunes*. Springer Dordrecht. doi:https://doi.org/10.1007/978-94-009-5682-7.

Barr, B.W. and Ezekoye, O.A. (2013) 'Thermo-mechanical modeling of firebrand

breakage on a fractal tree', *Proceedings of the Combustion Institute*, 34(2), pp. 2649–2656. doi:10.1016/j.proci.2012.07.066.

Belly, P.Y. (1964) *Sand movement by wind, technical report*.

Billmire, M., French, N.H.F., Loboda, T., Owen, R.C. and Tyner, M. (2014) 'Santa Ana winds and predictors of wildfire progression in southern California', *International Journal of Wildland Fire*, 23(8), pp. 1119–1129. doi:10.1071/WF13046.

Biswas, K., Werth, D. and Gupta, N. (2013) 'A home ignition assessment model applied to structures in the wildland-urban interface', *Thermal Performance of the Exterior Envelopes of Whole Buildings XII International Conference* [Preprint].

Blanchi, R., Leonard, J.E. and Leicester, R.H. (2006) 'Lessons learnt from post-bushfire surveys at the urban interface in Australia', *Forest Ecology and Management*, 234. doi:10.1016/j.foreco.2006.08.184.

Boboulos, M. and Purvis, M.R.I. (2009) 'Wind and slope effects on ROS during the fire propagation in East-Mediterranean pine forest litter', *Fire Safety Journal*, 44(5), pp. 764–769. doi:10.1016/j.firesaf.2009.03.006.

Bruno, L., Horvat, M. and Raffaele, L. (2018) 'Windblown sand along railway infrastructures: A review of challenges and mitigation measures', *Journal of Wind Engineering and Industrial Aerodynamics*, 177(April), pp. 340–365. doi:10.1016/j.jweia.2018.04.021.

Butler, C.P. (1974) 'The Urban/Wildland Fire Interface', *Proceedings of Western Stattes Section/Combustion Institute Papers*, 74(15), pp. 1–17.

Cantor, P., Arruda, M.R.T., Firmo, J. and Branco, F. (2023) 'Development of a standard firebrand accumulation temperature curve for residential wildfire protection system', *Results in Engineering*, 17(February), p. 100935. doi:10.1016/j.rineng.2023.100935.

Caton, S.E., Hakes, R.S.P., Gorham, D.J., Zhou, A. and Gollner, M.J. (2017)

‘Review of Pathways for Building Fire Spread in the Wildland Urban Interface Part I: Exposure Conditions’, *Fire Technology*, 53(2), pp. 429–473. doi:10.1007/s10694-016-0589-z.

Chappaz, F. and Ganteaume, A. (2022) ‘Role of land-cover and WUI types on spatio-temporal dynamics of fires in the French Mediterranean area’, *Risk Analysis*, pp. 1032–1057. doi:10.1111/risa.13979.

Cheng, J. jun and Xue, C. xiao (2014) ‘The sand-damage-prevention engineering system for the railway in the desert region of the Qinghai-Tibet plateau’, *Journal of Wind Engineering and Industrial Aerodynamics*, 125, pp. 30–37. doi:10.1016/j.jweia.2013.11.016.

Chhabra, R.P., Agarwal, L. and Sinha, N.K. (1999) ‘Drag on non-spherical particles: An evaluation of available methods’, *Powder Technology*, 101(3), pp. 288–295. doi:10.1016/S0032-5910(98)00178-8.

Cohen, J. (1988) *Statistical Power Analysis for the Behavioral Sciences*. 2nd edn. New York: Lawrence Erlbaum Associates, Publishers. doi:https://doi.org/10.4324/9780203771587.

Cohen, J. and Butler, B. (1996) ‘Modeling potential structure ignitions from flame radiation exposure with implications for wildland/urban interface fire management’, *Thirteenth Fire and Forest Meteorology …*, pp. 81–87.

Cohen, J.D. (2000) ‘Preventing disaster: Home ignitability in the wildland-urban interface’, *Journal of Forestry*, 98(3), pp. 15–21.

Cohen, J.D. (2004) ‘Relating flame radiation to home ignition using modeling and experimental crown fires’, *Canadian Journal of Forest Research*, 34(8). doi:https://doi.org/10.1139/x04-049.

Cohen, J.D. (2008) ‘The wildland-urban interface fire problem: a consequence of the fire exclusion paradigm.’, *Forest History Today*, 2008, pp. 20–26.

Defossé, G.E. (2023) 'Editorial: Fires in the wildland urban interface: An emerging global phenomenon threatening modern society', *Frontiers in Forest and Global Change*, 6. doi:doi: 10.3389/ffgc.2023.1137014 COPYRIGHT.

Dong, Z., Luo, W., Qian, G. and Wang, H. (2007) 'A wind tunnel simulation of the mean velocity fields behind upright porous fences', *Agricultural and Forest Meteorology*, 146(1–2), pp. 82–93. doi:10.1016/j.agrformet.2007.05.009.

Dossi, S., Messerschmidt, B., Ribeiro, L.M., Almeida, M. and Rein, G. (2022) 'Relationships between building features and wildfire damage in California, USA and Pedrógão Grande, Portugal', *International Journal of Wildland Fire*, 32(2), pp. 296–312. doi:10.1071/wf22095.

Escadafal, R., Bernoux, M., Bonnet, B., Cornet, A., *et al.* (2011) 'The African Great Green Wall project. What advice can scientists provide?', *Comité Scientifique Français de la Désertification (CSFD) Topical issue - The African Great Green Wall project*, (October), p. 41. Available at: www.csf-desertification.org/grande-muraille-verte.

Filkov, A., Prohanov, S., Mueller, E., Kasymov, D., *et al.* (2017) 'Investigation of firebrand production during prescribed fires conducted in a pine forest', *Proceedings of the Combustion Institute*, 36(2), pp. 3263–3270. doi:10.1016/j.proci.2016.06.125.

Finney, M.A., Cohen, J.D., Forthofer, J.M., McAllister, S.S., *et al.* (2015) 'Role of buoyant flame dynamics in wildfire spread', *Proceedings of the National Academy of Sciences of the United States of America*, 112(32), pp. 9833–9838. doi:10.1073/pnas.1504498112.

Fire Illustration (2023).

Galiana-Martin, L., Herrero, G. and Solana, J. (2011) 'A wildland-urban interface typology for forest fire risk management in mediterranean areas', *Landscape Research*, 36(2), pp. 151–171. doi:10.1080/01426397.2010.549218.

Gillies, J.A. and Lancaster, N. (2013) 'Large roughness element effects on sand

transport, Oceano Dunes, California', *Earth Surface Processes and Landforms*, 38(8), pp. 785–792. doi:10.1002/esp.3317.

Gillies, J.A., Nickling, W.G. and King, J. (2006) 'Aeolian sediment transport through large patches of roughness in the atmospheric inertial sublayer', *Journal of Geophysical Research: Earth Surface*, 111(2), pp. 1–13. doi:10.1029/2005JF000434.

Giudice, A. Lo, Nuca, R., Preziosi, L. and Coste, N. (2019) 'Wind-blown particulate transport: A review of computational fluid dynamics models', *Mathematics In Engineering*, 1(3), pp. 508–547. doi:10.3934/mine.2019.3.508.

Godoy, M.M., Martinuzzi, S., Masera, P. and Defossé, G.E. (2022) 'Forty Years of Wildland Urban Interface Growth and Its Relation With Wildfires in Central-Western Chubut, Argentina', *Frontiers in Forests and Global Change*, 5(June), pp. 1–15. doi:10.3389/ffgc.2022.850543.

Graham, R., Finney, M., McHugh, C., Cohen, J., *et al.* (2012) *Fourmile canyon fire findings*, *USDA Forest Service - General Technical Report RMRS-GTR*.

Guangyong, L. and Peng, M. (2012) 'Wind-preventing sand-throwing wall'.

Gunel, E. and Dickey, J. (1974) 'Bayes Factors for Independence in Contingency Tables', *Biometrika*, 61(3), pp. 545–557. Available at: https://www.jstor.org/stable/2334738.

Hadden, R.M., Scott, S., Lautenberger, C. and Fernandez-Pello, C.C. (2011) 'Ignition of Combustible Fuel Beds by Hot Particles: An Experimental and Theoretical Study', *Fire Technology*, 47(2), pp. 341–355. doi:10.1007/s10694-010-0181-x.

Haider, A. and Levenspiel, O. (1989) 'Drag Coefficient and Terminal Velocity of Spherical and Nonspherical Particles', *Powder Technology*, 58, pp. 63–70.

Hakes, R.S.P., Caton, S.E., Gorham, D.J. and Gollner, M.J. (2017) 'A Review of Pathways for Building Fire Spread in the Wildland Urban Interface Part II: Response of Components and Systems and Mitigation Strategies in the United States', *Fire*

Technology, 53(2), pp. 475–515. doi:10.1007/s10694-016-0601-7.

Hashempour, J. and Sharifian, A. (2017) 'Effective factors on the performance of woven wire screens against leaf firebrand attacks', *Journal of Fire Sciences*, 35(4), pp. 303–316. doi:10.1177/0734904117709203.

Hedayati, F., Bahrani, B., Zhou, A., Quarles, S.L. and Gorham, D.J. (2019) 'A Framework to Facilitate Firebrand Characterization', *Frontiers in Mechanical Engineering*, 5(July), pp. 1–14. doi:10.3389/fmech.2019.00043.

Henning, A., Cox, J. and Shew, D. (2016) *CAL FIRE's Damage Inspection Program - Its Evolution and Implementation*, *NFPA Conference & Expo*. Available at: http://www.fltwood.com/perm/nfpa-2016/scripts/sessions/M26.html (Accessed: 25 January 2022).

Himoto, K. and Hayashi, Y. (2022) 'Hierarchical Bayesian approach to developing probabilistic models for generation and transport of firebrands in large outdoor fires under limited data availability', *Fire Safety Journal*, 134(September), p. 103679. doi:10.1016/j.firesaf.2022.103679.

Himoto, K. and Tanaka, T. (2005) 'Transport of disk-shaped firebrands in a turbulent boundary layer', *Fire Safety Science*, pp. 433–444. doi:10.3801/IAFSS.FSS.8-433.

Hong, S.W., Lee, I.B. and Seo, I.H. (2015) 'Modelling and predicting wind velocity patterns for windbreak fence design', *Journal of Wind Engineering and Industrial Aerodynamics*, 142, pp. 53–64. doi:10.1016/j.jweia.2015.03.007.

Hotta, S. and Horikawa, K. (1990) 'Function of Sand Fence Placed in Front of Embankment', in *Coastal Engineering*, pp. 2754–2767. doi:https://doi.org/10.1061/9780872627765.211.

Hudson, T.R., Bray, R.B., Blunck, D.L., Page, W. and Butler, B. (2020) 'Effects of fuel morphology on ember generation characteristics at the tree scale', *International Journal of Wildland Fire*, 29(11), pp. 1042–1051. doi:10.1071/WF19182.

Hughes, M. and Hall, A. (2010) 'Local and synoptic mechanisms causing Southern California's Santa Ana winds', *Climate Dynamics*, 34(6), pp. 847–857. doi:10.1007/s00382-009-0650-4.

Hysa, A. (2021) 'Indexing the vegetated surfaces within WUI by their wildfire ignition and spreading capacity, a comparative case from developing metropolitan areas', *International Journal of Disaster Risk Reduction*, 63. doi:10.1016/j.ijdrr.2021.102434.

IBHS (2021) *Suburban Wildfire Adaptation Roadmaps*. Available at: https://ibhs.org/wp-content/uploads/ibhs-wildfire-roadmaps_executive-summary.pdf.

IBHS (2022) *Wildfire Prepared*. Available at: https://wildfireprepared.org/ (Accessed: 30 October 2022).

Intini, P., Ronchi, E., Gwynne, S. and Bénichou, N. (2020) *Guidance on Design and Construction of the Built Environment Against Wildland Urban Interface Fire Hazard: A Review*, *Fire Technology*. doi:10.1007/s10694-019-00902-z.

Kadel, J., Hedayati, F., Quarles, S.L. and Zhou, A. (2021) 'Effect of Environmental Conditions on the Dehydration and Performance of Fire-Protective Gels', *Fire Technology*, 57(3), pp. 1241–1257. doi:10.1007/s10694-020-01045-2.

Kimiko, B. (2022) *Wood roofs are a $6 billion wildfire problem*. Available at: https://headwaterseconomics.org/natural-hazards/wood-roofs-wildfire/ (Accessed: 5 September 2022).

Klassen, M.S., Sutula, J.A., Holton, M.M. and Roby, R.J. (2010) 'Transmission Through and Breakage of Single and Multi-Pane Glazing Due to Radiant Exposure: State of Research', *Fire Technology*, 46(4), pp. 821–832. doi:10.1007/s10694-010-0150-4.

Knapp, E.E., Valachovic, Y.S., Quarles, S.L. and Johnson, N.G. (2021) 'Housing arrangement and vegetation factors associated with single-family home survival in the

2018 Camp Fire, California', *Fire Ecology*, 17(1). doi:10.1186/s42408-021-00117-0.

Kok, J.F. (2010) 'Analytical calculation of the minimum wind speed required to sustain wind-blown sand on Earth and Mars', *arXiv preprint arXiv:1001.4840* [Preprint].

Kok, J.F., Parteli, E.J.R., Michaels, T.I. and Karam, D.B. (2012) 'The physics of wind-blown sand and dust', *Reports on Progress in Physics*, 75(10), pp. 1–119. doi:10.1088/0034-4885/75/10/106901.

Koo, E., Linn, R.R., Pagni, P.J. and Edminster, C.B. (2012) 'Modelling firebrand transport in wildfires using HIGRAD/FIRETEC', *International Journal of Wildland Fire*, 21(4), pp. 396–417. doi:10.1071/WF09146.

Koo, E., Pagni, P.J., Weise, D.R. and Woycheese, J.P. (2010) 'Firebrands and spotting ignition in large-scale fires', *International Journal of Wildland Fire*, 19(7), pp. 818–843. doi:10.1071/WF07119.

Kursa, M.B. and Rudnicki, W.R. (2010) 'Feature selection with the boruta package', *Journal of Statistical Software*, 36(11), pp. 1–13. doi:10.18637/jss.v036.i11.

Kwon, B. and Liao, Y.T.T. (2022) 'Effects of spacing on flaming and smoldering firebrands in wildland–urban interface fires', *Journal of Fire Sciences*, 40(3), pp. 155–174. doi:10.1177/07349041221081998.

Lee, M.D. and Wagenmakers, E.J. (2014) *Bayesian Cognitive Modeling: A Practical Course*. Cambridge University Press. Available at: https://books.google.co.uk/books?id=50tkAgAAQBAJ.

Lee, S.L. and Hellman, J.M. (1970) 'Firebrand trajectory study using an empirical velocity-dependent burning law', *Combustion and Flame*, 15(3), pp. 265–274. doi:10.1016/0010-2180(70)90006-4.

Liu, D.L. (2009) 'Particle Deposition onto Enclosure Surfaces', *Developments in Surface Contamination and Cleaning*, pp. 1–56. doi:10.1016/B978-1-4377-7830-

4.10001-5.

Mankame, A. and Shotorban, B. (2021) 'Deposition Characteristics of Firebrands on and Around Rectangular Cubic Structures', *Frontiers in Mechanical Engineering*, 7, pp. 1–14. doi:10.3389/fmech.2021.640979.

Manzello, S.L. (2013) *The Performance of Concrete Tile and Terracotta Tile Roofing Assemblies Exposed to Wind-Driven Firebrand Showers*. doi:http://dx.doi.org/10.6028/NIST.TN.1794.

Manzello, S.L., Blanchi, R., Gollner, M.J., Gorham, D., *et al.* (2018) 'Summary of workshop large outdoor fires and the built environment', *Fire Safety Journal*, 100, pp. 76–92. doi:10.1016/j.firesaf.2018.07.002.

Manzello, S.L. and Foote, E.I.D. (2014) 'Characterizing Firebrand Exposure from Wildland-Urban Interface (WUI) Fires: Results from the 2007 Angora Fire', *Fire Technology*, 50(1), pp. 105–124. doi:10.1007/s10694-012-0295-4.

Manzello, S.L., Hayashi, Y., Yoneki, T. and Yamamoto, Y. (2010) 'Quantifying the vulnerabilities of ceramic tile roofing assemblies to ignition during a firebrand attack', *Fire Safety Journal*, 45(1), pp. 35–43. doi:10.1016/j.firesaf.2009.09.002.

Manzello, S.L., Park, S.-H., Shields, J.R., Hayashi, Y. and Suzuki, S. (2010) *Comparison Testing Protocol for Firebrand Penetration through Building Vents : Summary of BRI / NIST Full Scale and NIST Reduced Scale Results*. Gaithersburg, MD.

Manzello, S.L., Shields, J.R., Hayashi, Y. and Nii, D. (2009) 'Investigating the vulnerabilities of structures to ignition from a firebrand attack', *Fire Safety Science*, 9, pp. 143–154. doi:10.3801/IAFSS.FSS.9-143.

Manzello, S.L. and Suzuki, S. (2013) 'Experimentally simulating wind driven firebrand showers in wildland-urban interface (WUI) fires: Overview of the NIST firebrand generator (NIST dragon) technology', *Procedia Engineering*, 62, pp. 91–102. doi:10.1016/j.proeng.2013.08.047.

Manzello, S.L. and Suzuki, S. (2014) 'Exposing decking assemblies to continuous wind-driven firebrand showers', *Fire Safety Science*, 11, pp. 1339–1352. doi:10.3801/IAFSS.FSS.11-1339.

Manzello, S.L., Suzuki, S., Gollner, M.J. and Fernandez-Pello, A.C. (2020) 'Role of firebrand combustion in large outdoor fire spread', *Progress in Energy and Combustion Science*, 76, p. 100801. doi:10.1016/j.pecs.2019.100801.

Manzello, S.L., Suzuki, S. and Hayashi, Y. (2012) 'Exposing siding treatments, walls fitted with eaves, and glazing assemblies to firebrand showers', *Fire Safety Journal*, 50, pp. 25–34. doi:10.1016/j.firesaf.2012.01.006.

Manzello, S.L., Suzuki, S. and Naruse, T. (2019) 'Quantifying wind-driven firebrand production from roofing assembly combustion', *Fire and Materials*, 43(1), pp. 3–7. doi:10.1002/fam.2661.

Maranghides, A. and Johnsson, E. (2008) *NIST Technical Note 1600 Residential Structure Separation Fire Experiments*.

Maranghides, A., Link, E., Mell, W.R., Maranghides, A., Nazare, S. and Link, E. (2022) *NIST Outdoor Structure Separation Experiments (NOSSE): Preliminary Test Plan*. doi:https://doi.org/10.6028/NIST.TN.2199.

Maranghides, A. and Mell, W. (2012) *Framework for Addressing the National Wildland Urban Interface Fire Problem- Determining Fire and Ember Exposure Zones using a WUI Hazard Scale*. NIST Technical Note 1748.

McArthur, A.G. (1967) *Fire behaviour in eucalypt forests*. Canberra: Forestry and Timber Bureau.

McGrattan, K. and Miles, S. (2016) 'Modeling Fires Using Computational Fluid Dynamics (CFD)', in *SFPE Handbook of Fire Protection Engineering*. Fifth. New York: Springer.

McGrattan, K.B., Baum, H.R., Rehm, R.G., Hamins, A. and Forney, G.P. (2021)

'Fire Dynamics Simulator - Technical Reference Manual', *NIST Special Publication 1018-1. US Department of Commerce, National Institute of Standards and Technology. Gaithersburg, MD.*, 1(5), p. 175.

McLaughlin, W.T. (1942) *Controlling coastal sand dunes in the Pacific Northwest*.

Meerpoel-Pietri, K., Tihay-Felicelli, V. and Santoni, P.A. (2021) 'Determination of the critical conditions leading to the ignition of decking slabs by flaming firebrands', *Fire Safety Journal*, 120. doi:10.1016/j.firesaf.2020.103017.

Meier, S., Elliott, R.J.R. and Strobl, E. (2023) 'The regional economic impact of wildfires: Evidence from Southern Europe', *Journal of Environmental Economics and Management*, 118(May 2022), p. 102787. doi:10.1016/j.jeem.2023.102787.

Mell, W.E., Manzello, S.L., Maranghides, A., Butry, D. and Rehm, R.G. (2010) 'The Wildland – Urban Interface Fire Problem – Current Approaches and Research Needs', *International Journal Of Wildland Fire*, 2005, pp. 238–251.

Mendes, P.J.N.F. (2013) *A influência do RCCTE na Arquitetura e as Perspetivas para o Futuro*. Universidade do Minho. Available at: https://hdl.handle.net/1822/27624.

Moinuddin, K. and Wadhwani, R. (2019) 'Simulated 6th International Fire Behavior and transport of short-range embers in an idealised bushfire', (May).

Moritz, M.A., Batllori, E., Bradstock, R.A., Gill, A.M., *et al.* (2014) 'Learning to coexist with wildfire', *Nature*, 515(7525), pp. 58–66. doi:10.1038/nature13946.

Muraszew, A., Fedele, J.B. and Kuby, W.C. (1977) 'Trajectory of firebrands in and out of fire whirls', *Combustion and Flame*, 30(C), pp. 321–324. doi:10.1016/0010-2180(77)90081-5.

National Fire Protection Association (2022) *FireWise USA*. Available at: https://www.nfpa.org/Public-Education/Fire-causes-and-risks/Wildfire/Firewise-

USA (Accessed: 17 September 2022).

NFPA 1140 (2022) *NFPA 1140 Standard for Wildland Fire Protection*. Available at: https://www.nfpa.org/codes-and-standards.

Nguyen, D. and Kaye, N.B. (2021) 'Experimental investigation of rooftop hotspots during wildfire ember storms', *Fire Safety Journal*, 125. doi:10.1016/j.firesaf.2021.103445.

Nguyen, D. and Kaye, N.B. (2022a) 'Quantification of ember accumulation on the rooftops of isolated buildings in an ember storm', *Fire Safety Journal*, 128(103525). doi:10.1016/j.firesaf.2022.103525.

Nguyen, D. and Kaye, N.B. (2022b) 'The role of surrounding buildings on the accumulation of embers on rooftops during an ember storm', *Fire Safety Journal*, 131(103624). doi:10.1016/j.firesaf.2022.103624.

Oke, T.R. (1987) *Boundary Layer Climates*. 2nd edn. Routledge. doi:https://doi.org/10.4324/9780203407219.

Orloff, L., De Ris, J. and Markstein, G.H. (1975) 'Upward turbulent fire spread and burning of fuel surface', *Symposium (International) on Combustion*, 15(1), pp. 183–192. doi:10.1016/S0082-0784(75)80296-7.

Pampaka, M., Hutcheson, G. and Williams, J. (2016) 'Handling missing data: analysis of a challenging data set using multiple imputation', *International Journal of Research and Method in Education*, 39(1), pp. 19–37. doi:10.1080/1743727X.2014.979146.

Papakosta, P., Xanthopoulos, G. and Straub, D. (2017) 'Probabilistic prediction of wildfire economic losses to housing in Cyprus using Bayesian network analysis', *International Journal of Wildland Fire*, 26(1), pp. 10–23. doi:10.1071/WF15113.

Papathoma-Köhle, M., Schlögl, M., Garlichs, C., Diakakis, M., Mavroulis, S. and Fuchs, S. (2022) 'A wildfire vulnerability index for buildings', *Scientific Reports*

Nature, 12(1), pp. 1–15. doi:10.1038/s41598-022-10479-3.

Piomelli, U. (2014) 'Large eddy simulations in 2030 and beyond', *Philosophical Transactions of the Royal Society*, 372(2022). doi:10.1098/rsta.2013.0320.

Potter, M. and Leonard, J. (2010) 'Spray System Design for Ember Attack - Research Findings and Discussion Paper', (D), p. 30.

Pyne, S.J. (1949) *Vestal Fire: An Environmental History, Told through Fire, of Europe and Europe's Encounter with the World*. Seattle and London: University of Washington Press.

Quarles, S. and Standohar-Alfano, C. (2018) *Ignition Potential of Decks Subjected to an Ember Exposure*. Available at: http://disastersafety.org/wp-content/uploads/2017/10/Deck-Ember-Testing-Report-2017_IBHS.pdf.

Quarles, S.L. and Sindelar, M. (2011) *Wildfire Ignition Resistant Home Design (WIRHD) Program: Full-scale Testing and Demonstration Final Report*. Available at: https://www.osti.gov/servlets/purl/1032503.

Quarles, S.L., Standohar-Alfano, C., Hedayati, F. and Gorham, D.J. (2023) 'Factors influencing ember accumulation near a building', *International Journal of Wildland Fire*, pp. 1–8. doi:10.1071/wf22132.

Quarles, S.L., Valachovic, Y., Nakamura, G.M., Nader, G.A. and de Lasaux, M.J. (2010) 'Home Survival in Wildfire-Prone Areas: Building Materials and Design Considerations', *Home Survival in Wildfire-Prone Areas: Building Materials and Design Considerations*, pp. 1–22. doi:10.3733/ucanr.8393.

Radeloff, V.C., Helmers, D.P., Anu Kramer, H., Mockrin, M.H., *et al.* (2018) 'Rapid growth of the US wildland-urban interface raises wildfire risk', *Proceedings of the National Academy of Sciences of the United States of America*, 115(13), pp. 3314–3319. doi:10.1073/pnas.1718850115.

Raffaele, L., Bruno, L., Pellerey, F. and Preziosi, L. (2016) 'Windblown sand

saltation: A statistical approach to fluid threshold shear velocity', *Aeolian Research*, 23, pp. 79–91. doi:10.1016/j.aeolia.2016.10.002.

Ragland, K.W., Aerts, D.J. and Baker, A.J. (1991) 'Properties of wood for combustion analysis', *Bioresource Technology*, 37(2), pp. 161–168. doi:10.1016/0960-8524(91)90205-X.

Rahim, M. (1945) 'Behaviour of Drift Sand and Method of Dealing with it', *Pakistan Engineering Congress* [Preprint].

Randerson, D. (1978) 'Atmospheric Boundary Layer.', *US Department of Energy, Technical Information Center, (Technical Report) DOE/TIC*, 37, pp. 147–188. doi:10.1201/9781439847121-c2.

Rea, L. and Parker, R. (1962) *Designing and Conducting Survey Research: A Comprehensive Guide*. San Francisco: Jossey-Bass Publishers.

Ribeiro, L.M., Rodrigues, A., Lucas, D. and Viegas, D.X. (2020) 'The impact on structures of the pedrógão grande fire complex in June 2017 (Portugal)', *Fire*, 3(4), pp. 1–22. doi:10.3390/fire3040057.

Rouder, J.N., Speckman, P.L., Sun, D., Morey, R.D. and Iverson, G. (2009) 'Bayesian t tests for accepting and rejecting the null hypothesis', *Psychonomic Bulletin and Review*, 16(2), pp. 225–237. doi:10.3758/PBR.16.2.225.

Samora-Arvela, A., Aranha, J., Correia, F., Pinto, D.M., Magalhães, C. and Tedim, F. (2023) 'Understanding Building Resistance to Wildfires: A Multi-Factor Approach', *Fire*, 6(1), pp. 1–15. doi:10.3390/fire6010032.

San-Miguel-Ayanz, J., Moreno, J.M. and Camia, A. (2013) 'Analysis of large fires in European Mediterranean landscapes: Lessons learned and perspectives', *Forest Ecology and Management*, 294, pp. 11–22. doi:10.1016/j.foreco.2012.10.050.

San-Miguel-Ayanz, J., Oom, D., Artès, T., Viegas, D.X., *et al.* (2021) 'Forest fires in Portugal in 2017', *Science for Disaster Risk Management 2020: acting today,*

protecting tomorrow, pp. 413–431. doi:10.2760/571085.

Santamaria, S., Kempná, K., Thomas, J.C., Houssami, M. El, *et al.* (2015) 'Investigation of Structural Wood Ignition By Firebrand Accumulation', *The First International Conference on Structural Safety under Fire and Blast*, (July 2016), pp. 1–13.

Santoso, M.A., Christensen, E.G., Yang, J. and Rein, G. (2019) 'Review of the Transition From Smouldering to Flaming Combustion in Wildfires', *Frontiers in Mechanical Engineering*, 5(September). doi:10.3389/fmech.2019.00049.

Sardoy, N., Consalvi, J.L., Porterie, B. and Fernandez-Pello, A.C. (2007) 'Modeling transport and combustion of firebrands from burning trees', *Combustion and Flame*, 150(3), pp. 151–169. doi:10.1016/j.combustflame.2007.04.008.

Sato, A. and Ono, M. (1990) 'Snowstorn Guard Fence Structures and Jey Roofs'.

Schug, F., Bar-Massada, A., Carlson, A.R., Cox, H., *et al.* (2023) 'The global wildland–urban interface', *Nature*, 621(May). doi:10.1038/s41586-023-06320-0.

Shields, T.J., Silcock, G.W.H. and Flood, M.F. (2001) 'Performance of a single glazing assembly exposed to enclosure corner fires of increasing severity', *Fire and Materials*, 25(4), pp. 123–152. doi:10.1002/fam.764.

Simeoni, A. (2016) 'Wildland Fires', in *SFPE Handbook of Fire Protection Engineering*. Fifth. Springer Science+Business Media, pp. 3283–3302.

Smith, E. and Adams, G. (1991) *Incline Village/Crystal Bay defensible space handbook*. University of Nevada, North Lake Tahoe Fire District.

SMMNRA (no date) *Sustainable Defensible Space*. Available at: https://defensiblespace.org/ (Accessed: 2 January 2023).

Stekhoven, D.J. and Bühlmann, P. (2012) 'Missforest - Non-parametric missing value imputation for mixed-type data', *Bioinformatics*, 28(1), pp. 112–118. doi:10.1093/bioinformatics/btr597.

Steward, L.G., Sydnor, T.D. and Bishop, B. (2003) 'The ease of ignition of 13 landscape mulches', *Journal of Arboriculture*, 29(6), pp. 317–321.

Stipho, A.S. (1992) 'Aeolian sand hazards and engineering design for desert regions', *Quarterly Journal of Engineering Geology*, 25(2), pp. 83–92. doi:10.1144/gsl.qjeg.1992.025.02.02.

Suzuki, S., Johnsson, E., Maranghides, A. and Manzello, S.L. (2016) 'Ignition of Wood Fencing Assemblies Exposed to Continuous Wind-Driven Firebrand Showers', *Fire Technology*, 52(4), pp. 1051–1067. doi:10.1007/s10694-015-0520-z.

Suzuki, S. and Manzello, S.L. (2017) 'Experimental investigation of firebrand accumulation zones in front of obstacles', *Fire Safety Journal*, 94(April), pp. 1–7. doi:10.1016/j.firesaf.2017.08.007.

Suzuki, S. and Manzello, S.L. (2018) 'Characteristics of Firebrands Collected from Actual Urban Fires', *Fire Technology*, 54(6), pp. 1533–1546. doi:10.1007/s10694-018-0751-x.

Suzuki, S. and Manzello, S.L. (2021a) 'Investigating Coupled Effect of Radiative Heat Flux and Firebrand Showers on Ignition of Fuel Beds', *Fire Technology*, 57(2), pp. 683–697. doi:10.1007/s10694-020-01018-5.

Suzuki, S. and Manzello, S.L. (2021b) 'Investigating the Effect of Structure to Structure Separation Distance on Firebrand Accumulation', *Frontiers in Mechanical Engineering*, 6(January), pp. 1–10. doi:10.3389/fmech.2020.628510.

Suzuki, S. and Manzello, S.L. (2021c) 'Towards understanding the effect of cedar roof covering application on firebrand production in large outdoor fires', *Journal of Cleaner Production*, 278, p. 123243. doi:10.1016/j.jclepro.2020.123243.

Suzuki, S. and Manzello, S.L. (2022) 'The processes of firebrand deposition and accumulation from wind-driven firebrand showers', *Fire and Materials*, (November), pp. 1–10. doi:10.1002/fam.3125.

Suzuki, S., Manzello, S.L., Kagiya, K., Suzuki, J. and Hayashi, Y. (2015) 'Ignition of Mulch Beds Exposed to Continuous Wind-Driven Firebrand Showers', *Fire Technology*, 51(4), pp. 905–922. doi:10.1007/s10694-014-0425-2.

Syphard, A.D., Keeley, J.E., Massada, A.B., Brennan, T.J. and Radeloff, V.C. (2012) 'Housing arrangement and location determine the likelihood of housing loss due to wildfire', *PLoS ONE*, 7(3). doi:10.1371/journal.pone.0033954.

Tabler, R.D. (1994) *Design Guidelines for the Control of Blowing and Drifting Snow*.

Takahashi, F. (2019) 'Whole-House Fire Blanket Protection From Wildland-Urban Interface Fires', *Frontiers in Mechanical Engineering*, 5(October). doi:10.3389/fmech.2019.00060.

Tarifa, C.S., Del Notario, P.P., Moreno, F.G. and Villa, A.R. (1967) 'Transport and combustion of firebrands', *Final Rep.*, II, p. 90.

Teague, B., McLeod, R. and Pascoe, S. (2010) *2009 Victorian Bushfires Royal Commision Final Report*. Parliament of Victoria.

Thomas, J.C., Mueller, E. V., Santamaria, S., Gallagher, M., *et al.* (2017) 'Investigation of firebrand generation from an experimental fire: Development of a reliable data collection methodology', *Fire Safety Journal*, 91(April), pp. 864–871. doi:10.1016/j.firesaf.2017.04.002.

Thurston, W., Kepert, J.D., Tory, K.J. and Fawcett, R.J.B. (2017) 'The contribution of turbulent plume dynamics to long-range spotting', *International Journal of Wildland Fire*, 26(4), pp. 317–330. doi:10.1071/WF16142.

Tilton, J.N. (1984) 'Fluid and Particle Dynamics', in *Perry's Chemical Engineers' Handbook*. sixth. New York: McGraw-Hill Inc.

Tohidi, A. (2016) 'Experimental and Numerical Modeling of Wildfire Spread via Fire Spotting', (August), pp. 1–222. Available at:

https://tigerprints.clemson.edu/all_dissertations.

Tohidi, A., Caton, S., Gollner, M. and Bryner, N. (2017) 'Thermo-mechanical breakage mechanism of firebrands', *10th U.S. National Combustion Meeting*, 2017-April(April).

Tomašević, I.Č., Cheung, K.K.W., Vučetić, V. and Fox-Hughes, P. (2022) 'Comparison of Wildfire Meteorology and Climate at the Adriatic Coast and Southeast Australia', *Atmosphere*, 13(5). doi:10.3390/atmos13050755.

Torero, J. (2016) 'Flaming Ignition of Solid Fuels', in *SFPE Handbook of Fire Protection Engineering*. Fifth. Springer Science, pp. 633–661. doi:DOI 10.1007/978-1-4939-2565-0.

Tse, S.D. and Fernandez-Pello, A.C. (1998) 'On the Flight Paths of Metal Particles and Embers Generated by Power Lines in High Winds - A Potential Source of Wildland Fires', *Fire Safety Journal*, 30(4), pp. 333–356. doi:10.1016/S0379-7112(97)00050-7.

Tsuda, A., Henry, F.S. and Butler, J.P. (2013) 'Particle transport and deposition: Basic physics of particle kinetics', *Comprehensive Physiology*, 3(4), pp. 1437–1471. doi:10.1002/cphy.c100085.

United Nations Environment Programme (2022) *Spreading like Wildfire – The Rising Threat of Extraordinary Landscape Fires*, *A UNEP Rapid Response Assessment*. Nairobi. doi:10.1038/news000413-8.

Urban, J.L., Song, J., Santamaria, S. and Fernandez-Pello, C. (2019) 'Ignition of a spot smolder in a moist fuel bed by a firebrand', *Fire Safety Journal*, 108(May), p. 102833. doi:10.1016/j.firesaf.2019.102833.

US Department of Housing and Urban Development (2021) *U.S. Census Bureau*, *Choice Reviews Online*. doi:10.5860/choice.49-3060.

Vacca, P., Caballero, D., Pastor, E. and Planas, E. (2020) 'WUI fire risk mitigation

in Europe: A performance-based design approach at home-owner level', *Journal of Safety Science and Resilience*, 1, pp. 97–105. doi:10.1016/j.jnlssr.2020.08.001.

Vacca, P., Planas, E., Mata, C., Muñoz, J.A., Heymes, F. and Pastor, E. (2022) 'Experimental analysis of real-scale burning tests of artificial fuel packs at the Wildland-Urban Interface', *Safety Science*, 146(September 2021). doi:10.1016/j.ssci.2021.105568.

Verisk (2022) *Wildfire Risk Analysis*, *Verisk.com*. Available at: https://www.verisk.com/insurance/campaigns/location-fireline-state-risk-report/ (Accessed: 13 June 2022).

Viegas, D.X., Almeida, M., Raposo, J., Oliveira, R. and Viegas, C.X. (2014) 'Ignition of Mediterranean Fuel Beds by Several Types of Firebrands', *Fire Technology*, 50(1), pp. 61–77. doi:10.1007/s10694-012-0267-8.

Wadhwani, R. (2019) *Physics-based simulation of short-range spotting in wildfires*. Victoria University.

Wadhwani, R., Sutherland, D., Ooi, A. and Moinuddin, K. (2022) 'Firebrand transport from a novel firebrand generator: Numerical simulation of laboratory experiments', *International Journal of Wildland Fire*, 31(6), pp. 634–648. doi:10.1071/WF21088.

Wadhwani, Sullivan, Wickramasinghe, Kyng, Khan and Moinuddin (2022) 'A review of firebrand studies on generation and transport', *Fire Safety Journal*, 134(September), p. 103674. doi:10.1016/j.firesaf.2022.103674.

Wadhwani, Sutherland, D., Ooi, A., Moinuddin, K. and Thorpe, G. (2017) 'Verification of a Lagrangian particle model for short-range firebrand transport', *Fire Safety Journal*, 91(May), pp. 776–783. doi:10.1016/j.firesaf.2017.03.019.

Watts, J.M. (2008) 'Fire Risk Indexing', in *The SFPE Handbook of Fire Protection Engineering*, pp. 5168–5185.

Wessies, S.S., Chang, M.K., Marr, K.C. and Ezekoye, O.A. (2019) 'Experimental and Analytical Characterization of Firebrand Ignition of Home Insulation Materials', *Fire Technology*, 55(3), pp. 1027–1056. doi:10.1007/s10694-019-00818-8.

Wheeler, J. (2004) 'Testing for Deck Material Flammability', *Fire Management*, 64(4), pp. 13–15.

White, N., Delichatsios, M., Ahrens, M. and Kimball, A. (2013) *Fire hazards of exterior wall assemblies containing combustible components*, *MATEC Web of Conferences*. doi:10.1051/matecconf/20130902005.

Wickramasinghe, A., Khan, N. and Moinuddin, K. (2022) 'Determining Firebrand Generation Rate Using Physics-Based Modelling from Experimental Studies through Inverse Analysis', *Fire*, 5(1). doi:10.3390/fire5010006.

Wilson, A.A.G. (1984) *Assessing the bushfire hazard of houses: A quantitative approach*. Melbourne.

Woycheese, J.P. and Pagni, P.J. (1999) 'Combustion models for wooden brands', *Proc. 3rd Int. Conf. on Fire Research and Engineering, Society of Fire Protection Engineers, Washington, USA*, p. 53.

Xiong, C., Liu, Y., Xu, C. and Huang, X. (2021) 'Acoustical Extinction of Flame on Moving Firebrand for the Fire Protection in Wildland–Urban Interface', *Fire Technology*, 57(3), pp. 1365–1380. doi:10.1007/s10694-020-01059-w.

Zhang, P., Sherman, D.J. and Li, B. (2021) 'Aeolian creep transport: A review', *Aeolian Research*, 51(April), p. 100711. doi:10.1016/j.aeolia.2021.100711.

Albini, F.A. (1979) *Spot Fire Distance from Burning Trees: A Predictive Model*. Edited by U. Intermountain Forest and Range Experiment Station (Ogden. USDA, Forest Service (General technical report INT).

Albini, F.A. (1981) 'Spot fire distance from isolated sources - extensions of a predictive model', *USDA Forest Service Research Note*, INT-309, p. 9p.

Albini, F.A. (1983) 'Transport of firebrands by line thermalst', *Combustion Science and Technology*, 32(5–6), pp. 277–288. doi:10.1080/00102208308923662.

Andersen, L.M. and Sugg, M.M. (2019) 'Geographic multi-criteria evaluation and validation: A case study of wildfire vulnerability in Western North Carolina, USA following the 2016 wildfires', *International Journal of Disaster Risk Reduction*, 39. doi:10.1016/j.ijdrr.2019.101123.

Anderson, J.D. (1995) *Computational Fluid Dynamics*. New York: McGraw-Hill Inc.

Anthenien, R.A., Tse, S.D. and Carlos Fernandez-Pello, A. (2006) 'On the trajectories of embers initially elevated or lofted by small scale ground fire plumes in high winds', *Fire Safety Journal*, 41(5), pp. 349–363. doi:10.1016/j.firesaf.2006.01.005.

Babrauskas, V. (2003) 'Ignition Sources', in *Ignition Handbook*, pp. 497–590.

Babrauskas, V. (2018) 'Firebrands and Embers', in Manzello, S.L. (ed.) *Encyclopedia of Wildfires and Wildland-Urban Interface (WUI) Fires*. Cham: Springer International Publishing, pp. 1–14. doi:10.1007/978-3-319-51727-8_3-1.

Bagnold, R.A. (1974) *The Physics of Blown Sand and Desert Dunes*. Springer Dordrecht. doi:https://doi.org/10.1007/978-94-009-5682-7.

Barr, B.W. and Ezekoye, O.A. (2013) 'Thermo-mechanical modeling of firebrand breakage on a fractal tree', *Proceedings of the Combustion Institute*, 34(2), pp. 2649–2656. doi:10.1016/j.proci.2012.07.066.

Belly, P.Y. (1964) *Sand movement by wind, technical report*.

Billmire, M., French, N.H.F., Loboda, T., Owen, R.C. and Tyner, M. (2014) 'Santa Ana winds and predictors of wildfire progression in southern California', *International Journal of Wildland Fire*, 23(8), pp. 1119–1129. doi:10.1071/WF13046.

Biswas, K., Werth, D. and Gupta, N. (2013) 'A home ignition assessment model

applied to structures in the wildland-urban interface', *Thermal Performance of the Exterior Envelopes of Whole Buildings XII International Conference* [Preprint].

Blanchi, R., Leonard, J.E. and Leicester, R.H. (2006) 'Lessons learnt from post-bushfire surveys at the urban interface in Australia', *Forest Ecology and Management*, 234. doi:10.1016/j.foreco.2006.08.184.

Boboulos, M. and Purvis, M.R.I. (2009) 'Wind and slope effects on ROS during the fire propagation in East-Mediterranean pine forest litter', *Fire Safety Journal*, 44(5), pp. 764–769. doi:10.1016/j.firesaf.2009.03.006.

Bruno, L., Horvat, M. and Raffaele, L. (2018) 'Windblown sand along railway infrastructures: A review of challenges and mitigation measures', *Journal of Wind Engineering and Industrial Aerodynamics*, 177(April), pp. 340–365. doi:10.1016/j.jweia.2018.04.021.

Butler, C.P. (1974) 'The Urban/Wildland Fire Interface', *Proceedings of Western Stattes Section/Combustion Institute Papers*, 74(15), pp. 1–17.

Cantor, P., Arruda, M.R.T., Firmo, J. and Branco, F. (2023) 'Development of a standard firebrand accumulation temperature curve for residential wildfire protection system', *Results in Engineering*, 17(February), p. 100935. doi:10.1016/j.rineng.2023.100935.

Caton, S.E., Hakes, R.S.P., Gorham, D.J., Zhou, A. and Gollner, M.J. (2017) 'Review of Pathways for Building Fire Spread in the Wildland Urban Interface Part I: Exposure Conditions', *Fire Technology*, 53(2), pp. 429–473. doi:10.1007/s10694-016-0589-z.

Chappaz, F. and Ganteaume, A. (2022) 'Role of land-cover and WUI types on spatio-temporal dynamics of fires in the French Mediterranean area', *Risk Analysis*, pp. 1032–1057. doi:10.1111/risa.13979.

Cheng, J. jun and Xue, C. xiao (2014) 'The sand-damage-prevention engineering system for the railway in the desert region of the Qinghai-Tibet plateau', *Journal of*

Wind Engineering and Industrial Aerodynamics, 125, pp. 30–37. doi:10.1016/j.jweia.2013.11.016.

Chhabra, R.P., Agarwal, L. and Sinha, N.K. (1999) 'Drag on non-spherical particles: An evaluation of available methods', *Powder Technology*, 101(3), pp. 288–295. doi:10.1016/S0032-5910(98)00178-8.

Cohen, J. (1988) *Statistical Power Analysis for the Behavioral Sciences*. 2nd edn. New York: Lawrence Erlbaum Associates, Publishers. doi:https://doi.org/10.4324/9780203771587.

Cohen, J. and Butler, B. (1996) 'Modeling potential structure ignitions from flame radiation exposure with implications for wildland/urban interface fire management', *Thirteenth Fire and Forest Meteorology …*, pp. 81–87.

Cohen, J.D. (2000) 'Preventing disaster: Home ignitability in the wildland-urban interface', *Journal of Forestry*, 98(3), pp. 15–21.

Cohen, J.D. (2004) 'Relating flame radiation to home ignition using modeling and experimental crown fires', *Canadian Journal of Forest Research*, 34(8). doi:https://doi.org/10.1139/x04-049.

Cohen, J.D. (2008) 'The wildland-urban interface fire problem: a consequence of the fire exclusion paradigm.', *Forest History Today*, 2008, pp. 20–26.

Defossé, G.E. (2023) 'Editorial: Fires in the wildland urban interface: An emerging global phenomenon threatening modern society', *Frontiers in Forest and Global Change*, 6. doi:doi: 10.3389/ffgc.2023.1137014 COPYRIGHT.

Dong, Z., Luo, W., Qian, G. and Wang, H. (2007) 'A wind tunnel simulation of the mean velocity fields behind upright porous fences', *Agricultural and Forest Meteorology*, 146(1–2), pp. 82–93. doi:10.1016/j.agrformet.2007.05.009.

Dossi, S., Messerschmidt, B., Ribeiro, L.M., Almeida, M. and Rein, G. (2022) 'Relationships between building features and wildfire damage in California, USA and

Pedrógão Grande, Portugal', *International Journal of Wildland Fire*, 32(2), pp. 296–312. doi:10.1071/wf22095.

Escadafal, R., Bernoux, M., Bonnet, B., Cornet, A., *et al.* (2011) 'The African Great Green Wall project. What advice can scientists provide?', *Comité Scientifique Français de la Désertification (CSFD) Topical issue - The African Great Green Wall project*, (October), p. 41. Available at: www.csf-desertification.org/grande-muraille-verte.

Filkov, A., Prohanov, S., Mueller, E., Kasymov, D., *et al.* (2017) 'Investigation of firebrand production during prescribed fires conducted in a pine forest', *Proceedings of the Combustion Institute*, 36(2), pp. 3263–3270. doi:10.1016/j.proci.2016.06.125.

Finney, M.A., Cohen, J.D., Forthofer, J.M., McAllister, S.S., *et al.* (2015) 'Role of buoyant flame dynamics in wildfire spread', *Proceedings of the National Academy of Sciences of the United States of America*, 112(32), pp. 9833–9838. doi:10.1073/pnas.1504498112.

Fire Illustration (2023).

Galiana-Martin, L., Herrero, G. and Solana, J. (2011) 'A wildland-urban interface typology for forest fire risk management in mediterranean areas', *Landscape Research*, 36(2), pp. 151–171. doi:10.1080/01426397.2010.549218.

Gillies, J.A. and Lancaster, N. (2013) 'Large roughness element effects on sand transport, Oceano Dunes, California', *Earth Surface Processes and Landforms*, 38(8), pp. 785–792. doi:10.1002/esp.3317.

Gillies, J.A., Nickling, W.G. and King, J. (2006) 'Aeolian sediment transport through large patches of roughness in the atmospheric inertial sublayer', *Journal of Geophysical Research: Earth Surface*, 111(2), pp. 1–13. doi:10.1029/2005JF000434.

Giudice, A. Lo, Nuca, R., Preziosi, L. and Coste, N. (2019) 'Wind-blown particulate transport: A review of computational fluid dynamics models', *Mathematics In Engineering*, 1(3), pp. 508–547. doi:10.3934/mine.2019.3.508.

Godoy, M.M., Martinuzzi, S., Masera, P. and Defossé, G.E. (2022) 'Forty Years of Wildland Urban Interface Growth and Its Relation With Wildfires in Central-Western Chubut, Argentina', *Frontiers in Forests and Global Change*, 5(June), pp. 1–15. doi:10.3389/ffgc.2022.850543.

Graham, R., Finney, M., McHugh, C., Cohen, J., *et al.* (2012) *Fourmile canyon fire findings*, *USDA Forest Service - General Technical Report RMRS-GTR*.

Guangyong, L. and Peng, M. (2012) 'Wind-preventing sand-throwing wall'.

Gunel, E. and Dickey, J. (1974) 'Bayes Factors for Independence in Contingency Tables', *Biometrika*, 61(3), pp. 545–557. Available at: https://www.jstor.org/stable/2334738.

Hadden, R.M., Scott, S., Lautenberger, C. and Fernandez-Pello, C.C. (2011) 'Ignition of Combustible Fuel Beds by Hot Particles: An Experimental and Theoretical Study', *Fire Technology*, 47(2), pp. 341–355. doi:10.1007/s10694-010-0181-x.

Haider, A. and Levenspiel, O. (1989) 'Drag Coefficient and Terminal Velocity of Spherical and Nonspherical Particles', *Powder Technology*, 58, pp. 63–70.

Hakes, R.S.P., Caton, S.E., Gorham, D.J. and Gollner, M.J. (2017) 'A Review of Pathways for Building Fire Spread in the Wildland Urban Interface Part II: Response of Components and Systems and Mitigation Strategies in the United States', *Fire Technology*, 53(2), pp. 475–515. doi:10.1007/s10694-016-0601-7.

Hashempour, J. and Sharifian, A. (2017) 'Effective factors on the performance of woven wire screens against leaf firebrand attacks', *Journal of Fire Sciences*, 35(4), pp. 303–316. doi:10.1177/0734904117709203.

Hedayati, F., Bahrani, B., Zhou, A., Quarles, S.L. and Gorham, D.J. (2019) 'A Framework to Facilitate Firebrand Characterization', *Frontiers in Mechanical Engineering*, 5(July), pp. 1–14. doi:10.3389/fmech.2019.00043.

Henning, A., Cox, J. and Shew, D. (2016) *CAL FIRE's Damage Inspection*

Program - Its Evolution and Implementation, *NFPA Conference & Expo*. Available at: http://www.fltwood.com/perm/nfpa-2016/scripts/sessions/M26.html (Accessed: 25 January 2022).

Himoto, K. and Hayashi, Y. (2022) 'Hierarchical Bayesian approach to developing probabilistic models for generation and transport of firebrands in large outdoor fires under limited data availability', *Fire Safety Journal*, 134(September), p. 103679. doi:10.1016/j.firesaf.2022.103679.

Himoto, K. and Tanaka, T. (2005) 'Transport of disk-shaped firebrands in a turbulent boundary layer', *Fire Safety Science*, pp. 433–444. doi:10.3801/IAFSS.FSS.8-433.

Hong, S.W., Lee, I.B. and Seo, I.H. (2015) 'Modelling and predicting wind velocity patterns for windbreak fence design', *Journal of Wind Engineering and Industrial Aerodynamics*, 142, pp. 53–64. doi:10.1016/j.jweia.2015.03.007.

Hotta, S. and Horikawa, K. (1990) 'Function of Sand Fence Placed in Front of Embankment', in *Coastal Engineering*, pp. 2754–2767. doi:https://doi.org/10.1061/9780872627765.211.

Hudson, T.R., Bray, R.B., Blunck, D.L., Page, W. and Butler, B. (2020) 'Effects of fuel morphology on ember generation characteristics at the tree scale', *International Journal of Wildland Fire*, 29(11), pp. 1042–1051. doi:10.1071/WF19182.

Hughes, M. and Hall, A. (2010) 'Local and synoptic mechanisms causing Southern California's Santa Ana winds', *Climate Dynamics*, 34(6), pp. 847–857. doi:10.1007/s00382-009-0650-4.

Hysa, A. (2021) 'Indexing the vegetated surfaces within WUI by their wildfire ignition and spreading capacity, a comparative case from developing metropolitan areas', *International Journal of Disaster Risk Reduction*, 63. doi:10.1016/j.ijdrr.2021.102434.

IBHS (2021) *Suburban Wildfire Adaptation Roadmaps*. Available at:

https://ibhs.org/wp-content/uploads/ibhs-wildfire-roadmaps_executive-summary.pdf.

IBHS (2022) *Wildfire Prepared*. Available at: https://wildfireprepared.org/ (Accessed: 30 October 2022).

Intini, P., Ronchi, E., Gwynne, S. and Bénichou, N. (2020) *Guidance on Design and Construction of the Built Environment Against Wildland Urban Interface Fire Hazard: A Review*, *Fire Technology*. doi:10.1007/s10694-019-00902-z.

Kadel, J., Hedayati, F., Quarles, S.L. and Zhou, A. (2021) 'Effect of Environmental Conditions on the Dehydration and Performance of Fire-Protective Gels', *Fire Technology*, 57(3), pp. 1241–1257. doi:10.1007/s10694-020-01045-2.

Kimiko, B. (2022) *Wood roofs are a $6 billion wildfire problem*. Available at: https://headwaterseconomics.org/natural-hazards/wood-roofs-wildfire/ (Accessed: 5 September 2022).

Klassen, M.S., Sutula, J.A., Holton, M.M. and Roby, R.J. (2010) 'Transmission Through and Breakage of Single and Multi-Pane Glazing Due to Radiant Exposure: State of Research', *Fire Technology*, 46(4), pp. 821–832. doi:10.1007/s10694-010-0150-4.

Knapp, E.E., Valachovic, Y.S., Quarles, S.L. and Johnson, N.G. (2021) 'Housing arrangement and vegetation factors associated with single-family home survival in the 2018 Camp Fire, California', *Fire Ecology*, 17(1). doi:10.1186/s42408-021-00117-0.

Kok, J.F. (2010) 'Analytical calculation of the minimum wind speed required to sustain wind-blown sand on Earth and Mars', *arXiv preprint arXiv:1001.4840* [Preprint].

Kok, J.F., Parteli, E.J.R., Michaels, T.I. and Karam, D.B. (2012) 'The physics of wind-blown sand and dust', *Reports on Progress in Physics*, 75(10), pp. 1–119. doi:10.1088/0034-4885/75/10/106901.

Koo, E., Linn, R.R., Pagni, P.J. and Edminster, C.B. (2012) 'Modelling firebrand transport in wildfires using HIGRAD/FIRETEC', *International Journal of Wildland Fire*, 21(4), pp. 396–417. doi:10.1071/WF09146.

Koo, E., Pagni, P.J., Weise, D.R. and Woycheese, J.P. (2010) 'Firebrands and spotting ignition in large-scale fires', *International Journal of Wildland Fire*, 19(7), pp. 818–843. doi:10.1071/WF07119.

Kursa, M.B. and Rudnicki, W.R. (2010) 'Feature selection with the boruta package', *Journal of Statistical Software*, 36(11), pp. 1–13. doi:10.18637/jss.v036.i11.

Kwon, B. and Liao, Y.T.T. (2022) 'Effects of spacing on flaming and smoldering firebrands in wildland–urban interface fires', *Journal of Fire Sciences*, 40(3), pp. 155–174. doi:10.1177/07349041221081998.

Lee, M.D. and Wagenmakers, E.J. (2014) *Bayesian Cognitive Modeling: A Practical Course*. Cambridge University Press. Available at: https://books.google.co.uk/books?id=50tkAgAAQBAJ.

Lee, S.L. and Hellman, J.M. (1970) 'Firebrand trajectory study using an empirical velocity-dependent burning law', *Combustion and Flame*, 15(3), pp. 265–274. doi:10.1016/0010-2180(70)90006-4.

Liu, D.L. (2009) 'Particle Deposition onto Enclosure Surfaces', *Developments in Surface Contamination and Cleaning*, pp. 1–56. doi:10.1016/B978-1-4377-7830-4.10001-5.

Mankame, A. and Shotorban, B. (2021) 'Deposition Characteristics of Firebrands on and Around Rectangular Cubic Structures', *Frontiers in Mechanical Engineering*, 7, pp. 1–14. doi:10.3389/fmech.2021.640979.

Manzello, S.L. (2013) *The Performance of Concrete Tile and Terracotta Tile Roofing Assemblies Exposed to Wind-Driven Firebrand Showers*. doi:http://dx.doi.org/10.6028/NIST.TN.1794.

Manzello, S.L., Blanchi, R., Gollner, M.J., Gorham, D., *et al.* (2018) 'Summary of workshop large outdoor fires and the built environment', *Fire Safety Journal*, 100, pp. 76–92. doi:10.1016/j.firesaf.2018.07.002.

Manzello, S.L. and Foote, E.I.D. (2014) 'Characterizing Firebrand Exposure from Wildland-Urban Interface (WUI) Fires: Results from the 2007 Angora Fire', *Fire Technology*, 50(1), pp. 105–124. doi:10.1007/s10694-012-0295-4.

Manzello, S.L., Hayashi, Y., Yoneki, T. and Yamamoto, Y. (2010) 'Quantifying the vulnerabilities of ceramic tile roofing assemblies to ignition during a firebrand attack', *Fire Safety Journal*, 45(1), pp. 35–43. doi:10.1016/j.firesaf.2009.09.002.

Manzello, S.L., Park, S.-H., Shields, J.R., Hayashi, Y. and Suzuki, S. (2010) *Comparison Testing Protocol for Firebrand Penetration through Building Vents : Summary of BRI / NIST Full Scale and NIST Reduced Scale Results*. Gaithersburg, MD.

Manzello, S.L., Shields, J.R., Hayashi, Y. and Nii, D. (2009) 'Investigating the vulnerabilities of structures to ignition from a firebrand attack', *Fire Safety Science*, 9, pp. 143–154. doi:10.3801/IAFSS.FSS.9-143.

Manzello, S.L. and Suzuki, S. (2013) 'Experimentally simulating wind driven firebrand showers in wildland-urban interface (WUI) fires: Overview of the NIST firebrand generator (NIST dragon) technology', *Procedia Engineering*, 62, pp. 91–102. doi:10.1016/j.proeng.2013.08.047.

Manzello, S.L. and Suzuki, S. (2014) 'Exposing decking assemblies to continuous wind-driven firebrand showers', *Fire Safety Science*, 11, pp. 1339–1352. doi:10.3801/IAFSS.FSS.11-1339.

Manzello, S.L., Suzuki, S., Gollner, M.J. and Fernandez-Pello, A.C. (2020) 'Role of firebrand combustion in large outdoor fire spread', *Progress in Energy and Combustion Science*, 76, p. 100801. doi:10.1016/j.pecs.2019.100801.

Manzello, S.L., Suzuki, S. and Hayashi, Y. (2012) 'Exposing siding treatments,

walls fitted with eaves, and glazing assemblies to firebrand showers', *Fire Safety Journal*, 50, pp. 25–34. doi:10.1016/j.firesaf.2012.01.006.

Manzello, S.L., Suzuki, S. and Naruse, T. (2019) 'Quantifying wind-driven firebrand production from roofing assembly combustion', *Fire and Materials*, 43(1), pp. 3–7. doi:10.1002/fam.2661.

Maranghides, A. and Johnsson, E. (2008) *NIST Technical Note 1600 Residential Structure Separation Fire Experiments*.

Maranghides, A., Link, E., Mell, W.R., Maranghides, A., Nazare, S. and Link, E. (2022) *NIST Outdoor Structure Separation Experiments (NOSSE): Preliminary Test Plan*. doi:https://doi.org/10.6028/NIST.TN.2199.

Maranghides, A. and Mell, W. (2012) *Framework for Addressing the National Wildland Urban Interface Fire Problem- Determining Fire and Ember Exposure Zones using a WUI Hazard Scale*. NIST Technical Note 1748.

McArthur, A.G. (1967) *Fire behaviour in eucalypt forests*. Canberra: Forestry and Timber Bureau.

McGrattan, K. and Miles, S. (2016) 'Modeling Fires Using Computational Fluid Dynamics (CFD)', in *SFPE Handbook of Fire Protection Engineering*. Fifth. New York: Springer.

McGrattan, K.B., Baum, H.R., Rehm, R.G., Hamins, A. and Forney, G.P. (2021) 'Fire Dynamics Simulator - Technical Reference Manual', *NIST Special Publication 1018-1. US Department of Commerce, National Institute of Standards and Technology. Gaithersburg, MD.*, 1(5), p. 175.

McLaughlin, W.T. (1942) *Controlling coastal sand dunes in the Pacific Northwest*.

Meerpoel-Pietri, K., Tihay-Felicelli, V. and Santoni, P.A. (2021) 'Determination of the critical conditions leading to the ignition of decking slabs by flaming firebrands',

Fire Safety Journal, 120. doi:10.1016/j.firesaf.2020.103017.

Meier, S., Elliott, R.J.R. and Strobl, E. (2023) 'The regional economic impact of wildfires: Evidence from Southern Europe', *Journal of Environmental Economics and Management*, 118(May 2022), p. 102787. doi:10.1016/j.jeem.2023.102787.

Mell, W.E., Manzello, S.L., Maranghides, A., Butry, D. and Rehm, R.G. (2010) 'The Wildland – Urban Interface Fire Problem – Current Approaches and Research Needs', *International Journal Of Wildland Fire*, 2005, pp. 238–251.

Mendes, P.J.N.F. (2013) *A influência do RCCTE na Arquitetura e as Perspetivas para o Futuro*. Universidade do Minho. Available at: https://hdl.handle.net/1822/27624.

Moinuddin, K. and Wadhwani, R. (2019) 'Simulated 6th International Fire Behavior and transport of short-range embers in an idealised bushfire', (May).

Moritz, M.A., Batllori, E., Bradstock, R.A., Gill, A.M., *et al.* (2014) 'Learning to coexist with wildfire', *Nature*, 515(7525), pp. 58–66. doi:10.1038/nature13946.

Muraszew, A., Fedele, J.B. and Kuby, W.C. (1977) 'Trajectory of firebrands in and out of fire whirls', *Combustion and Flame*, 30(C), pp. 321–324. doi:10.1016/0010-2180(77)90081-5.

National Fire Protection Association (2022) *FireWise USA*. Available at: https://www.nfpa.org/Public-Education/Fire-causes-and-risks/Wildfire/Firewise-USA (Accessed: 17 September 2022).

NFPA 1140 (2022) *NFPA 1140 Standard for Wildland Fire Protection*. Available at: https://www.nfpa.org/codes-and-standards.

Nguyen, D. and Kaye, N.B. (2021) 'Experimental investigation of rooftop hotspots during wildfire ember storms', *Fire Safety Journal*, 125. doi:10.1016/j.firesaf.2021.103445.

Nguyen, D. and Kaye, N.B. (2022a) 'Quantification of ember accumulation on the

rooftops of isolated buildings in an ember storm', *Fire Safety Journal*, 128(103525). doi:10.1016/j.firesaf.2022.103525.

Nguyen, D. and Kaye, N.B. (2022b) 'The role of surrounding buildings on the accumulation of embers on rooftops during an ember storm', *Fire Safety Journal*, 131(103624). doi:10.1016/j.firesaf.2022.103624.

Oke, T.R. (1987) *Boundary Layer Climates*. 2nd edn. Routledge. doi:https://doi.org/10.4324/9780203407219.

Orloff, L., De Ris, J. and Markstein, G.H. (1975) 'Upward turbulent fire spread and burning of fuel surface', *Symposium (International) on Combustion*, 15(1), pp. 183–192. doi:10.1016/S0082-0784(75)80296-7.

Pampaka, M., Hutcheson, G. and Williams, J. (2016) 'Handling missing data: analysis of a challenging data set using multiple imputation', *International Journal of Research and Method in Education*, 39(1), pp. 19–37. doi:10.1080/1743727X.2014.979146.

Papakosta, P., Xanthopoulos, G. and Straub, D. (2017) 'Probabilistic prediction of wildfire economic losses to housing in Cyprus using Bayesian network analysis', *International Journal of Wildland Fire*, 26(1), pp. 10–23. doi:10.1071/WF15113.

Papathoma-Köhle, M., Schlögl, M., Garlichs, C., Diakakis, M., Mavroulis, S. and Fuchs, S. (2022) 'A wildfire vulnerability index for buildings', *Scientific Reports Nature*, 12(1), pp. 1–15. doi:10.1038/s41598-022-10479-3.

Piomelli, U. (2014) 'Large eddy simulations in 2030 and beyond', *Philosophical Transactions of the Royal Society*, 372(2022). doi:10.1098/rsta.2013.0320.

Potter, M. and Leonard, J. (2010) 'Spray System Design for Ember Attack - Research Findings and Discussion Paper', (D), p. 30.

Pyne, S.J. (1949) *Vestal Fire: An Environmental History, Told through Fire, of Europe and Europe's Encounter with the World*. Seattle and London: University of

Washington Press.

Quarles, S. and Standohar-Alfano, C. (2018) *Ignition Potential of Decks Subjected to an Ember Exposure*. Available at: http://disastersafety.org/wp-content/uploads/2017/10/Deck-Ember-Testing-Report-2017_IBHS.pdf.

Quarles, S.L. and Sindelar, M. (2011) *Wildfire Ignition Resistant Home Design (WIRHD) Program: Full-scale Testing and Demonstration Final Report*. Available at: https://www.osti.gov/servlets/purl/1032503.

Quarles, S.L., Standohar-Alfano, C., Hedayati, F. and Gorham, D.J. (2023) 'Factors influencing ember accumulation near a building', *International Journal of Wildland Fire*, pp. 1–8. doi:10.1071/wf22132.

Quarles, S.L., Valachovic, Y., Nakamura, G.M., Nader, G.A. and de Lasaux, M.J. (2010) 'Home Survival in Wildfire-Prone Areas: Building Materials and Design Considerations', *Home Survival in Wildfire-Prone Areas: Building Materials and Design Considerations*, pp. 1–22. doi:10.3733/ucanr.8393.

Radeloff, V.C., Helmers, D.P., Anu Kramer, H., Mockrin, M.H., *et al.* (2018) 'Rapid growth of the US wildland-urban interface raises wildfire risk', *Proceedings of the National Academy of Sciences of the United States of America*, 115(13), pp. 3314–3319. doi:10.1073/pnas.1718850115.

Raffaele, L., Bruno, L., Pellerey, F. and Preziosi, L. (2016) 'Windblown sand saltation: A statistical approach to fluid threshold shear velocity', *Aeolian Research*, 23, pp. 79–91. doi:10.1016/j.aeolia.2016.10.002.

Ragland, K.W., Aerts, D.J. and Baker, A.J. (1991) 'Properties of wood for combustion analysis', *Bioresource Technology*, 37(2), pp. 161–168. doi:10.1016/0960-8524(91)90205-X.

Rahim, M. (1945) 'Behaviour of Drift Sand and Method of Dealing with it', *Pakistan Engineering Congress* [Preprint].

Randerson, D. (1978) 'Atmospheric Boundary Layer.', *US Department of Energy, Technical Information Center, (Technical Report) DOE/TIC*, 37, pp. 147–188. doi:10.1201/9781439847121-c2.

Rea, L. and Parker, R. (1962) *Designing and Conducting Survey Research: A Comprehensive Guide*. San Francisco: Jossey-Bass Publishers.

Ribeiro, L.M., Rodrigues, A., Lucas, D. and Viegas, D.X. (2020) 'The impact on structures of the pedrógão grande fire complex in June 2017 (Portugal)', *Fire*, 3(4), pp. 1–22. doi:10.3390/fire3040057.

Rouder, J.N., Speckman, P.L., Sun, D., Morey, R.D. and Iverson, G. (2009) 'Bayesian t tests for accepting and rejecting the null hypothesis', *Psychonomic Bulletin and Review*, 16(2), pp. 225–237. doi:10.3758/PBR.16.2.225.

Samora-Arvela, A., Aranha, J., Correia, F., Pinto, D.M., Magalhães, C. and Tedim, F. (2023) 'Understanding Building Resistance to Wildfires: A Multi-Factor Approach', *Fire*, 6(1), pp. 1–15. doi:10.3390/fire6010032.

San-Miguel-Ayanz, J., Moreno, J.M. and Camia, A. (2013) 'Analysis of large fires in European Mediterranean landscapes: Lessons learned and perspectives', *Forest Ecology and Management*, 294, pp. 11–22. doi:10.1016/j.foreco.2012.10.050.

San-Miguel-Ayanz, J., Oom, D., Artès, T., Viegas, D.X., *et al.* (2021) 'Forest fires in Portugal in 2017', *Science for Disaster Risk Management 2020: acting today, protecting tomorrow*, pp. 413–431. doi:10.2760/571085.

Santamaria, S., Kempná, K., Thomas, J.C., Houssami, M. El, *et al.* (2015) 'Investigation of Structural Wood Ignition By Firebrand Accumulation', *The First International Conference on Structural Safety under Fire and Blast*, (July 2016), pp. 1–13.

Santoso, M.A., Christensen, E.G., Yang, J. and Rein, G. (2019) 'Review of the Transition From Smouldering to Flaming Combustion in Wildfires', *Frontiers in Mechanical Engineering*, 5(September). doi:10.3389/fmech.2019.00049.

Sardoy, N., Consalvi, J.L., Porterie, B. and Fernandez-Pello, A.C. (2007) 'Modeling transport and combustion of firebrands from burning trees', *Combustion and Flame*, 150(3), pp. 151–169. doi:10.1016/j.combustflame.2007.04.008.

Sato, A. and Ono, M. (1990) 'Snowstorn Guard Fence Structures and Jey Roofs'.

Schug, F., Bar-Massada, A., Carlson, A.R., Cox, H., *et al.* (2023) 'The global wildland–urban interface', *Nature*, 621(May). doi:10.1038/s41586-023-06320-0.

Shields, T.J., Silcock, G.W.H. and Flood, M.F. (2001) 'Performance of a single glazing assembly exposed to enclosure corner fires of increasing severity', *Fire and Materials*, 25(4), pp. 123–152. doi:10.1002/fam.764.

Simeoni, A. (2016) 'Wildland Fires', in *SFPE Handbook of Fire Protection Engineering*. Fifth. Springer Science+Business Media, pp. 3283–3302.

Smith, E. and Adams, G. (1991) *Incline Village/Crystal Bay defensible space handbook*. University of Nevada, North Lake Tahoe Fire District.

SMMNRA (no date) *Sustainable Defensible Space*. Available at: https://defensiblespace.org/ (Accessed: 2 January 2023).

Stekhoven, D.J. and Bühlmann, P. (2012) 'Missforest - Non-parametric missing value imputation for mixed-type data', *Bioinformatics*, 28(1), pp. 112–118. doi:10.1093/bioinformatics/btr597.

Steward, L.G., Sydnor, T.D. and Bishop, B. (2003) 'The ease of ignition of 13 landscape mulches', *Journal of Arboriculture*, 29(6), pp. 317–321.

Stipho, A.S. (1992) 'Aeolian sand hazards and engineering design for desert regions', *Quarterly Journal of Engineering Geology*, 25(2), pp. 83–92. doi:10.1144/gsl.qjeg.1992.025.02.02.

Suzuki, S., Johnsson, E., Maranghides, A. and Manzello, S.L. (2016) 'Ignition of Wood Fencing Assemblies Exposed to Continuous Wind-Driven Firebrand Showers', *Fire Technology*, 52(4), pp. 1051–1067. doi:10.1007/s10694-015-0520-z.

Suzuki, S. and Manzello, S.L. (2017) 'Experimental investigation of firebrand accumulation zones in front of obstacles', *Fire Safety Journal*, 94(April), pp. 1–7. doi:10.1016/j.firesaf.2017.08.007.

Suzuki, S. and Manzello, S.L. (2018) 'Characteristics of Firebrands Collected from Actual Urban Fires', *Fire Technology*, 54(6), pp. 1533–1546. doi:10.1007/s10694-018-0751-x.

Suzuki, S. and Manzello, S.L. (2021a) 'Investigating Coupled Effect of Radiative Heat Flux and Firebrand Showers on Ignition of Fuel Beds', *Fire Technology*, 57(2), pp. 683–697. doi:10.1007/s10694-020-01018-5.

Suzuki, S. and Manzello, S.L. (2021b) 'Investigating the Effect of Structure to Structure Separation Distance on Firebrand Accumulation', *Frontiers in Mechanical Engineering*, 6(January), pp. 1–10. doi:10.3389/fmech.2020.628510.

Suzuki, S. and Manzello, S.L. (2021c) 'Towards understanding the effect of cedar roof covering application on firebrand production in large outdoor fires', *Journal of Cleaner Production*, 278, p. 123243. doi:10.1016/j.jclepro.2020.123243.

Suzuki, S. and Manzello, S.L. (2022) 'The processes of firebrand deposition and accumulation from wind-driven firebrand showers', *Fire and Materials*, (November), pp. 1–10. doi:10.1002/fam.3125.

Suzuki, S., Manzello, S.L., Kagiya, K., Suzuki, J. and Hayashi, Y. (2015) 'Ignition of Mulch Beds Exposed to Continuous Wind-Driven Firebrand Showers', *Fire Technology*, 51(4), pp. 905–922. doi:10.1007/s10694-014-0425-2.

Syphard, A.D., Keeley, J.E., Massada, A.B., Brennan, T.J. and Radeloff, V.C. (2012) 'Housing arrangement and location determine the likelihood of housing loss due to wildfire', *PLoS ONE*, 7(3). doi:10.1371/journal.pone.0033954.

Tabler, R.D. (1994) *Design Guidelines for the Control of Blowing and Drifting Snow*.

Takahashi, F. (2019) 'Whole-House Fire Blanket Protection From Wildland-Urban Interface Fires', *Frontiers in Mechanical Engineering*, 5(October). doi:10.3389/fmech.2019.00060.

Tarifa, C.S., Del Notario, P.P., Moreno, F.G. and Villa, A.R. (1967) 'Transport and combustion of firebrands', *Final Rep.*, II, p. 90.

Teague, B., McLeod, R. and Pascoe, S. (2010) *2009 Victorian Bushfires Royal Commision Final Report*. Parliament of Victoria.

Thomas, J.C., Mueller, E. V., Santamaria, S., Gallagher, M., *et al.* (2017) 'Investigation of firebrand generation from an experimental fire: Development of a reliable data collection methodology', *Fire Safety Journal*, 91(April), pp. 864–871. doi:10.1016/j.firesaf.2017.04.002.

Thurston, W., Kepert, J.D., Tory, K.J. and Fawcett, R.J.B. (2017) 'The contribution of turbulent plume dynamics to long-range spotting', *International Journal of Wildland Fire*, 26(4), pp. 317–330. doi:10.1071/WF16142.

Tilton, J.N. (1984) 'Fluid and Particle Dynamics', in *Perry's Chemical Engineers' Handbook*. sixth. New York: McGraw-Hill Inc.

Tohidi, A. (2016) 'Experimental and Numerical Modeling of Wildfire Spread via Fire Spotting', (August), pp. 1–222. Available at: https://tigerprints.clemson.edu/all_dissertations.

Tohidi, A., Caton, S., Gollner, M. and Bryner, N. (2017) 'Thermo-mechanical breakage mechanism of firebrands', *10th U.S. National Combustion Meeting*, 2017-April(April).

Tomašević, I.Č., Cheung, K.K.W., Vučetić, V. and Fox-Hughes, P. (2022) 'Comparison of Wildfire Meteorology and Climate at the Adriatic Coast and Southeast Australia', *Atmosphere*, 13(5). doi:10.3390/atmos13050755.

Torero, J. (2016) 'Flaming Ignition of Solid Fuels', in *SFPE Handbook of Fire*

Protection Engineering. Fifth. Springer Science, pp. 633–661. doi:DOI 10.1007/978-1-4939-2565-0.

Tse, S.D. and Fernandez-Pello, A.C. (1998) 'On the Flight Paths of Metal Particles and Embers Generated by Power Lines in High Winds - A Potential Source of Wildland Fires', *Fire Safety Journal*, 30(4), pp. 333–356. doi:10.1016/S0379-7112(97)00050-7.

Tsuda, A., Henry, F.S. and Butler, J.P. (2013) 'Particle transport and deposition: Basic physics of particle kinetics', *Comprehensive Physiology*, 3(4), pp. 1437–1471. doi:10.1002/cphy.c100085.

United Nations Environment Programme (2022) *Spreading like Wildfire – The Rising Threat of Extraordinary Landscape Fires*, *A UNEP Rapid Response Assessment*. Nairobi. doi:10.1038/news000413-8.

Urban, J.L., Song, J., Santamaria, S. and Fernandez-Pello, C. (2019) 'Ignition of a spot smolder in a moist fuel bed by a firebrand', *Fire Safety Journal*, 108(May), p. 102833. doi:10.1016/j.firesaf.2019.102833.

US Department of Housing and Urban Development (2021) *U.S. Census Bureau*, *Choice Reviews Online*. doi:10.5860/choice.49-3060.

Vacca, P., Caballero, D., Pastor, E. and Planas, E. (2020) 'WUI fire risk mitigation in Europe: A performance-based design approach at home-owner level', *Journal of Safety Science and Resilience*, 1, pp. 97–105. doi:10.1016/j.jnlssr.2020.08.001.

Vacca, P., Planas, E., Mata, C., Muñoz, J.A., Heymes, F. and Pastor, E. (2022) 'Experimental analysis of real-scale burning tests of artificial fuel packs at the Wildland-Urban Interface', *Safety Science*, 146(September 2021). doi:10.1016/j.ssci.2021.105568.

Verisk (2022) *Wildfire Risk Analysis*, *Verisk.com*. Available at: https://www.verisk.com/insurance/campaigns/location-fireline-state-risk-report/ (Accessed: 13 June 2022).

Viegas, D.X., Almeida, M., Raposo, J., Oliveira, R. and Viegas, C.X. (2014) 'Ignition of Mediterranean Fuel Beds by Several Types of Firebrands', *Fire Technology*, 50(1), pp. 61–77. doi:10.1007/s10694-012-0267-8.

Wadhwani, R. (2019) *Physics-based simulation of short-range spotting in wildfires*. Victoria University.

Wadhwani, R., Sutherland, D., Ooi, A. and Moinuddin, K. (2022) 'Firebrand transport from a novel firebrand generator: Numerical simulation of laboratory experiments', *International Journal of Wildland Fire*, 31(6), pp. 634–648. doi:10.1071/WF21088.

Wadhwani, Sullivan, Wickramasinghe, Kyng, Khan and Moinuddin (2022) 'A review of firebrand studies on generation and transport', *Fire Safety Journal*, 134(September), p. 103674. doi:10.1016/j.firesaf.2022.103674.

Wadhwani, Sutherland, D., Ooi, A., Moinuddin, K. and Thorpe, G. (2017) 'Verification of a Lagrangian particle model for short-range firebrand transport', *Fire Safety Journal*, 91(May), pp. 776–783. doi:10.1016/j.firesaf.2017.03.019.

Watts, J.M. (2008) 'Fire Risk Indexing', in *The SFPE Handbook of Fire Protection Engineering*, pp. 5168–5185.

Wessies, S.S., Chang, M.K., Marr, K.C. and Ezekoye, O.A. (2019) 'Experimental and Analytical Characterization of Firebrand Ignition of Home Insulation Materials', *Fire Technology*, 55(3), pp. 1027–1056. doi:10.1007/s10694-019-00818-8.

Wheeler, J. (2004) 'Testing for Deck Material Flammability', *Fire Management*, 64(4), pp. 13–15.

White, N., Delichatsios, M., Ahrens, M. and Kimball, A. (2013) *Fire hazards of exterior wall assemblies containing combustible components*, *MATEC Web of Conferences*. doi:10.1051/matecconf/20130902005.

Wickramasinghe, A., Khan, N. and Moinuddin, K. (2022) 'Determining

Firebrand Generation Rate Using Physics-Based Modelling from Experimental Studies through Inverse Analysis', *Fire*, 5(1). doi:10.3390/fire5010006.

Wilson, A.A.G. (1984) *Assessing the bushfire hazard of houses: A quantitative approach*. Melbourne.

Woycheese, J.P. and Pagni, P.J. (1999) 'Combustion models for wooden brands', *Proc. 3rd Int. Conf. on Fire Research and Engineering, Society of Fire Protection Engineers, Washington, USA*, p. 53.

Xiong, C., Liu, Y., Xu, C. and Huang, X. (2021) 'Acoustical Extinction of Flame on Moving Firebrand for the Fire Protection in Wildland–Urban Interface', *Fire Technology*, 57(3), pp. 1365–1380. doi:10.1007/s10694-020-01059-w.

Zhang, P., Sherman, D.J. and Li, B. (2021) 'Aeolian creep transport: A review', *Aeolian Research*, 51(April), p. 100711. doi:10.1016/j.aeolia.2021.100711.